2018

High Temperature Compression Creep Of U3Si2

Emil Angelo Cahanap Mercado
University of South Carolina

HIGH TEMPERATURE COMPRESSION CREEP OF U_3Si_2

by

Emil Angelo Cahanap Mercado

Bachelor of Science
University of South Carolina, 2015

Submitted in Partial Fulfillment of the Requirements

For the Degree of Master of Science in

Mechanical Engineering

College of Engineering and Computing

University of South Carolina

2018

Accepted by:

Xinyu Huang, Director of Thesis

Travis Knight, Reader

Cheryl L. Addy, Vice Provost and Dean of the Graduate School

Abstract

As a result of the Fukushima Daiichi Nuclear Disaster in 2011, a push for increasing the safety of nuclear power plants was made through research grants funded through the United States Department of Energy via the Accident Tolerant Fuels (ATF) campaign. One of the focuses of the campaign is improving the accident tolerance of nuclear fuel during a loss of coolant accident.

A promising set of being researched from the ATF is Silicon Carbide (SiC) composite cladding and Uranium Silicide (U_3Si_2) fuel pellets. Under high temperatures, stresses, and times the creep deformation can play an important factor in pellet to cladding contact behavior. The objective of this research was to quantify the creep behavior of U_3Si_2 as input data for a fuel deformation code, BISON.

A compression creep test plan was carried out. A creep test stand was designed and constructed at USC. To reduce oxidation effects, the experiments take place in a high vacuum environment (total pressures were monitored to ~1E-3mbar and oxygen partial pressures ~1E-7mbar) which is achieved by a turbomolecular and vane pump combination. A constant load is applied using a pneumatic actuator and is monitored via an inline load cell. U_3Si_2 is electrically conductive. Direct joule heating method was utilized to bring the sample to high temperature. A chain of step down AC transformers was implemented to obtain high amperage suitable to heat the U_3Si_2 sample for creep testing. A two-color

pyrometer was utilized to monitor the temperature of the sample pellet. To reduce temperature fluctuation, a PID temperature controller was used. The controller uses the -pyrometer as input signal and a silicon crystal rectifier module to modulate power input to achieve a desired temperature. To accurately measure strain at high temperature, a telecentric lens and illuminator are used which captures the outline of the creep test pellets as viewed through borosilicate viewing windows. The telecentric lens and illuminator combination produced images with very low optical distortion (max theoretical distortion of 0.69um) and can measure strains in the range from 1000 to 2500 microstrain. A digital camera was used to record images at a fixed time interval as the sample deforms under the compressive stress and high temperatures. The captured images are processed in imageJ via an automatic template matching program. Using notches on the test pellets as strain markers, axial and radial deformation is calculated.

Creep tests were conducted from 850 to 1000ºC and stress states ranged from 30 to 80 MPa. Multiple stress and temperature combinations were performed on each pellet with total axial strains up to 18%. With a total running time of 4000 combined hours, 4 TB of images, a combination of 13 testing conditions and 5 U_3Si_2 creep test pellets, a steady state strain equation was obtained as a function of stress and temperature. At 850°C and stress of 70MPa, strain rate was found to be 4.51E-5 hr^{-1}, at 950°C at 77MPa strain rate was found to be 2.52E-4 hr^{-1}, and at 1000°C at 48MPa, strain rate was found to be 1.64E04 hr^{-1}. When using the Arrhenius form of the steady state creep equation, in these temperatures and stresses, the activation energy, Q, is 168kJ/mol and the stress exponent, n, is 1.94. With a low activation energy and stress exponent it is believed that the creep regime is best described via diffusional processes. To the best of our knowledge, this is the first time that

the high temperature creep properties of U_3Si_2 was experimentally obtained. With the data obtained from this research, the updated BISON fuel simulation code modeled a significant difference (5 GWd/MTU longer) between a case where creep deformation is taken into account and a case where no creep deformation is taken into account.

Table of Contents

List of Tables

List of Figures

Chapter 1 Background

1.1 Accident Tolerant Fuels Campaign

As a response to the Fukushima disaster in March 2011, United States congress provided funding to start developing nuclear fuels and claddings to develop enhanced accident tolerant fuels to the Department of Energy (DOE).

Figure 1.1: Hydrogen explosion at the Fukushima Daiichi plant [1]

In collaboration with industry efforts and government funding, research towards a possible replacement of the conventional UO_2-Zircaloy system took place. Accident tolerant fuels are in direct comparison to currently used UO_2-Zircaloy system; they can tolerate the loss of active cooling for a longer time period and have reduced fuel cladding interactions, whether they be chemical or mechanical interactions. In addition, their fuel performance under normal operating conditions must match or exceed the currently used UO_2 system. [2],[3]

Uranium Silicide (U_3Si_2) has been identified as a nuclear fuel replacement candidate due to a high uranium density and high thermal conductivity (in regards to UO_2). It can play a key role in creating accident tolerant nuclear reactors as a replacement of current fuel claddings require that the claddings be made of a material that may be safer, but provides less than ideal performance. These effects can be offset by U_3Si_2's higher thermal conductivity and higher uranium density when compared to UO_2. [4]

In a Loss of Coolant accident (LOCA), high temperatures can develop in the reactor and fuel pellets within. These high temperatures are conducive to creep of these materials, resulting in excessive deformation or possible interactions with the fuel cladding surrounding them.

1.2 Research Objective

The goal of this research is to determine the mechanical creep properties of U_3Si_2 via direct experimentation. This data will be used to develop models for implementation into BISON, a code for fuel performance.

1.3 Properties of U_3Si_2 and Comparison with UO_2

U_3Si_2 has a higher thermal conductivity and uranium density UO_2 as seen in Table 1.1. Its higher thermal conductivity makes it more resistant to centerline melting during accident conditions, reduce thermal gradients across the radius of the pellet, and reduce negative effects due to high temperatures such as grain growth, cracking, and fission product transport. A higher thermally conductive fuel will have a lower operating temperature, storing less energy. In general, a lower operating temperature leads to higher safety margins in a LOCA situation. [5]. In addition, U_3Si_2 has a higher theoretical uranium density, allowing for greater fissile density and times between reactor refueling, leading to potentially greater economics for the power plant without the need to increase enrichment

levels. [5] Accident tolerant performing cladding materials that have a larger neutron absorption penalties can be considered due to this higher uranium density. [4]

Table 1.1: Property Comparisons Between U_3Si_2 and UO_2 [6]

Property	U_3Si_2	UO_2
Theoretical Density (g/cm^3)	12.20	10.96
Uranium Density (g/cm^3)	11.31	9.66
Melting Point (°C)	1665	2810
Thermal Conductivity at 600°C (cal/cm-sec°C) (cal/cm-sec°C)	0.03	0.010
Electrical Resistivity at room temp (ohm-cm)	~10^-4	NA

U_3Si_2 is fairly conductive with an electrical resistivity on the order of 10^{-4} Ohm-cm. [6] It has been reported to have a low reactivity with water with up to a 0.4% weight change when exposed to water. Crystal structure of U_3Si_2 has been reported as Tetragonal [7]

1.4 UO_2-Zirconium vs U_3Si_2-SiC Cladding System

Conventional Pressurized Water Reactor (PWR) fuel designs use UO_2 pellets and zirconium alloy based cladding that, under accident conditions, react exothermically with steam and causes a release of hydrogen. Silicon Carbide (SiC) cladding is much less

susceptible to this exothermic and when paired with U_3Si_2, can operate at lower temperatures, increasing the factor of safety in accident conditions. [8]

When compared to a reference UO_2-ZIRCALOY system of comparable cladding thickness, U_3Si_2 and SiC is preliminarily modeled to provide up to a 5.6% reduction in Fuel Cycle costs and up to a 10.3% reduction for the 24 month fuel cycle. [8]

1.5 Creep

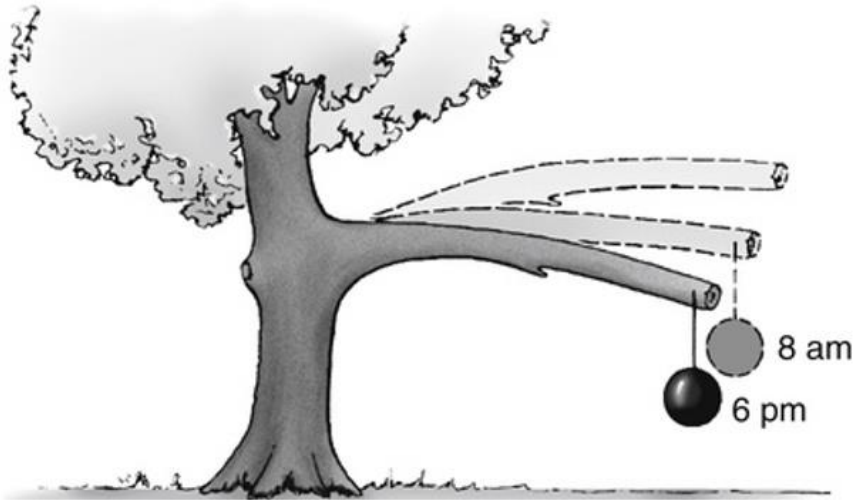

Figure 1.2: Illustration of a tree branch undergoing creep deformation. [9]

Thermal creep is a time dependent, plastic deformation that occurs below the yield strength of the material. Thermal creep is noticeable in materials given time and high temperatures. In addition, irradiation creep deformation occurs in materials that undergo fission (such as UO_2) and is caused by the agglomeration of fission-products in the fuel matrix; as these fission-products gather, they strain the structure and contribute to total deformation. [10] For the scope of this work however, only thermal type creep will be considered.

Multiple methods exist to collect creep data and include tensile creep testing, compressive creep testing, flexural (bend) testing, and indentation hardness creep testing.

Figure 1.3: Electromechanical driving Industry Tensile Creep stand ZwickUSA. [11]

The machines have different operating principles. Tensile testing machines apply a constant stress and temperature to a sample and a strain recorder measures the deformation as the test progresses. For certain materials, such as ceramics, the creep rate is extremely sensitive to the formed cavities when subjected to a tensile test. [12] Thus, compressive creep tests can be used to work around this sensitivity. The general testing procedure is generally the same as a tension creep test, but with a compressive load instead of a tensile load. Lastly, flexural bending tests apply a load to a flat, supported specimen to produce a bending moment in the material.

For flexural bending tests, just as in tensile and compressive tests, under high temperatures, a stress is developed in the material due to the applied force. Given enough time under temperature, a creep curve for the material can be made. Four point bend tests are ideal for brittle ceramics as it allows for simple shapes to be used.

Lastly, indentation hardness tests can be used to measure creep deformation. An indentation test (such as Brinell or Vickers) applies a penetrating indentation under a constant load for a specified time; this constant load applied over a period of time leads the material to deform and creep. [12]

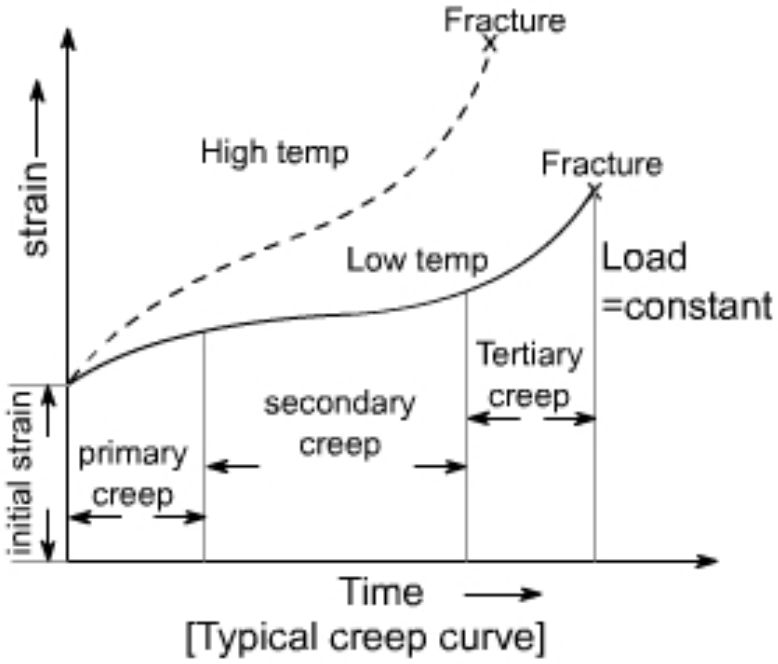

Figure 1.4: Typical creep curve displaying different regions of creep. [13]

For a typical creep strain vs time plot, there are three regions of creep: primary, secondary, and tertiary as seen in Figure 1.4. Primary creep has a nonuniform and transient strain rate, followed by a relatively stable creep rate. Secondary creep is generally the longest portion of a creep vs time curve and as such, most attention is given to this steady

state. Finally, tertiary creep occurs near failure and is associated with a transient strain rate that is higher than secondary creep rate and occurs until the material ruptures and fails [12].

As stated before, most engineering analysis is focused on the steady state, or secondary creep, behavior of a material. Steady state strain rate is modeled by an Arrhenius type equation [12] as

$$\frac{d\epsilon}{dt} = A\sigma^{n}\exp(-Q/RT) \qquad \text{Equation 1.1}$$

Where σ is the normal stress A is a pre exponential, n is the stress constant, Q activation energy, R is the universal gas constant, and T is absolute temperature. [12]

1.6 Mechanisms of Creep

Several mechanisms have been proposed that contribute to creep deformation in materials. They include: Dislocation slip, climb, grain-boundary sliding, and diffusional flow of vacancies [12].

In dislocation slip, deformation in the material is caused by the movement of dislocations throughout the atomic structure. Dislocations are disordered planes of atoms in an otherwise perfect structure and include edge dislocations (an extra plane of atoms "squeezed" in between the ordered structure) and screw dislocations (in which two touching faces of atoms are shifted relative to one another beginning at a point). Edge dislocations move in the same direction of the applied stress while screw dislocations move perpendicular to the stress and for both types, movement can only happen along the most densely packed planes of atoms [12].

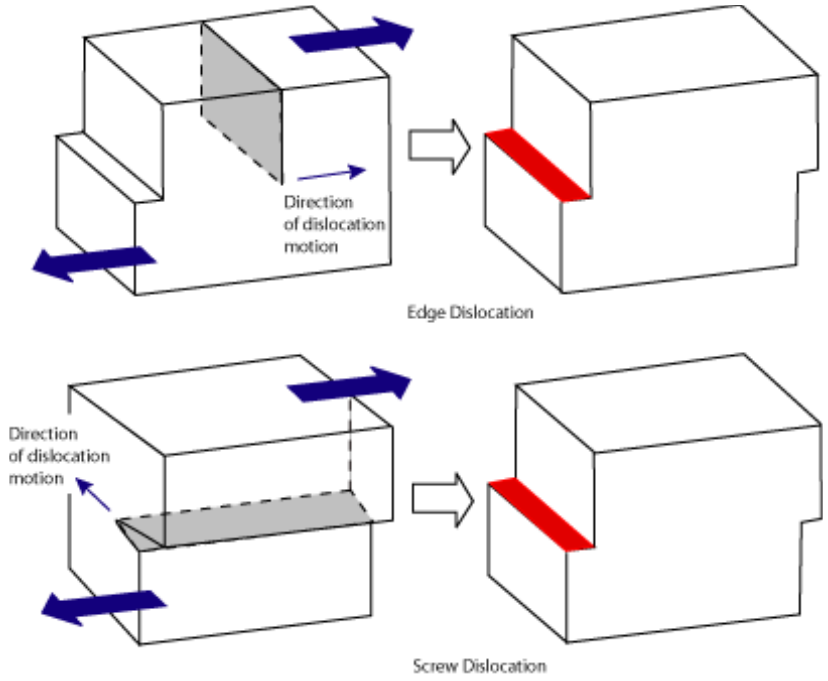

Figure 1.5: Edge dislocation vs screw dislocation in a crystal structure. Both dislocations deform the crystal structure and can occur during creep. [14]

In dislocation climb, dislocations maneuver around obstacles impeding their path via an exchange of atoms with vacancies surrounding these obstacles. [14] Types of obstacles dislocations can be hindered by include grain boundaries, impurities in the material, or other dislocations. When an atom is exchanged with a vacancy, the atom and the vacancy essentially switches places, leading to the net result of the dislocation maneuvering around the obstacle. The concentration of vacancies in a material increases exponentially as the temperature increases due to the atoms gaining more thermal energy. These atoms must move or self-diffuse throughout the lattice in order to climb and as such, the activation energies for self-diffusion and that for dislocation creep are often said to be the same. [12]

In slip (or glide) movement, dislocations move along planes of atoms called slip planes and move through the crystal by breaking and recreating atomic bonds. Creep

deformations due to dislocation slip are generally not significant at lower temperatures (but can still occur) but instead play a more important role as the material temperatures approach the melting temperature of the material. Stresses needed to drive dislocation slip are on the order of a tenth of the shear strength of the material. [12]

Grain boundary sliding (GBS) occurs when whole grains slide relative to one another along their shared boundary or in a zone close to the boundary. Grain size (and thus, the number of grain boundaries) in a material has a pronounced effect on the contribution of grain boundary sliding on the creep rate of a material, as decreasing the grain size will increase the number of grain boundaries thus leading to a reduced contribution from grain boundary sliding; this relationship can be seen with the Hall-Petch relationship [12] as seen below

$$\sigma_y = \sigma_0 + \frac{k_y}{\sqrt{d}} \qquad \text{Equation 1.2}$$

Where σ_y is the yield stress, σ_0 is the resistance to dislocation glide, k_y a measure of the dislocation pile-up behind an obstacle and d the size of the grain. Effects due to GBS can be reduced by employing a material with many precipitates, phases, or serrations at the grain boundaries as these additions serve to increase the friction and contact between boundaries. In general, no significant elongation of grains occurs under grain boundary sliding processes; this can be measured experimentally through grain size ratio analysis before and after creep. It plays a role in deformations when the temperature is at least half of the materials melting temperature and at low stresses. GBS contributes significantly to

polycrystalline ceramics at high temperatures by up to 60% of the total strain being caused by it. [12]

Diffusional creep (in regards to changing of a grain size) occurs when mass is transported through or around grains in an atomic structure with grain boundaries acting as sources and "sinks" of vacancies as seen in Figure 1.6. These vacancies in the atomic lattice of each grain switch places with atoms in the lattice leading to a change of grain shape in response to the applied stress [12]. Two major models exist: Nabarro-Herring Creep and Coble Creep. They differ in that Nabarro Herring creep, the atoms move through the atomic lattice and Coble flows along the grain boundaries.

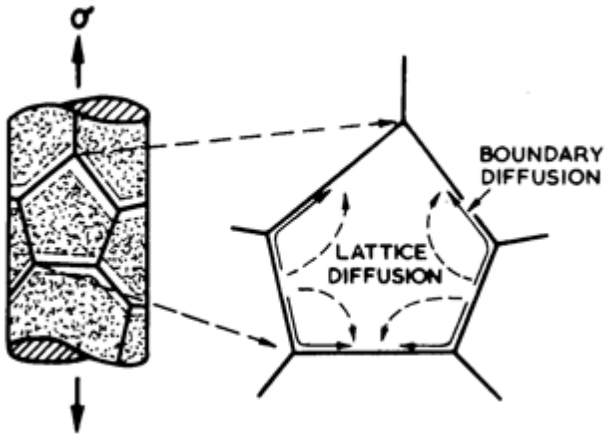

Figure 1.6: The movement of atoms as a response to the applied tensile stress through Lattice (Nabarro-Herring) and Boundary Diffusion (Coble Creep) [15]

In Nabarro-Herring creep (lattice diffusion), a flow of atoms move from the tensile to the compressed faces of a grain through the respective grain. The creep rate is proportional to the vacancy flux and is inversely proportional to the square of the grain size of the material. Nabarro-Herring creep generally occurs during low-stress and higher temperatures

For Nabarro-Herring diffusional creep, strain rate is described by the following equation [12]

$$\frac{d\epsilon}{dt} = \frac{16\alpha D_s}{\pi d^2}\frac{\sigma V}{kT} \qquad \text{Equation 1.3}$$

Where α is a geometrical factor, D_s is the self-diffusion coefficient, V is the atomic volume of a vacancy, d is the size of the grain with an (with an inverse squared dependence), T is temperature, σ is stress and k is Boltzmann's constant. [12].

Coble creep or boundary diffusion occurs when atoms move along grain boundaries to produce a change in grain shape and is thought to occur at lower temperatures than Nabarro-Herring. Coble creep rate is also dependent on grain size but has a strong, inverse cubic dependence on it. An equation to model creep rate [12] due to Coble creep is given as

$$\frac{d\epsilon}{dt} = \frac{150\ \Omega\ \delta D_{gb}\sigma}{\pi d^3 kT} \qquad \text{Equation 1.4}$$

Where δ is effective grain boundary width, D_{gb} is grain boundary diffusion coefficient, σ the applied stress, k is the Boltzmann's constant, T is temperature, d is the size of the average grain, and $\Omega = 0.7b^3$ where b is the burgers vector. Again, the strain rate is inversely dependent on the cube of the grain size, d.

For both types of creep, the stress exponent is theoretically one but can be range anywhere from one to two in practice. Activation energies of Coble creep are lower than that of Nabarro-Herring creep, leading to it being more preferable at lower temperatures. It is worth noting these different types of creep can occur at the same time complicating

efforts to establish what kinds are active at different temperature and stress conditions. [12], [16]

1.7 UO_2 Creep

A report by Armstrong et al [17] tested polycrystalline UO_2 samples with a density range from 93 to 98% with grain sizes from 6 to 40 microns using a bending beam creep test. Testing conditions in their atmosphere controlled creep rig ranged from 1250 to 1400°C and stress from 700 to 16000 psi. They found that below 10000 psi, creep rates of the higher density UO_2 could be modeled with the Ahhrenius equation with a stress exponent equal to about 1 and at higher stresses, the creep rate increased rapidly with increasing stress. They report that creep rate of UO_2 is dependent on density and believe that the pore structure (size, shape and location) may have an effect on the creep rate of the sintered pellets. They found that for pores located within the grains had little effect on the creep rate as opposed to the pores that were located near the grain boundaries, suggesting that grain boundary sliding contributed substantially to the creep rates of their testing. They observed an activation energy for plastic deformation of 91 +/- 9 kcal for stoichiometric UO_2 which compares closely for self-diffusion of the U4+ ion in UO_2. [17]

A report by Bobay et al [18] details their results of a set of compressive creep experiments of stoichiometric UO_2 as a function of temperature and stress as well as the results from other researchers. Wolfe and Kaufman [19] performed tests on samples with grain sizes from 18 to 55 microns, testing temperatures from 1600 to 2000°C, and initial stress values from 1000 to 7500 psi. In their report, they found that the transition stress (from where creep rate is linearly dependent on stress to one where creep rate is exponentially dependent on stress) is dependent on the grain size; the transition was 3000 psi for 18 micron material and 2000 for 55 micron materials. From the data of their own

compression creep experiments, Bobay et al found that the creep rate is highly dependent on grain size at low stresses. (under 3000 psi) Some scatter was observed in the UO_2 creep data. However, a general trend was observed: at relatively low stresses (from 1000 to 3000 psi), a change in activation energies from 90 to 132 kcal/mole which indicated a change in the controlling creep mechanism. Their data agrees well with the previous data found on the creep of UO_2. Their results indicated that the creep rate was inversely related to the grain sized squared for low stresses and that no relationship was found between grain size and creep rate for stresses higher than 10000 psi. The posit that diffusional processes control the creep rate at low stresses as the calculated activation energy at low stresses (found to be 90 kcal /mole) is close to the activation energies of self-diffusion for the uranium atom in UO_2 (70 to 109 kcal /mole). Calculated activation energies from the set of experiments listed in their report range from 71 to 118 kcal /mole and compare to the values of self-diffusion of uranium atom in UO_2 favorable (found to be anywhere from 70 to 108kcal /mole) [18].

In addition to the work done with stoichiometric UO_2, researchers have studied the effects of adding oxide dopants to UO_2 to increase the creep rate and relax the effects of Pellet Cladding Mechanical Interaction (PCMI). For UO_2, a relationship between creep rate and the oxygen chemical potential of the material has been noted. Self-diffusion in UO_2 is controlled by the concentration of point defects [20]. These point defects include the usual vacancies found in as fabricated stoichiometric, unirradiated UO_2 fuel as well as the defects formed with irradiated fuels, such as Frenkel pairs (made of a vacancy and an interstitial of the same atom) and Schottky defects (consisting of two oxygen vacancies and one uranium vacancy). The concentration of these defects control and regulate the diffusion

of the oxygen into the material. As such, by changing the oxygen to metal ratio in the material (such as with oxide dopants), one changes the concentrations of the point defects, thereby affecting the creep rate of the material. In their study, Massih and Jernkvist studied the effects of Nb_2O_5 and Cr_2O_3 on the creep rate of UO_2. Experimental creep rates for both dopants increased the creep rate compared to non-doped UO_2 by 2 orders of magnitudes for conditions tested and reported on. They reference a study by Sawbridge and coworkers who note that at higher stresses, strain rate of UO_2 doped with Nb_2O_5 due to creep has a stress exponent value of 3 to 4, typically corresponding to dislocation creep mechanism. [20] Duguay et al [21]evaluated the effects of Cr_2O_3 dopant vs stoichiometric UO_2 and found that for the testing conditions (at 1500°C, 20 to 70MPa) Cr_2O_3 doped samples had several orders of magnitude higher creep rates compared to reference UO_2.

1.8 Modeling of U_3Si_2 Creep - Previous Work

An analysis of U_3Si_2 material properties was completed at USC previously and includes a section on the creep properties of the fuel. [22] At low temperatures, irradiation induced creep is predicted to dominate and transitions to thermal creep at higher temperatures. Uranium Carbide data is used as a surrogate for U_3Si_2 data due to similar strong covalent bonding characteristics. As such, the average onset temperature for athermal to thermally induced creep used is 0.45Tmelt (the same as UC) in the U_3Si_2 model, corresponding to a value of 872°K. The Nabarro Herring creep rate equation is used as the predictor for the strain rate in this athermal regime. For the thermal creep regime, two types of creep are considered: Coble creep or dislocation climb and glide. For normalized stresses (stress divided by shear modulus) greater than 10^{-4}, the predicted thermal creep is described by dislocation climb and glide and when it is less than 10^{-4}, the predicted creep is described by Coble creep

Data from either sintering production of U_3Si_2 or DFT data is used in the model for the grain boundary and lattice activation energies and diffusion constants. A fixed stress of 5 MPa was used and the fuel pellet is assumed to be 100% dense with no porosity and thus, with no volume for the fuel deform into. The model takes into account the fuel swelling behavior of U_3Si_2 and is based off of the cumulative burnup. The creep model developed predicts extremely low creep rates that are insufficient to significantly relieve stresses when the fuel comes into contact with the cladding but predicts that the creep will extend the time until fuel to cladding contact [22]. The model is preliminary and is constantly being updated; the creep data provided with this research and more experiments to accurately determine the swelling characteristics of the fuel should improve the accuracy of the results.

U_3Si_2 has been reported to undergo oxidation and complete deterioration in air at temperatures as low as 315°C. [6] Furthermore, along with U_3Si_5, U_3Si_2 was noted to experience extreme exothermic oxidation reactions [4]. Thermogravimetric tests at LANL indicated that U_3Si_2 severely degraded at temperatures above ~800°K unless testing was done in ultra-high vacuum with ultra-high purity argon gas. [4] It was with these considerations that the decision to perform the creep test under a high vacuum environment was made.

Chapter 2 Experimental Setup

2.1 Telecentric Strain Measurement

A telecentric lens and illuminator setup is used due to the low distortion of the image as seen in Figure 2.1. Telecentric setups allow for an orthographic projection of the object in the field of view with little distortion. [23]

When used in combination with an illuminator, an object placed in between the camera and the illuminator will appear to the camera as a shadow of the objects outline. Due to the coliminated and parallel nature of the light rays coming from the illuminator and the properties of the telecentric lens, the shadow that is cast is a high contrast and highly accurate silhouette. Any changes in the objects shadow outline (such as shrinking in height or expansion in the width) will be captured via the changes in the shadow images. [23] As an example, the sphere in the center of Figure 2.1 would appear to the camera lens as a perfect circle.

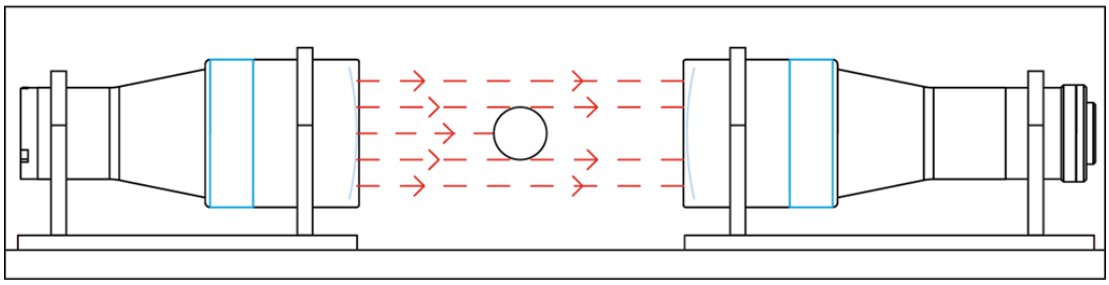

Figure 2.1: Parallel rays from the telecentric illuminator (left) project a shadow to the telecentric lens (right)

2.2 Image Processing and Strain Measurement

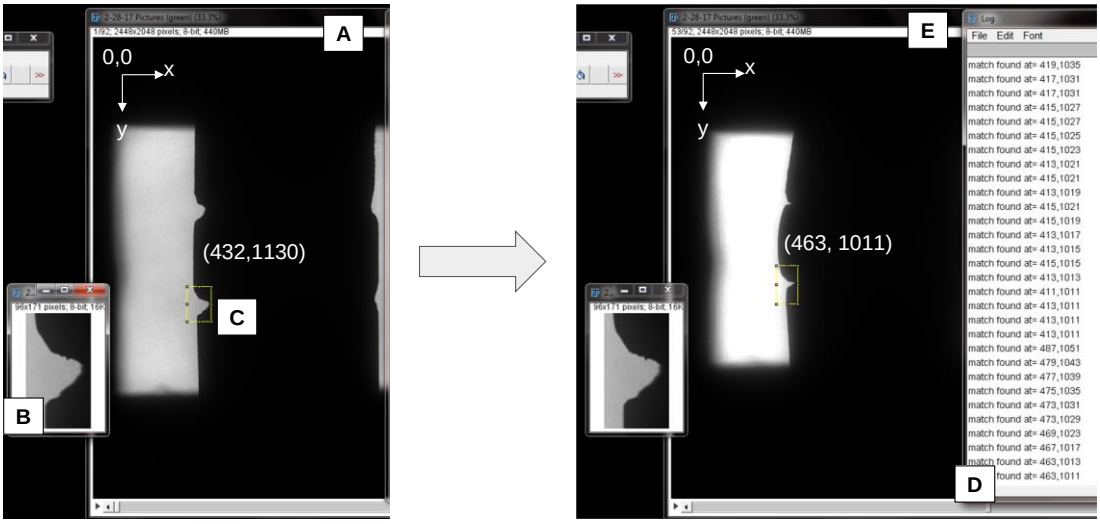

Figure 2.2: ImageJ notch Tracking. The initial image is on the left and deformed image is on the right (Sample 150813a)

The images are processed using ImageJ and the cvMatch template plugin. The cvMatch plugin takes two images: a template image to match [B] and an initial reference image to search [A].

The pellets are notched via electrical discharge machining (EDM) wire cutting. They are less than one millimeter deep and are located in the middle third of the pellets height as seen in Figure 2.3. In general, most pellets have four notches cut on opposite sides of one another. They appear to the camera system as a silhouette [A]

Figure 2.3: Sketch of a notched sample (left) with a typical creep sample (150813a) on the right

The image of a notch [C] is chosen as the template and the test images [A] are used as the reference images. As the pellet deforms, the notch moves and the cvMatch plugin will track the notch in the deformed image [E]. When a match is made, the x and y pixel coordinate positions of the notch are saved [D]. [24]

2.3 True Stress Calculation

To account for changes in sample diameter, instantaneous area is calculated from the shadow images assuming a perfectly round cylinder. The largest diameter (generally the middle of the pellet) is chosen for the true stress calculations.

The diameter is calculated from a smaller sample of shadow images. For example, for sample 150813a, there were 93 total shadow images used to calculate strain values with 12 images chosen to be measured diameterally. This was done because the widest part of the pellet has no notches (which the cvMatch template plugin uses as templates) and must be tracked manually. To measure this area, the manual tracking plugin of imageJ was used.

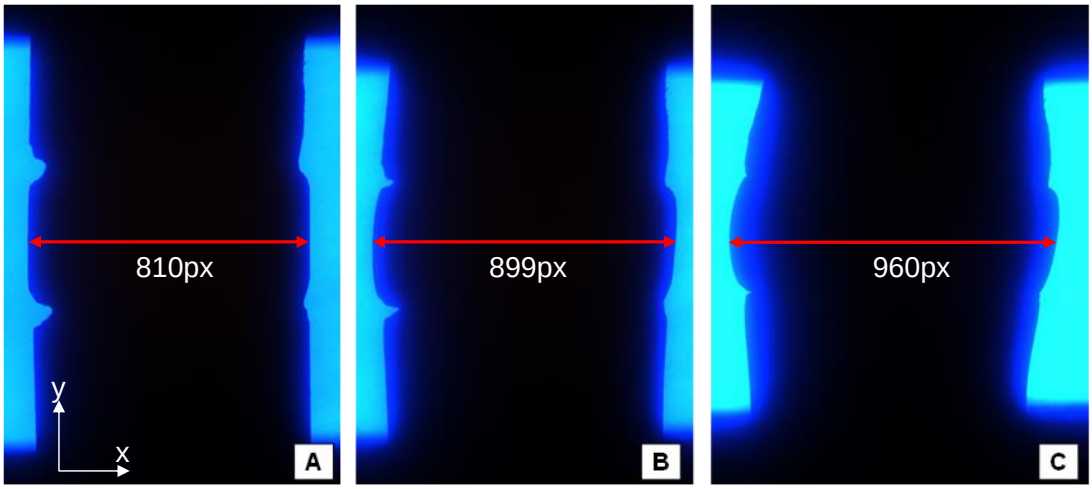

Figure 2.4: 150813a diameter measure

The diameter of the sample obtained is in terms of pixels as seen in Figure 2.4. Using the same camera setup, a picture of a precision tooling ball [25] was used to correlate the pixel value with a known size.

Figure 2.5: Tooling ball [25] used to correlate pixel and length

The tooling ball has a ball diameter of 0.5 inches +/- 0.0002 inches and a shank diameter of .25 inches +/- 0.00015 inches. Using these relations, a relation was found to be 2.73E-4 inches/pixel.

Using this relationship, the pixel values from Figure 2.4 was converted to a useable length for calculations and assuming a perfectly round cylinder, the area was calculated.

2.4 True Strain Calculation

After processing the images in ImageJ, the x and y pixel coordinates of all four notches are mapped throughout the stack of test images. Axial length (along the height of the pellet) is calculated as the average of the distance between the notches on the left and the right side as seen in Figure 2.6.

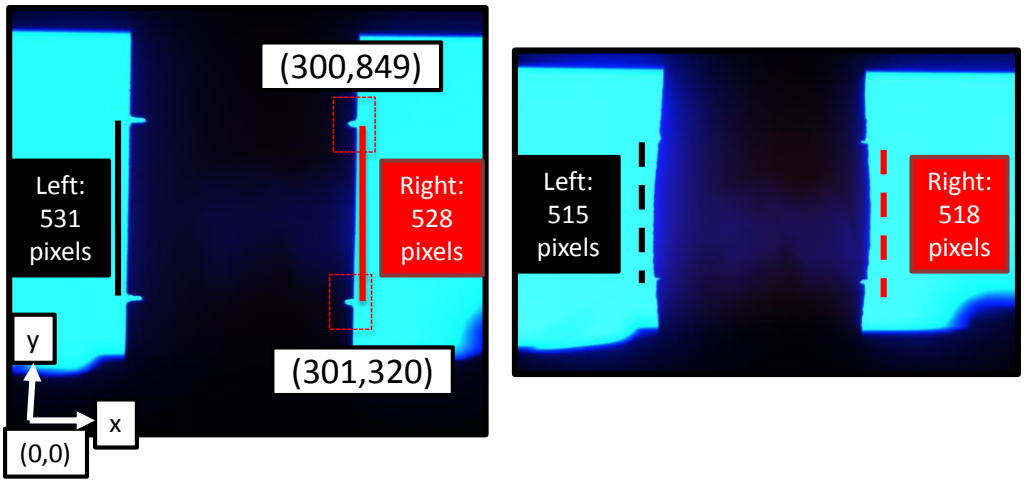

Figure 2.6: 161214c Vertical line length

In a similar manner, the diametral length is calculated from the manually picked diameter as shown in Figure 2.4. In addition, diametral strains are across the widest part of the pellet and the data are coarser than vertical strains reported.

True strain for both vertical and diametral cases [26] is taken as below

$$\epsilon = \ln(\frac{l_f}{l_0}) \qquad \text{Equation 2.1}$$

where l_f and l_0 are the final and initial axial lengths between the notches, respectivley.

2.5 Strain Smoothing and Data Representation

The strain data has been smoothed for better representation with the assumption that the strain is continuous and does not jump back and forth. Both vertical and diametral strains have been smoothed in this manner. The jumps in the original data are likely due to the automated template matching algorithm having problems with the camera and lighting noise in the images. However, general trends can still be gleaned from the data.

In addition, for all tests reported, the strain history plots start after the sample has been loaded and heated to the first testing condition and not the original height and dimensions.

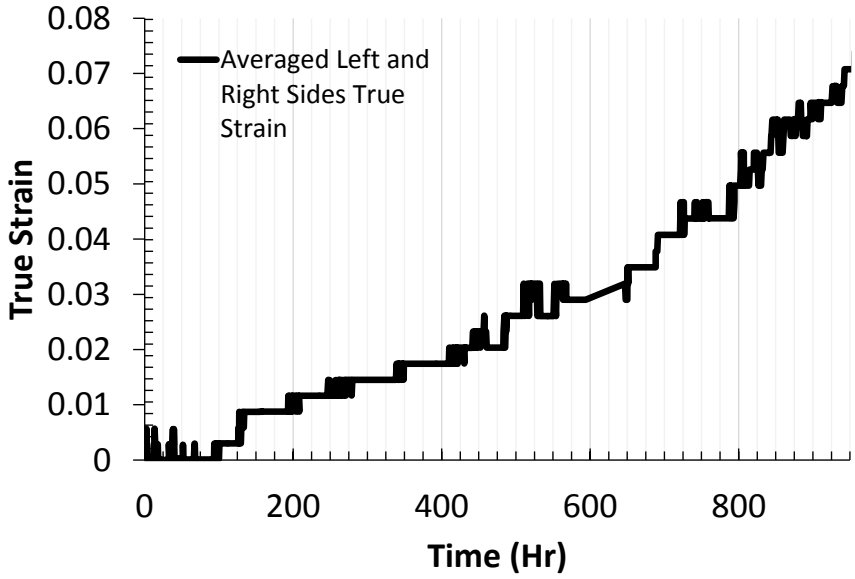

Figure 2.7: Vertical strain time history 161214a – unsmoothed

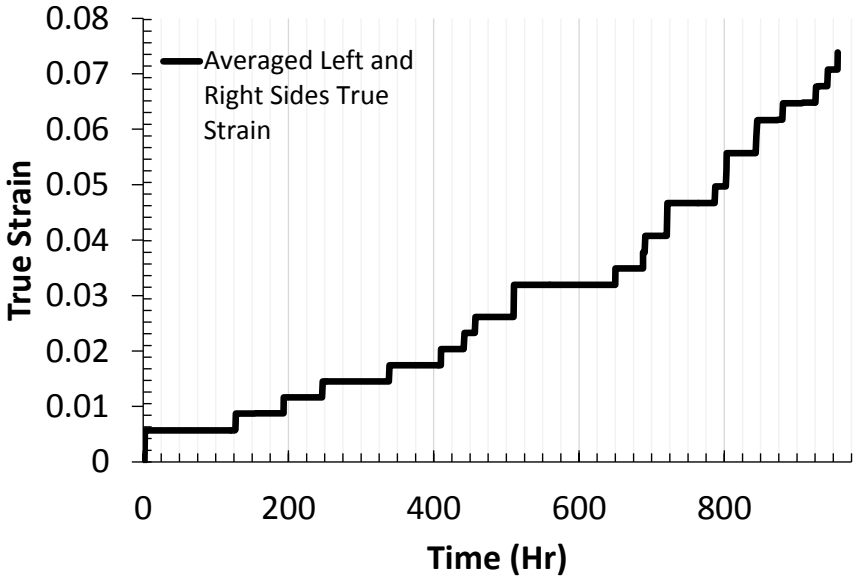

Figure 2.8: Vertical strain time history 161214a - smoothed

Each image's time stamp is correlated with the DAQ data time stamp to match the testing conditions with the image time.

2.6 Steady State Strain Rate

To report the steady state strain rate, each testing condition was first separated by temperature and stress. The strain vs time history for a single testing condition was then analyzed as shown in the figure below. The slope of the line (true strain divided by time) represents the strain rate.

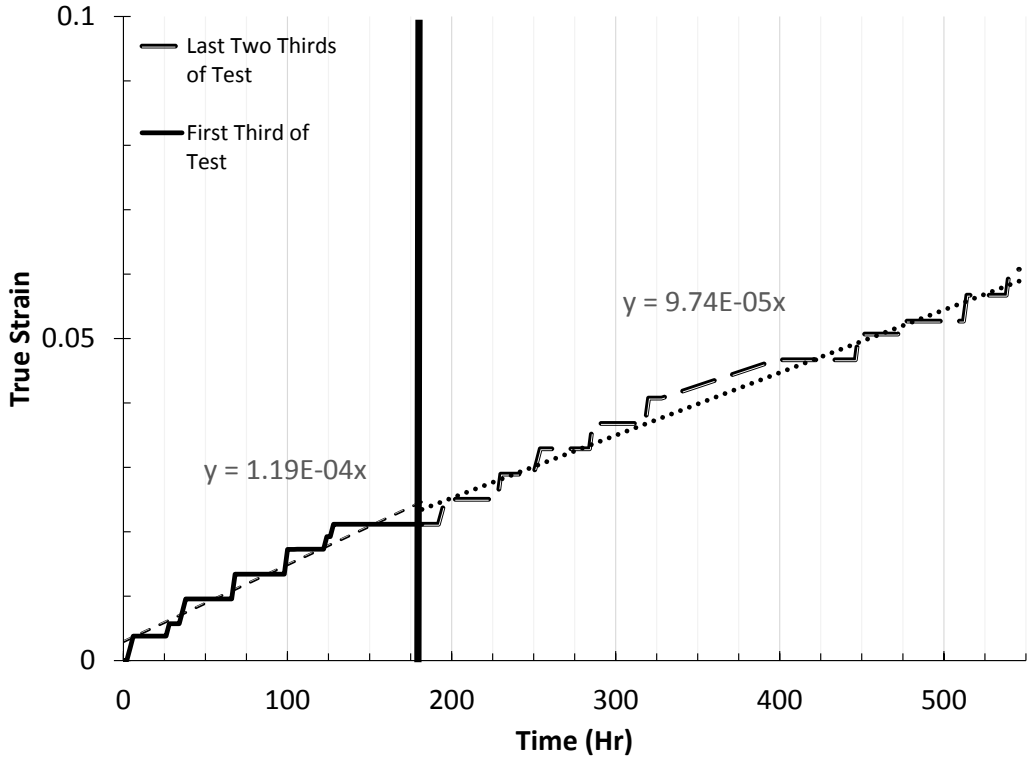

Figure 2.9:161214b steady state strain rate analysis for 950°C and 50MPa condition

To separate any effects of primary creep strain, the test time was split into two areas: the first third of the test and the last two thirds of the test. It is assumed that any effects due to primary or transient strains would have the greatest effect during the first part of the test. As a further check, the two strain rates were then compared with the percent difference

formula. If it was found that the strain rates were different by more than 15%, the test would not be considered steady state (secondary creep) and not be included in the analysis.

2.7 Heating Scheme

Direct joule heating is used to raise the temperature of the pellet. High amperage, low voltage, alternating current is chosen due to the ease of transforming current and voltage. [27]

$$P = I^2R \qquad \text{Equation 2.2}$$

As seen in the relation above, low pellet resistance (10-4 ohm-cm) necessitates the use of high amperage to reach heating power.[6]

2.8 System Overview

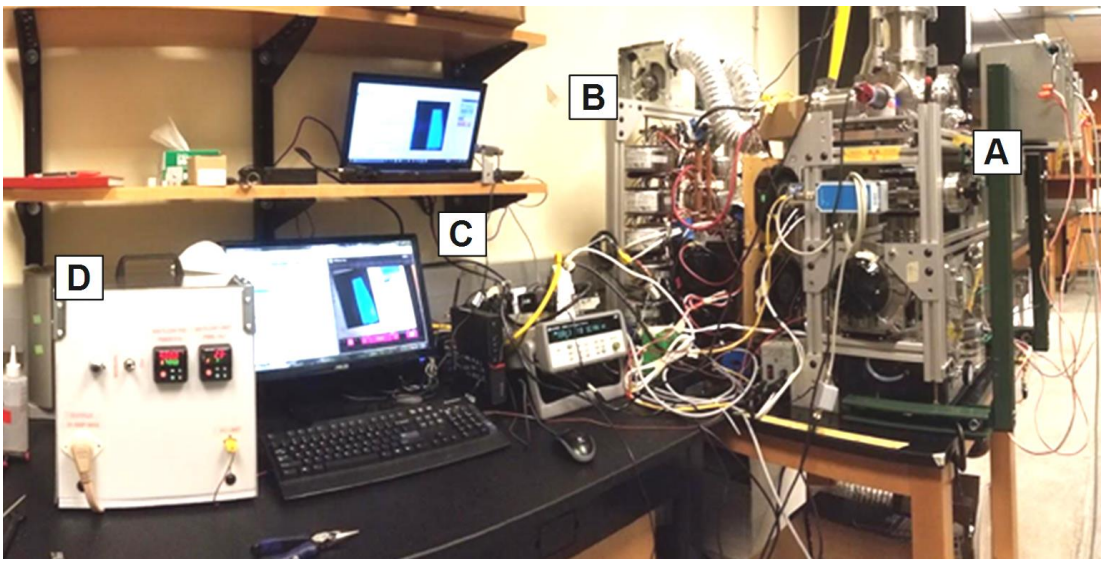

Figure 2.10: System overview of experimental setup

To measure the creep response of U_3Si_2, a test rig was designed and created. It uses a combination of pre-made parts as well as a mixture of fabricated pieces. It is split into multiple systems

A. Main test chamber and frame

B. Electrical power bank

C. Data acquisition

D. Temperature controller box

2.9 Frame

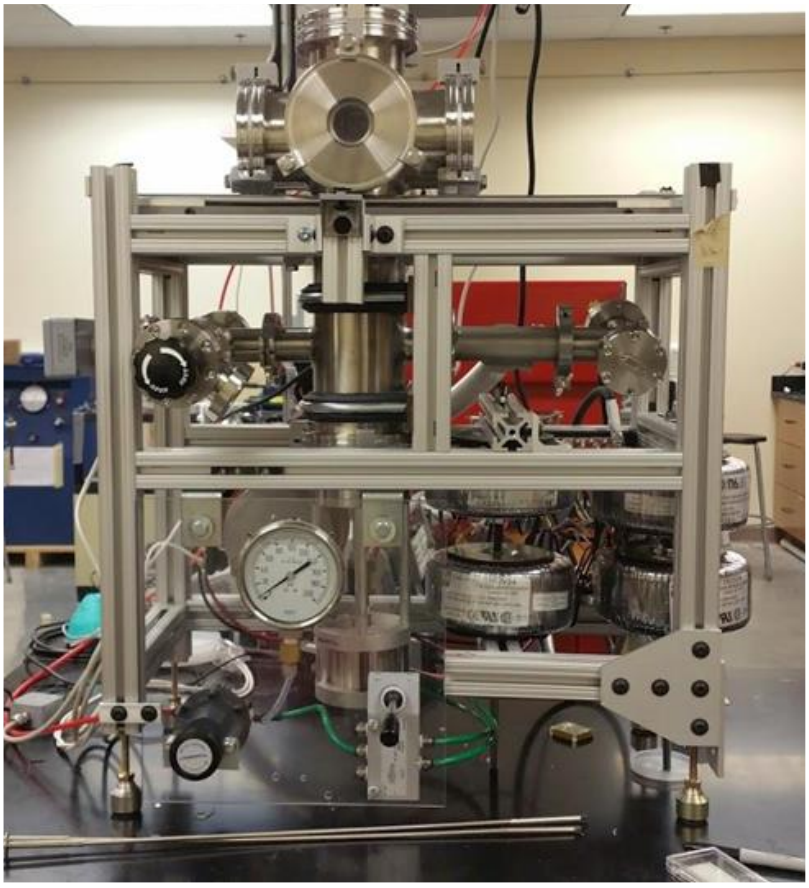

Figure 2.11: Test chamber and frame side view

An 80/20 extruded aluminum frame was designed and assembled to hold the vacuum chamber and testing equipment. The frame height and level is adjustable via adjustable feet on each of the four legs.

2.10 Vacuum Enclosures

304L Stainless steel vacuum enclosures from various manufactures make up the outer casing of the rig [28]. Industry standard vacuum flanges, including ISO100, ISO 45, and ISO 25 flanges are used. Viton O rings and gaskets are used to seal the sealing faces.

2.11 Cooling Fans

Cooling fans actively blow air over the test rig. This is to keep the rubber gaskets from becoming too hot and losing sealing effectiveness. In addition, special care is brought to the high current wires, transformer bank, and electrical feedthrough as considerable heat builds up along these high current devices if left uncooled.

2.12 Electrical Passthrough

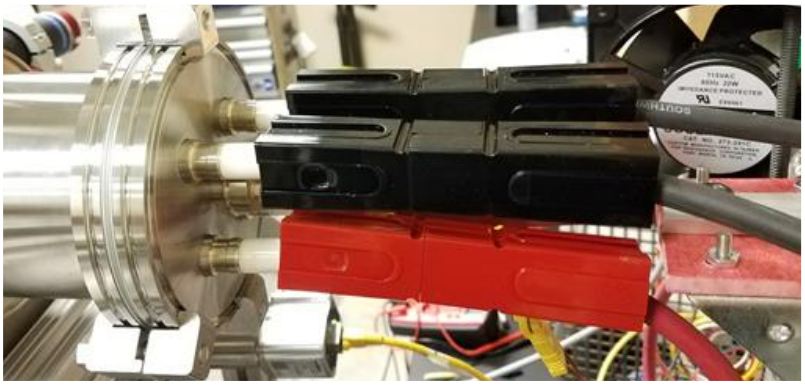

Figure 2.12: Passthrough as installed on the testing chamber

To allow current to enter the vacuum environment of the test rig, an electrical pass-through was installed. It is comprised of four, quarter inch copper terminals (two for input current and two for output current) and two K type thermocouple slots which allow for temperature measurement inside the testing stand. The maximum amperage of each copper terminal is 180 Amps for a combined maximum heating current of 360 Amps when used in pairs. Special attention is paid to cool these terminal connectors – high temperature (~130°F) were noted without forced cooling which presents a danger during long term testing.

2.13 Loading Frame

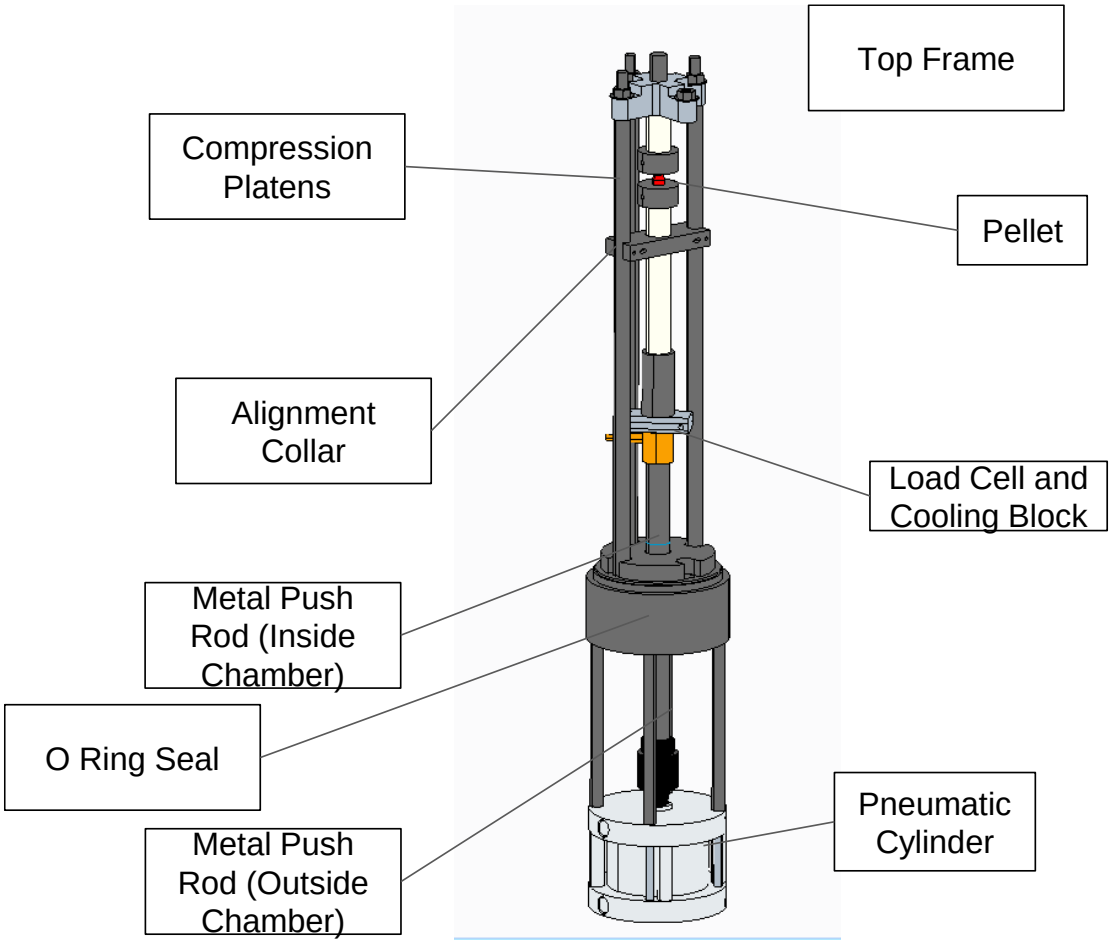

Figure 2.13: CAD design of internal loading frame

The test pellets are compressed via a loading frame. It is comprised of multiple pieces that work together to apply force to the pellet. A pair of O Ring seals maintain the environment inside the chamber and are effective to 10E-4 mbar total vacuum pressure. The internal load frame is partially assembled before insertion into the vacuum chamber and a specific installation order is necessary to correctly assemble the pieces. The fully constructed view is shown in Figure 2.14.

Figure 2.14: As constructed internal loading frame

2.14 Pneumatic Cylinder and Regulator

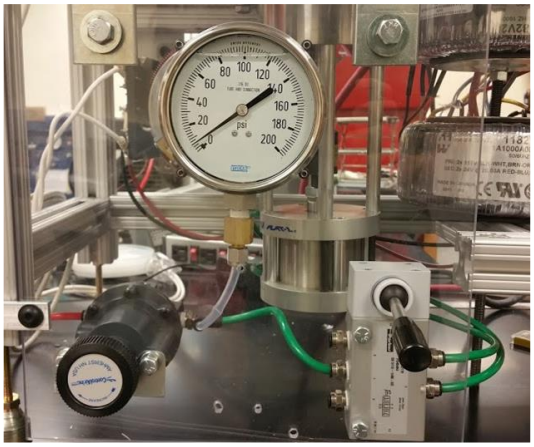

Figure 2.15: Operator panel for the pneumatic cylinder

From the bottom up, the loading frame starts at the pneumatic pancake cylinder as seen in Figure 2.15. The cylinder accepts air pressure from a precision air regulator which is pressurized by 100 psi shop air. The cylinder is attached to a metal push rod which then enters the vacuum chamber to apply load to the sample. A set of O-rings seals the vacuum chamber and the metal push rod to maintain the vacuum environment.

2.15 Load Cell, Water Cooling Block and Ceramic Collar

Figure 2.16: Load cell assembly with water pass through leading to the right

Attached to the push rods is a Futek load cell rated for 2000 lbf to measure the load applied to the sample. It is placed inside the testing chamber to reduce the frictional effects between the test chamber and the metal push rod. The load cell is capable of tension or compression load monitoring. In the test rig, it is threaded in line as a compression monitoring load cell with a stainless steel collar that keeps the ceramic rods in place.

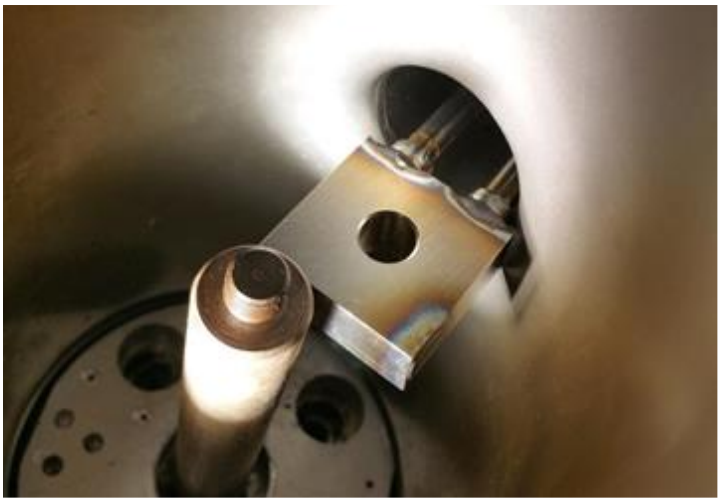

Figure 2.17: Water cooling block in test environment

A water cooling block transfers heat from the ceramic rods (which are hot due to the high temperature pellet) away from the load cell. Cool water is brought into the system via a water feedthrough and comes from the buildings chilled water supply. A thermocouple that is attached to the load cell then monitors the temperature and effectiveness of the cooling block during the tests. It is attached to the temperature controller box, where a limit controller cuts off system power if the load cell reaches a specified temperature limit.

Figure 2.18: Assembled load frame in testing chamber

Figure 2.19: External water supply feedthrough

2.16 Adjustable Alignment Collar

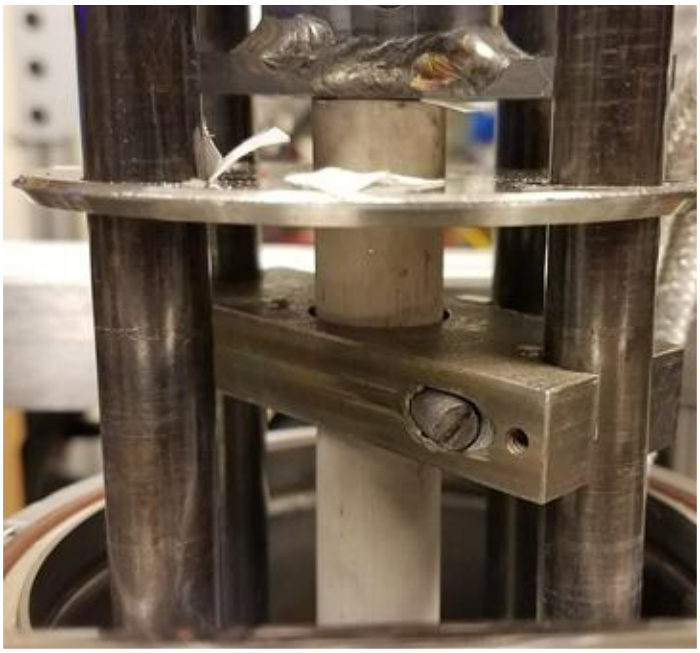

Figure 2.20: Alignment collar underneath bottom platen

To keep vertical compression rod alignment, a three way adjustable collar holds the ceramic compression tube in line. Internal ball bearings keep the rod aligned and are adjustable via a set of three set screws.

2.17 Compression Platens

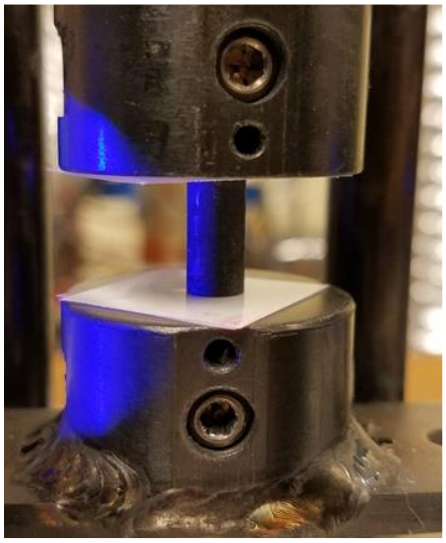

Figure 2.21: Top and bottom compression platens with a dummy graphite sample

Two Inconel platens were fabricated that are attached to the ceramic tubes. [29] This bottom platen serves as the bottom platform on which the U_3Si_2 pellet sits on. Current flows through this bottom platen, through the U_3Si_2 Pellet, then leaves through the top platen for the joule heating setup. Copper Bus bars connect these platens to the power feedthrough which then connects to the electrical system.

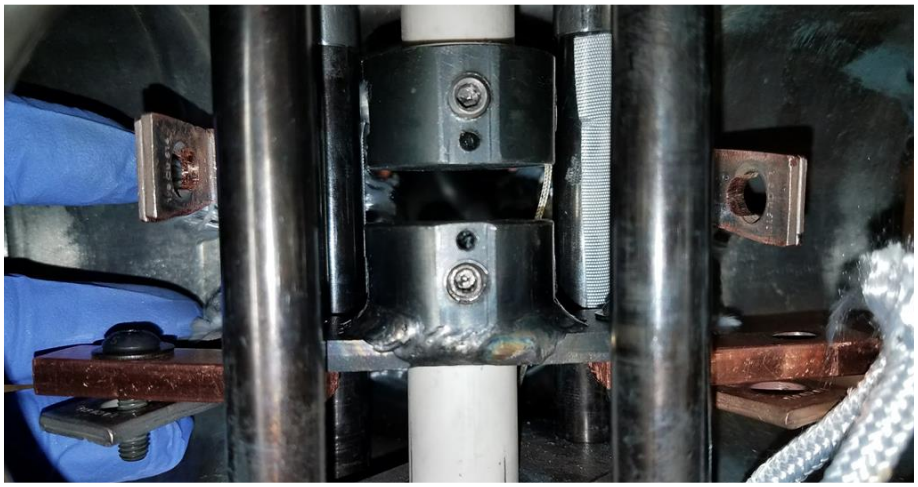

Figure 2.22: Inconel platens as installed in testing chamber

2.18 Top Cross

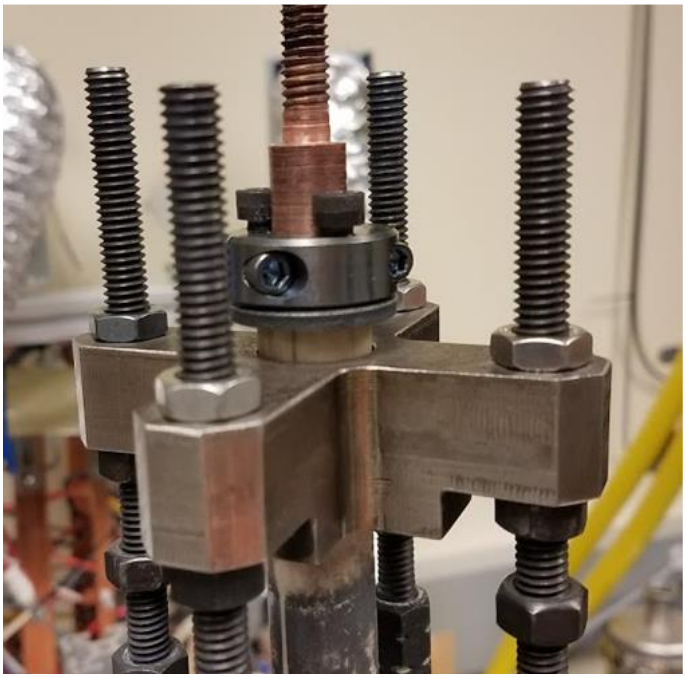

Figure 2.23: Top holding cross

The top holding frame is fixed to four posts and holds in the top loading frame ceramic tube. Using the four adjustment nuts, it is adjusted to ensure that the two platen faces are parallel with each other.

2.19 Radiation Heat Shield

Figure 2.24: Stainless steel heat shield with viewing holes

It was observed that at approximately 700°C, the pellet begins to emit a dull orange glow. As the pellet increases temperature, the glow becomes brighter and loses heat to the surrounding vacuum walls and system pieces via radiation. To reduce this radiative heat loss, a multi layered shield was designed and constructed via multiple stainless steel sheets cut by a water jet.

The shield is comprised of multiple layers of stainless steel foil that are concentrically arranged around the pellet. To reduce conductive heat transfer between the foil layers, ceramic screws separate each layer. The shield is slid around the pellet before the test is conducted and slides upwards when the pellet is to be removed.

Figure 2.25: Radiation shield as installed in testing chamber

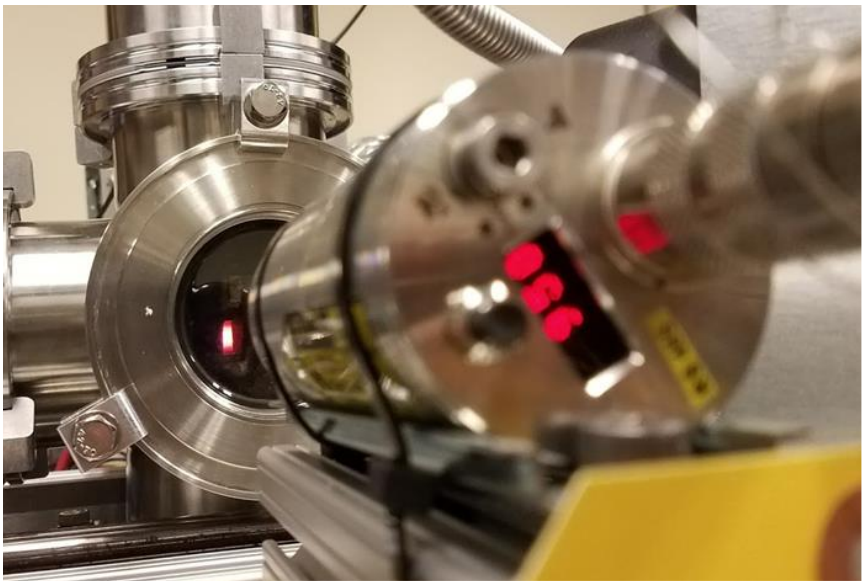

Figure 2.26: Glowing sample with pyrometer sighted on it

In the radiation shield, there are holes that allow for the telecentric optical setup to see the pellet as well as the pyrometer to sight the sample as seen in Figure 2.26.

2.20 Ceramic Tubes

Figure 2.27: Top and bottom mullite tubes

Mullite ceramic tubes are used to curtail the heat loss from the pellet. Compared to steel, Mullite ceramics have a much lower thermal conductivity [30] but are still suitable for the applied loads of the test. In addition, ceramic felt washers were cut via laser cutter

and inserted in between the inconel platens and the ceramic rods to further increase thermal resistivity.

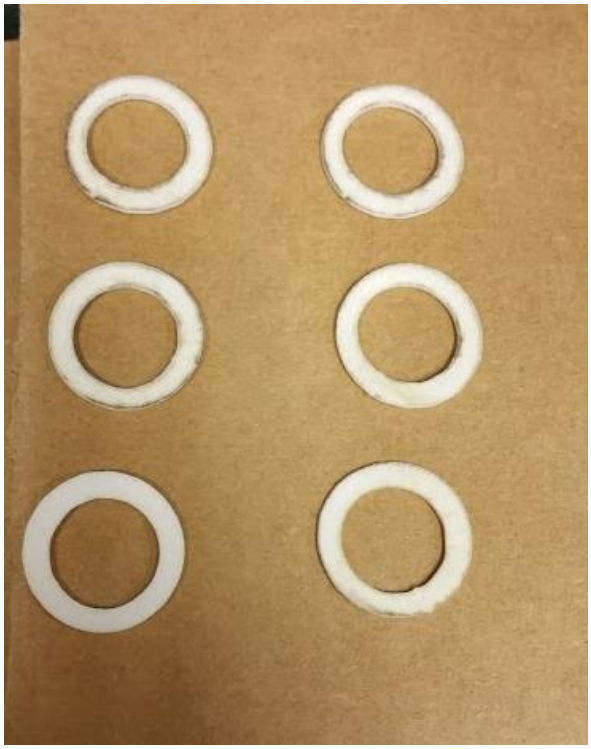

Figure 2.28: Ceramic felt washers

2.21 Active Guard Heater Cartridges

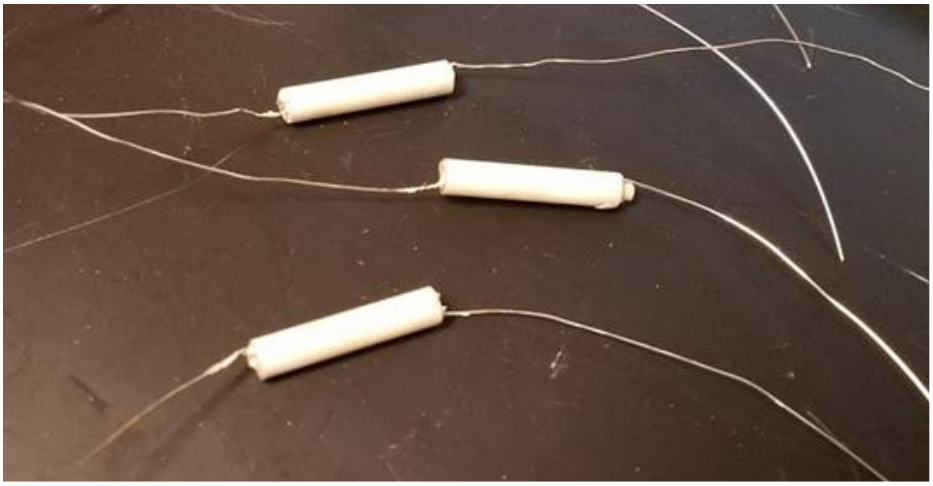

Figure 2.29: NiCr wound cartridge heaters

Figure 2.30: Cartridge heaters inserted into top platen

Cartridge heaters were sized to be inserted into holes found in the top and bottom platens. Ceramic tubes electrically isolate the guard heater circuit from interfering with the main heater power supply circuit. When a voltage is applied to these cartridge heaters, the high internal resistance of the NiCr wires causes the cartridge to heat up to temperatures up to 900°C. This creates a hot zone above and below the sample which helps to reduce the conductive heat loss from the sample.

Figure 2.31: Active guard heaters in test

2.22 Vacuum Pumps

Figure 2.32: Roughing vane pump for low vacuum

To reduce oxidation effects during high temperature testing, the creep tests take place in a high vacuumed environment. Two vacuum pumps work in tandem to bring the system down to high vacuum levels. The first stage roughing pump brings the vacuum environment to a low vacuum (approximately 10^{-1} mBar) at which point it reaches a steady state. The second stage turbomolecular pump then takes the system to 10^{-3} mBar.

Figure 2.33: Turbomolecular pump to bring system to high vacuum

In the event of a power loss or a vacuum interruption, an automatic shutoff valve has been installed to maintain the vacuum levels and environment inside the test rig that will seal the testing environment if it detects a power loss. Uninterruptable power supplies provide bridging power for all systems and allow the system to run fully for approximately 30 minutes

2.23 Zirox Oxygen Partial Pressure Probe

Figure 2.34: Partial pressure probe in operation

To monitor the oxygen partial pressure, a Zirox SS-28H vacuum probe is used. The sensing electrode heats up to 700°C and measures oxygen concentration inside the testing chamber versus the oxygen environment outside the testing chamber (considering the outside environment as the baseline). Effective range is from 1E5 Pa to 1E-21 Pa with less than a 5% relative error. [31] As stated before, the oxygen partial pressure was an important value to monitor due to the exothermic oxidation effect reported when the U_3Si_2 samples were heated in air.

2.24 Oerlikon Total Vacuum Gage

Figure 2.35: Total vacuum gage with display

An Oerlikon PTR 90 vacuum gage measures total vacuum pressure. The measurement range for the total vacuum pressure is 5E-9 to 1E3 mbar with an accuracy of +/- 30%. [32]

2.25 Load Cell

Figure 2.36: In-line compression load cell [33]

The Futek LCB200 tension and compression load cell measures the force the sample is receiving. The load cell has a 2000 lbf maximum load rating and nonlinearity and hysteresis values of 0.5% of the output; the non-repeatability is 0.1% of the output. [33]

A total of four thermocouple passthroughs allow for temperature sensing inside the test rig; each allows for a K type thermocouple to be attached. Thermocouples are installed onto the load cell as a check to ensure that it does not overheat due to the high temperature test. In addition, a thermocouple is attached inside the bottom Inconel platen to get a better sense of the temperature distribution inside the testing chamber directly underneath the sample.

2.26 Lumasense Noncontact Pyrometer

Figure 2.37: Lumasense ISR6 noncontact pyrometer [34]

A Lumasense ISR6 MB 18 Advanced Pyrometer is used to measure the sample temperature and is run in two color mode without having to touch the sample. Emissivity ratio is adjustable via the software. Previous efforts have been made to calibrate the emissivity ratio of U_3Si_2 to match the pyrometer temperature output to that of a thermocouple. The pyrometer is capable of measuring between 700°C to 1800°C with a measurement uncertainty of up to 0.6% of the reading. In the sighting range used, the spot size was approximately 1mm. [34]

2.27 Pyrometer Calibration

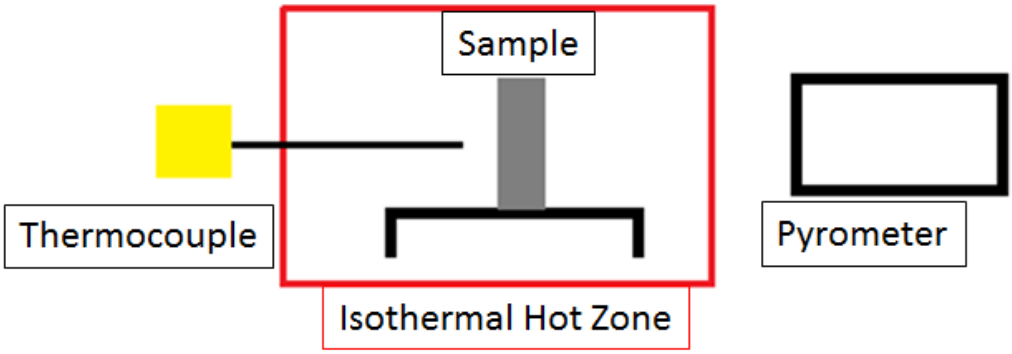

Figure 2.38: General setup of pyrometer calibration

To calibrate the pyrometer to read accurate test values, a test was conducted to match the pyrometer readings with that of a thermocouple. A U_3Si_2 tile was placed into a furnace with an argon gas input as seen in Figure 2.38. The tile is from the same batch as the 150813a and 150813b pellets.

The furnace hot zone was assumed to be isothermal and ceramic insulations blocked off the heating area. The thermocouple was placed within a centimeter of the U_3Si_2 tile, inside the hot zone, and the pyrometer was sighted onto the sample. It was assumed that the thermocouple was reading the correct temperature value of the furnace zone and that the tile was the same temperature as the furnace zone. The furnace began a heating cycle to 1300°C. At every 25°C, the pyrometer emissivity value was changed so that the pyrometer reading would match the thermocouple. This correlation then gave a calibrated emissivity ratio value which could be used for a corresponding value of U_3Si_2 temperature.

Figure 2.39: View from pyrometer port of the U_3Si_2 tile for calibration testing

2.28 Optical Equipment and Frame

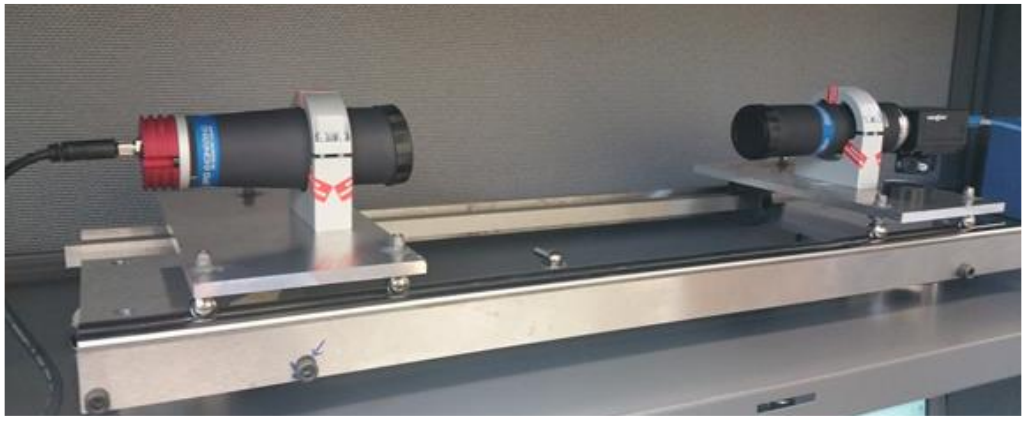

Figure 2.40: Telecentric camera and illuminator on frame

To measure visual changes in the sample, a telecentric camera lens and light source were employed. The camera used is a Grasshopper 5.0 MP Firewire Camera with a resolution of 2448x2048, a pixel size of 3.45 um. [35]

The camera is mounted to a long distance telecentric lens with a working distance of 132.3mm, a maximum distortion of 0.2% and an object field of view of 16.9 x 14.1 mm x mm. The illuminator light source has a blue color corresponding to a 460 nm wavelength and a working distance range of 45-90 mm and is mounted directly opposite to the camera

system [36]. All optical components are mounted on movable carts which are kept aligned through a system of precision ground rods and surfaces.

The optical frame has been assembled on a stone table to ensure a flat plane of conformity. In addition, either end of the frame has been milled from the same block of aluminum to better aid in alignment. Two ground rods and a bar stock are then slid into these block of aluminum and provide the surface on which the optical carts move along.

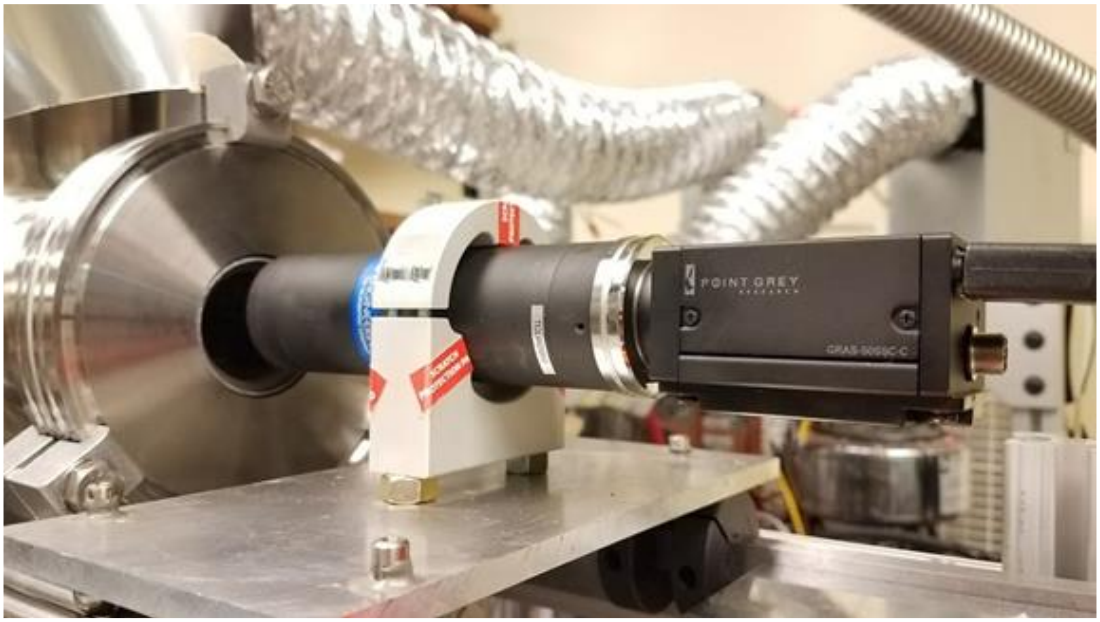

Figure 2.41: Camera as focused on the sample outside of the test rig

Quartz glass windows allow for viewing into the test rig. Installed on the six way vacuum chamber are three glass windows: two allow for the telecentric camera and illuminator to view the sample and one allows for the pyrometer to measure sample temperature.

2.29 Electrical Power Bank [B]

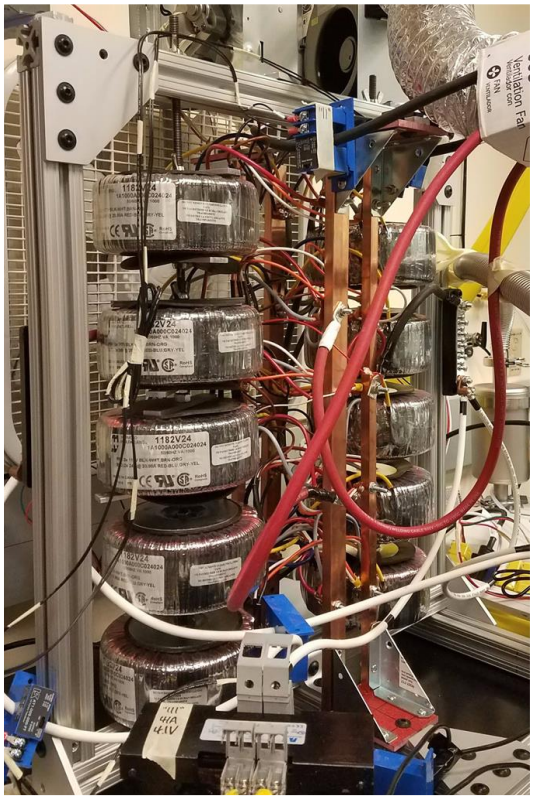

Figure 2.42: Final stage of power bank chain

A multi stage step down, AC power bank chain is used to drive the joule heating circuit. The power chain begins with an initial stage VARIAC which allows for a coarse adjustment of power input. After the first stage VARIAC, the load is then fed to an intermediate transformer bank. The intermediate transformers are a bank of four ACME FS11000 transformers [37] wired in parallel. Voltage is stepped down in this intermediate step and amperage is stepped up until it is fed to the final stage power bank. The final transformer bank is made of 10 Hammond Manufacturing 1182v24 colloidal transformers which is the last step down stage before the current enters the sample [38].

2.30 Temperature Controller Box [D]

Figure 2.43: Front panel of temperature controller box

To regulate temperature fluctuations a temperature controller box is implemented using an internal solid crystal rectifier to modulate the input power to the power bank.

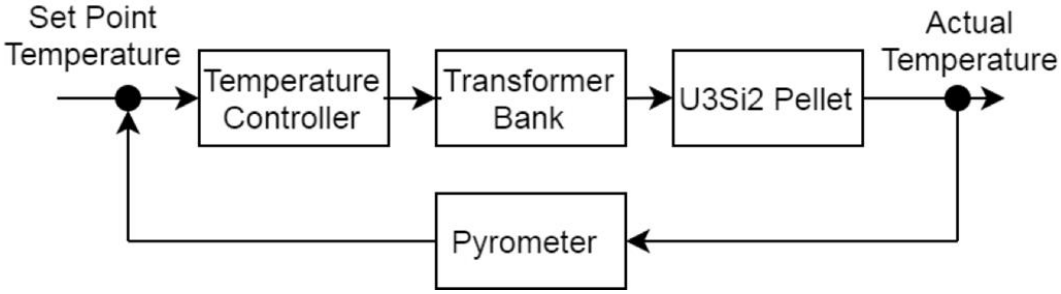

Figure 2.44: Closed loop control diagram

The temperature controller box allows for closed loop feedback control. The input temperature from the pyrometer is compared with the set temperature. A PID controller (Watlow pm6rf1a) [39] adjusts the input power via the SCR unit to automatically match the two values. The main power bank is connected directly to the SCR unit.

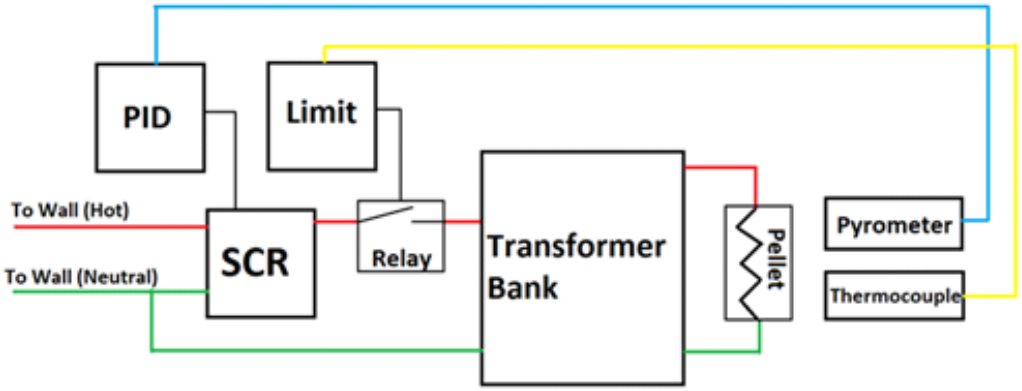

Figure 2.45: Functional diagram overview of electrical system

2.31 Data Acquisition and Computers [C]

All sensors are connected to the Agilent 34972A Data Acquisition Switch Unit (DAQ). The DAQ is periodically stopped to save the data but in general, runs continuously with the camera system throughout the creep tests. The measurement accuracy of the DC voltage of the DAQ is between 0.0006 and 0.0035V. [40]

Remote monitoring is done through an automatic screen capture software to periodically check in on the status of the test.

Figure 2.46: Data acquisition unit

2.32 Platen Alignment

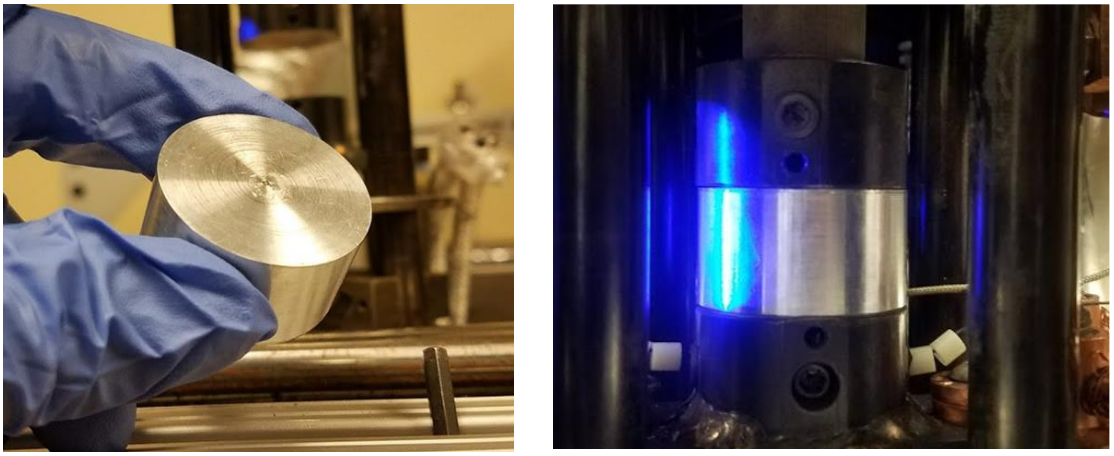

Figure 2.47: Alignment puck to keep faces of the compression platens parallel

To ensure that the top and bottom platens are aligned so that their faces are parallel with each other, alignment pucks were made. The pucks were turned from an aluminum round bar stock and were measured with calipers to be of a uniform height (maximum of 0.5 mm difference in height difference as measured across the diameter of the puck). Multiple alignment pucks were made that roughly corresponded to the heights of the samples.

The puck alignment process is as follows: It is first placed on the bottom platen. Next, the fully assembled top frame assembly is lowered so that the top platen touches the top face of the alignment puck. Finally, the top assembly is tightened onto the load frame, tightening onto the alignment puck. The bottom platen is lowered allowing the alignment puck to removed, leaving the faces between the top and bottom platens parallel and aligned. If any further adjustments are necessary, they can be made by adjusting the alignment collar on the load frame.

2.33 Rubber Blank and Prescale Check

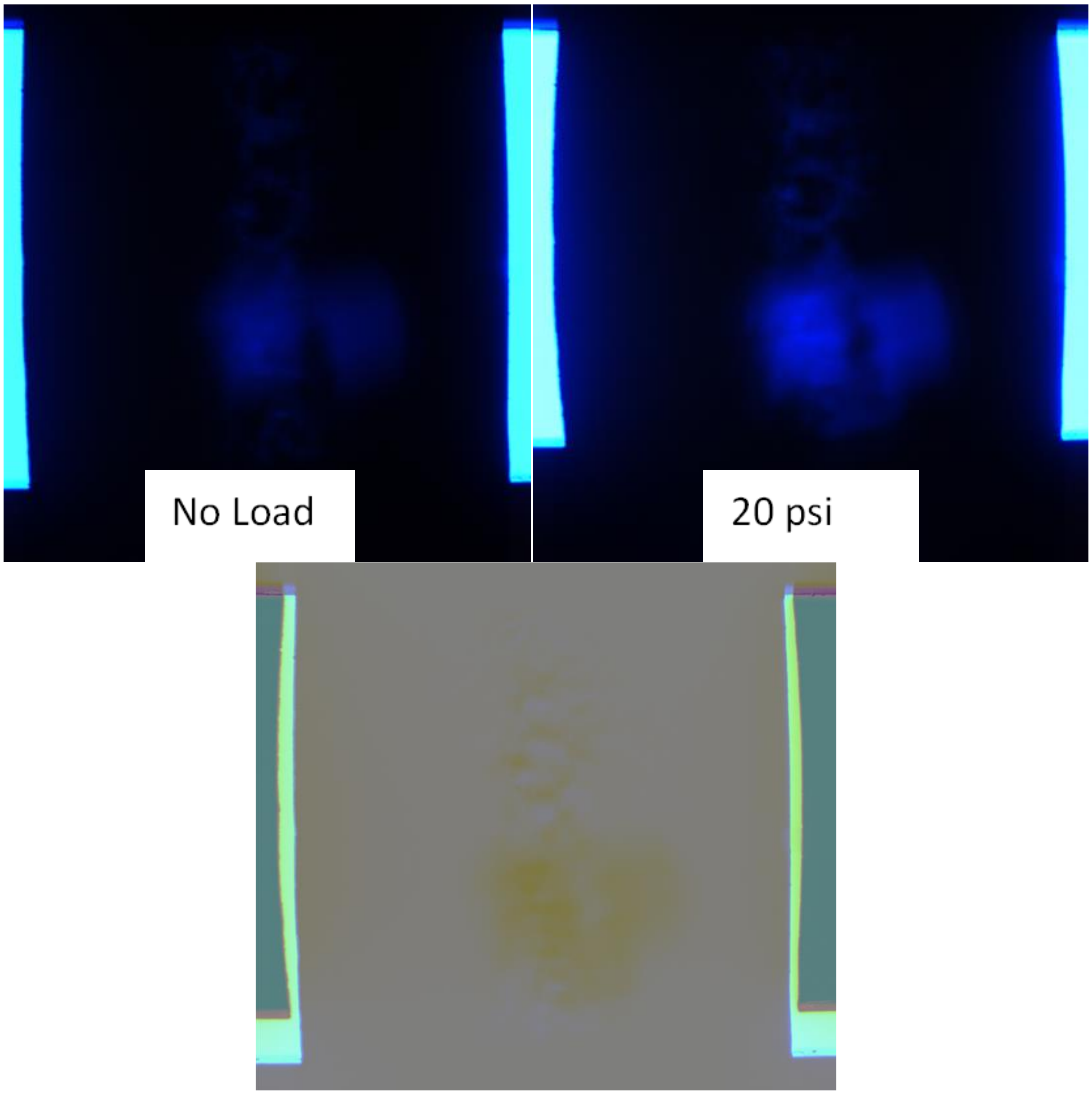

Figure 2.48: Rubber blank as viewed from the telecentric camera

To check for alignment accuracy, a rubber pellet blank roughly the size and diameter of a creep pellet sample was cut. The rubber pellet blank is centered on the pellet and compressed. The image of the blank is compared before and after and checked for symmetry.

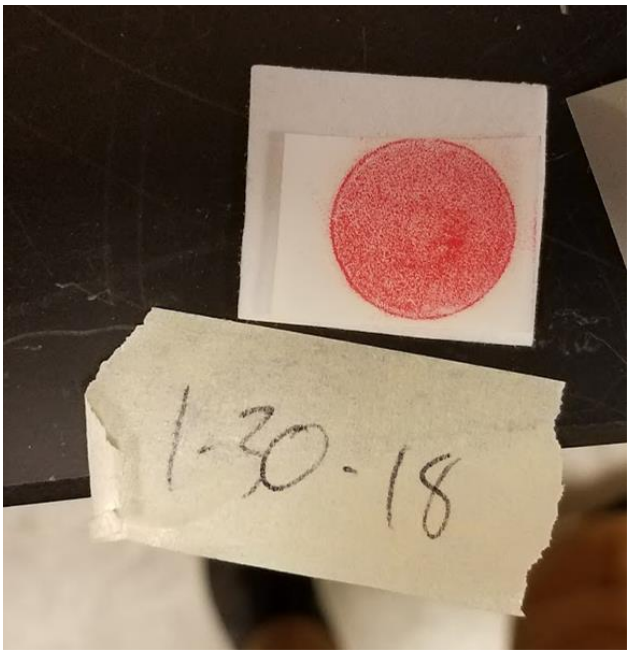

Figure 2.49: Prescale film results (from sample 161214a setup)

In addition, pressure sensitive prescale film allows for a full field measure of the pressure distribution of the compression platens. The higher the pressure in an area the deeper the color. Low pressure prescale (useful to 2.5 ~10MPa) was used. [41] The prescale is compressed by the platens and the color distribution due to the pressure from the compression is transmitted to the prescale film. The platens are aligned using the adjustable bottom collar and the top holding plate until the shadow image of the compressed rubber blank is symmetrical and the prescale color distribution is evenly red.

After these alignment tools, the platens are considered to be aligned. It is possible that as the test progresses the heat and applied load can disrupt the alignment. As such, before each pellet is tested, the loading frame is re-aligned.

2.34 Sample Alignment

Figure 2.50: Pellet alignment puck

A 3D printed pellet alignment puck was created to facilitate insertion of the pellets onto the center of the platens. The pellet alignment puck is sized to the diameter of the bottom platen and allows for the pellet to be placed in the center of the platen.

2.35 General Procedures

After sample insertion, the radiation shield is lowered over the sample and the guard heaters are installed into the platens. Thermocouples are inserted into the platens as well. Special care must be taken to separate the electrical connectors from touching the guard heater circuit.

The telecentric camera cart is then focused on the pellet by moving it forward or backwards on the camera-telecentric track; it is then fixed in place via shaft collars. It is then connected to a PC that captures a shadow image at predefined intervals and does not move during the test. The telecentric illuminator is placed on the same track as the camera and pointed towards it. The pyrometer is sighted to the sample through the pyrometer viewing window.

Figure 2.51: Image capture computer with camera sighted on sample (sample 150813b)

The system is sealed by closing off all ports and attaching all necessary vacuum pieces. Sensing equipment is then turned on to record the test. The DAQ is turned on and set to record.

The vacuums are then turned on. The roughing pump is the first stage vacuum that removes the majority of the atmosphere in the test chamber. An automatic switch turns on the turbomolecular pump when the pressure is low enough for it to activate. The vacuums run overnight before any heating or loading takes place to reduce contaminants that remain in the test chamber.

The sample is then heated and loaded. Using the temperature controller box and the pyrometer input, the sample is automatically heated at 3 °C per minute. At the same time, the active guard heaters are turned on. The sample is then loaded manually at approximately 2 lbf/min. This process continues until the set load is achieved.

Chapter 3 Results and Discussion

3.1 Pellet Data

Data for all tests are shown. All data shown start after the sample is loaded and heated to the initial testing conditions. Representative images of the sample are shown after the strain history plots.

3.2 150813a

The strain vs history graph of sample 150813a is shown Figure 3.1. This was the first successfully crept sample of all the tested pellets the straight line seen between 310-370 hours on the dashed line is an estimation of temperature. It was during this time the pyrometer emissivity ratio was being calibrated to the U_3Si_2 Tile. All values for this test, however, were back calculated and are based off of that calibration.

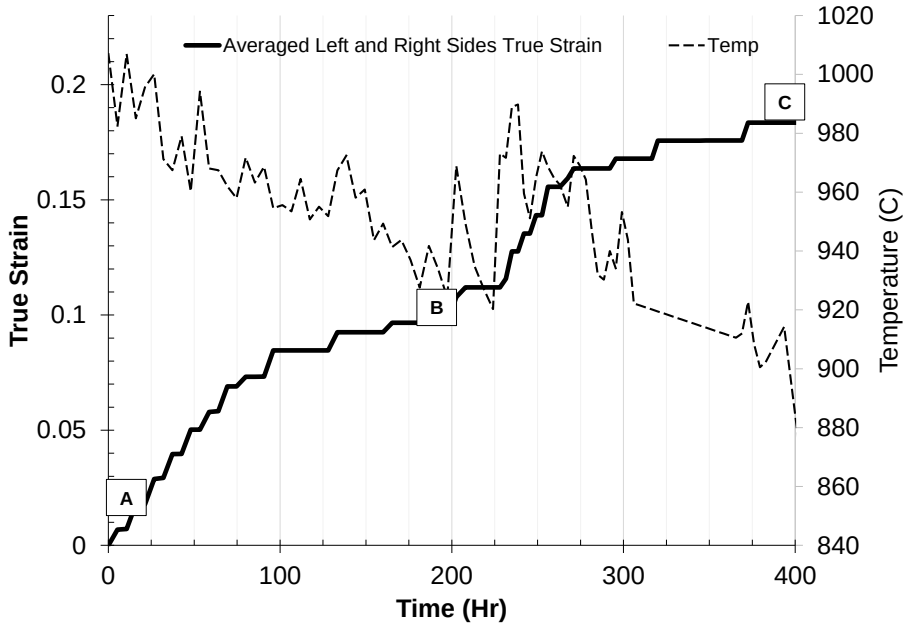

Figure 3.1: 150813a strain time and temperature history

Sample 150813a was tested before the closed loop temperature controller was implemented. As such, the strain time history graph appear to show clear areas of primary and secondary creep but this is believed to be due to the temperature variations. A faster strain rate (the slope of the solid line) can be readily seen in hours 0-100 and 200-260 but these directly occur when the temperatures was higher at that time. It is believed that the faster strain rate is due to these higher temperatures. A more detailed analysis of this is provided later in the report.

The shadow images of 150813a are shown in Figure 3.2. The letters correlate with Figure 3.1. The notches from this batch are differently shaped due to differences in EDM wire size.

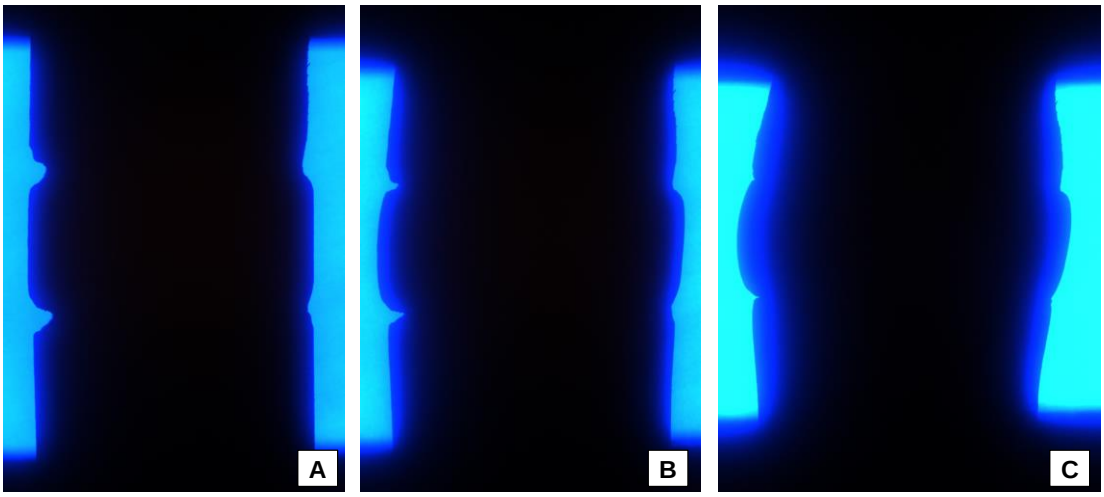

Figure 3.2: 150813a shadow images. A: Start of test, 980°C, 40MPa B: 210 hours, 990°C, 40MPa C: 400 hours, 900°C, 60MPa

As seen in Figure 3.3, sample 150813a was strained up to 18% vertical strain before a transformer failure abruptly stopped the test. Diametral strain rates remain below vertical strains and appear to follow the same sensitivity to temperature as described earlier.

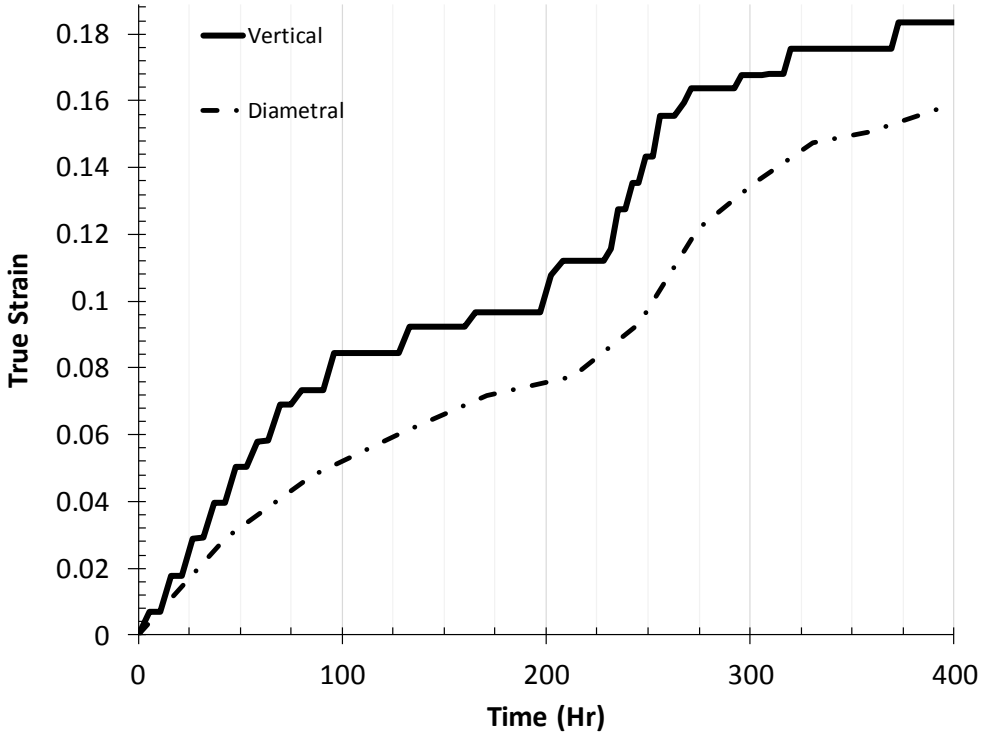

Figure 3.3: 150813a Diametral vs vertical strain history

3.3 150813b

Sample 158013b was the final creep pellet tested before the closed loop temperature controller was implemented. Similar sensitivity to the temperature transients can be seen between 790-830 hours in Figure 3.4. This sample was strained to the highest vertical strain of all samples tested. Low temperature (~850°C) and high stress conditions was chosen for the first set of testing conditions as seen 0-800 hours; the flat portions of the vertical strain line (hours 300-500, 550-790) are likely due to the small deformations that could not be readily captured by the optical system. However, a general trend can still be seen for the testing conditions.

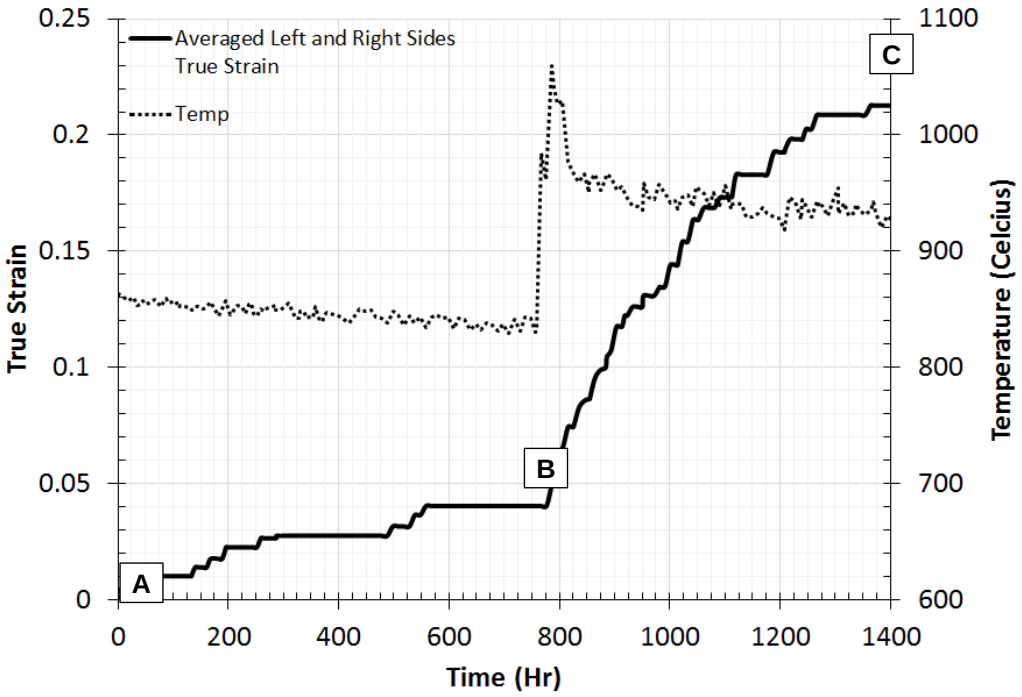

Figure 3.4: 150813b vertical strain time history

As seen in Figure 3.5, sample 150813b was imaged in its entirety (as opposed to other samples where the radiation heat shield obscured parts of the top and bottom).

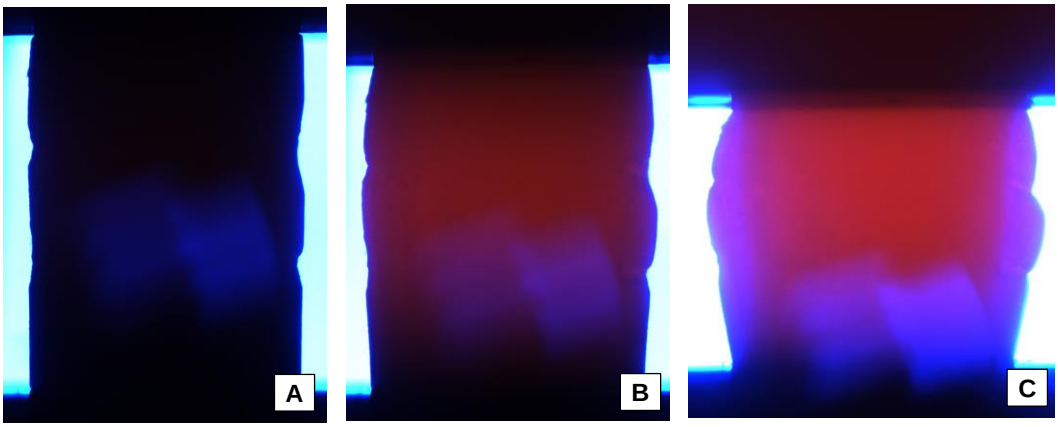

Figure 3.5: 150813b shadow images A: Start of test, 850°C, 70MPa B: 800 hours, 970°C 70MPa C: 1400 hours, 950°C, 50MPa

Pressure and true stress for 150813b are shown in Figure 3.6. The decreasing stress line (solid black line) between hours 800-1400 are due to the increasing area of the sample; as the load was still kept constant, the true stress decreased.

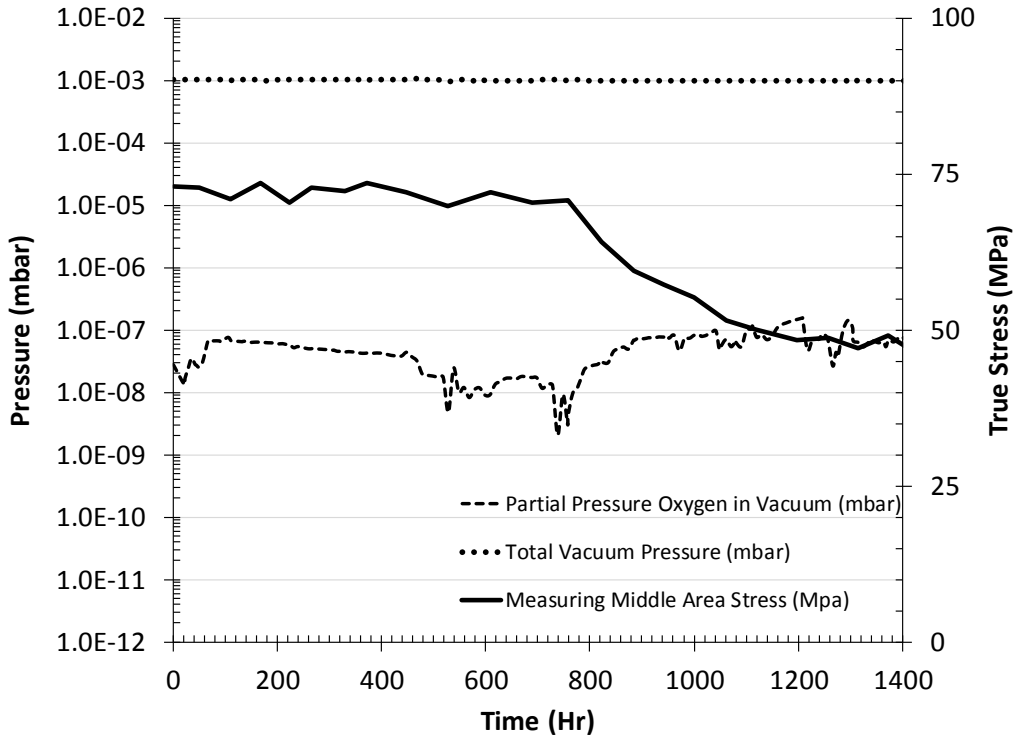

Figure 3.6: 150813b pressure history

Oxygen partial pressure appears erratic around hour 775 as seen in the long dashed line. This can be attributed to the increasing of the temperature condition at that point from 850 °C to 950 °C; the increase in temperature would increase the gettering effect in the chamber.

Diametral strain vs time history is plotted with the vertical strain history of sample 150813b in Figure 3.7. It follows the same trends of 150813a in that it appears sensitive to temperature (as seen from the strain rate in hours 790-820) and is fairly close to the vertical strain values.

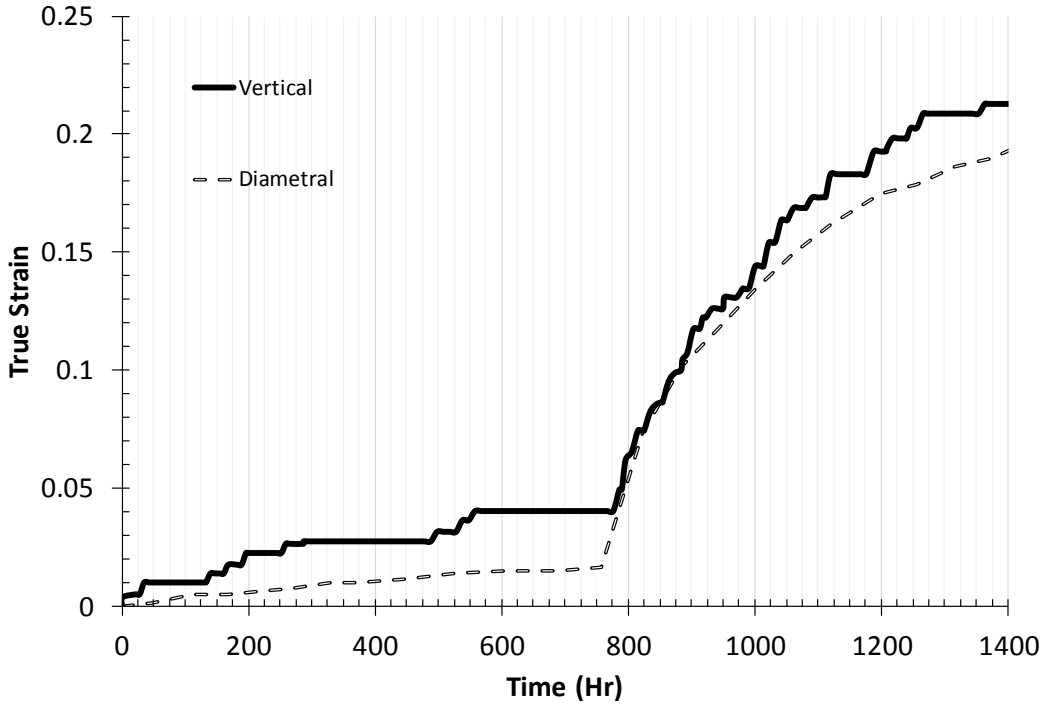

Figure 3.7: 150813b diametral and vertical strain history

Diametral strains are similar to 150813a pellet and remain lower than the vertical strain; the shape of the strain-time history curve is also comparable. Sample 150813b was ended early due to a power failure at approximately hour 1400. This was the impetus to install an uninterruptible power supply outlet for the test system.

3.4 161214b

Sample 161214b was the first sample that was tested with the closed loop temperature control installed. The temperature stability is much improved as seen Figure 3.8 via the dashed line and shows the two temperature testing conditions: 900°C and 950°C. The strain rate (the slope of the solid black line) increases due to this change in testing conditions and can be readily seen starting at hour 540.

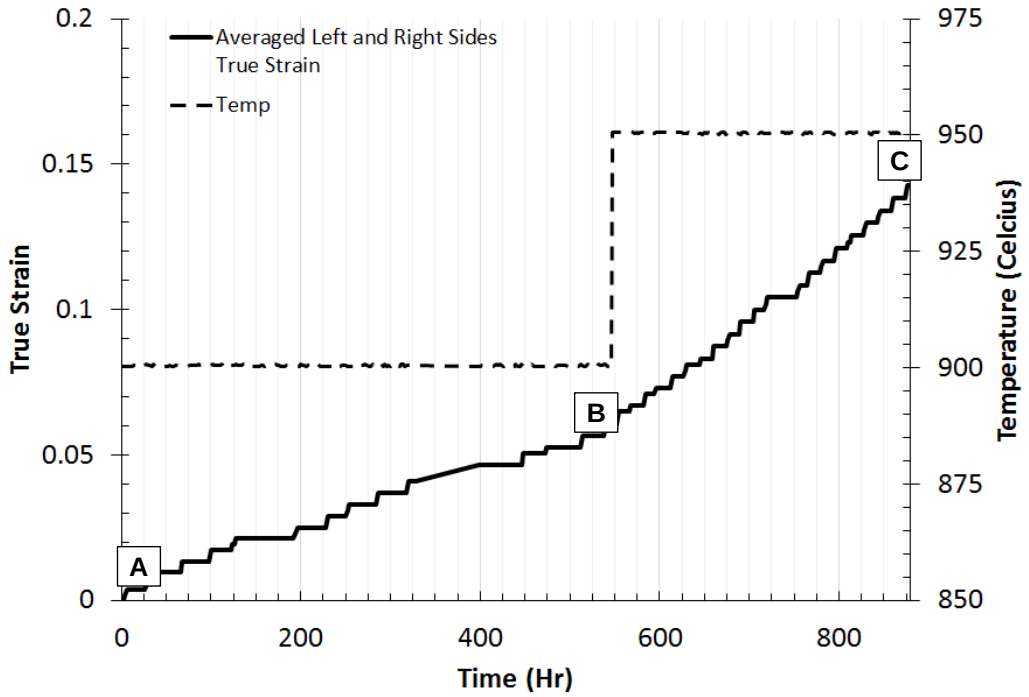

Figure 3.8: 161214b strain time history

During the hours 375-400, a camera system malfunction was noted in that the system stopped recording images. As such, there is a constant slope line during that period due to the lack of data for that time period; however, the slope of the line is still similar to the slope of the True Strain vs Time curve before it.

Sample 161214b is the longest sample tested. It began to exhibit a noticeable curve as can be seen in Figure 3.9 possibly due to misalignment of the sample or testing platens. Further samples were cut shorter to reduce this effect and to preserve pieces of the sample to archive the microstructure. The notches from this sample are amongst the smallest of the pellets tested and are due to a different EDM wire size used during cutting.

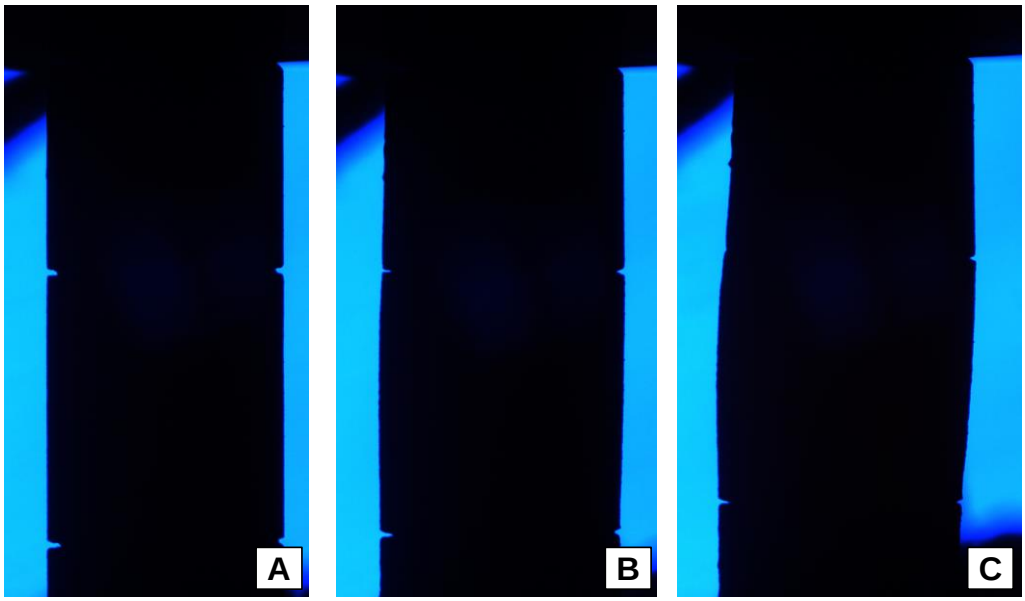

Figure 3.9: 161214b shadow images A: Start of test, 900°C, 50MPa B: 520 hours, 950°C 50MPa C:860 hours, 950°C, 50MPa

Pressures and stress history for 161214b is shown in Figure 3.10. There was one tested stress state (50MPa) and the slow decline is due to the increasing area of the pellet.

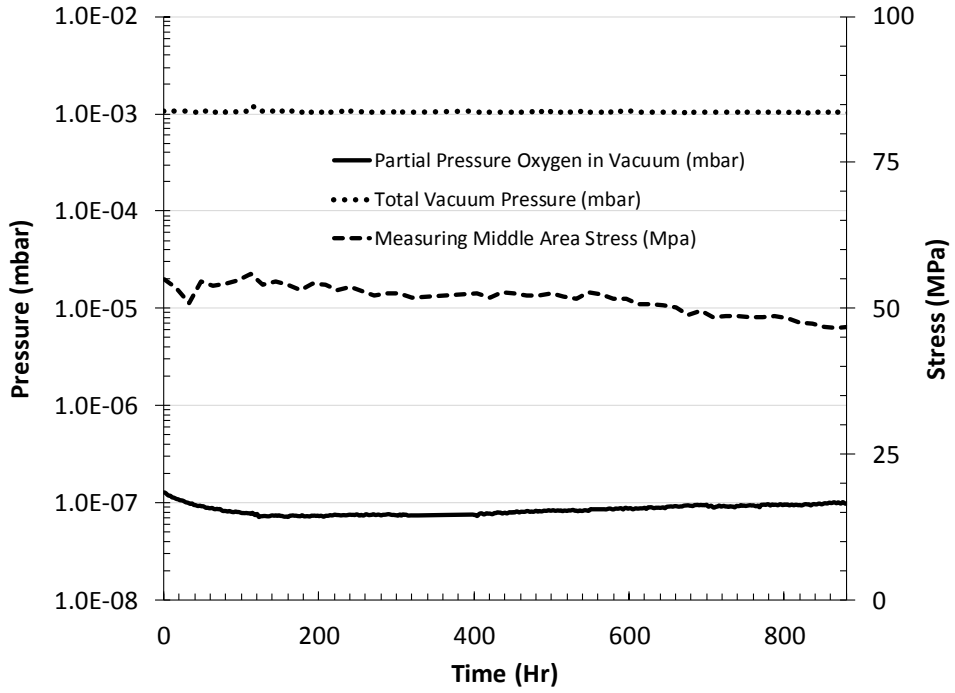

Figure 3.10: 161214b pressure history

The Diametral Strain history is plotted against the vertical history and shows similar behavior to the previous pellets.

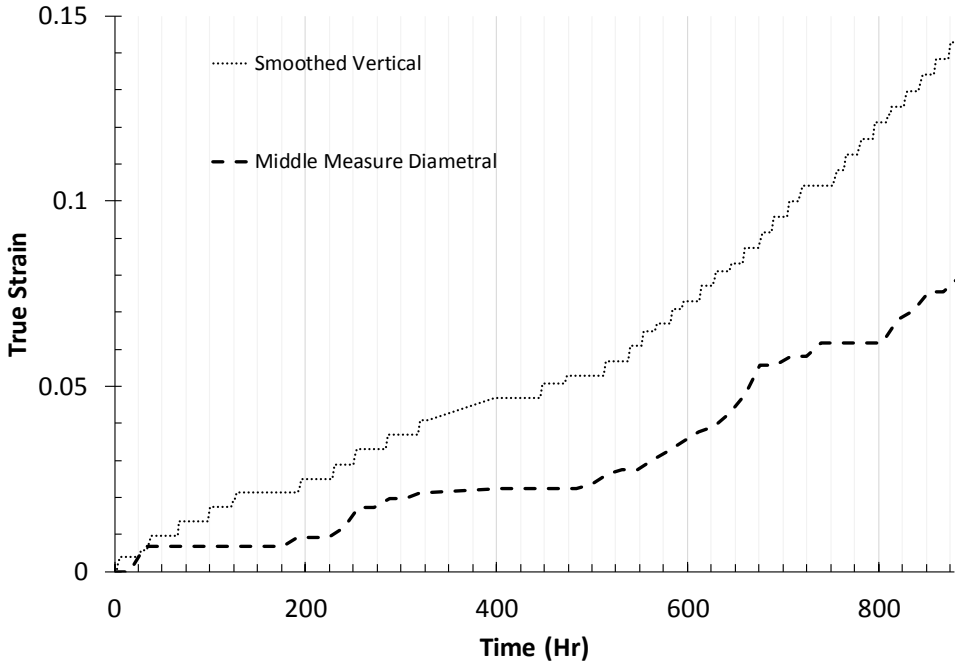

Figure 3.11:161214b Diametral vs Vertical strain history

As stated earlier, the sample began to show a large amount of curvature to it as shown in Figure 3.9 and Figure 3.12. The test was stopped early due to concerns that the non-uniform compression state would not be accurate enough of a uniaxial compressive force. As such, some data from this test was not used and the data up until the sample reached the maximum curvature as seen in Figure 3.9 is reported.

The final shape that the sample reached is shown in the figure below. The cord as seen in the top left of the image is a shadow of the thermocouple used during the test.

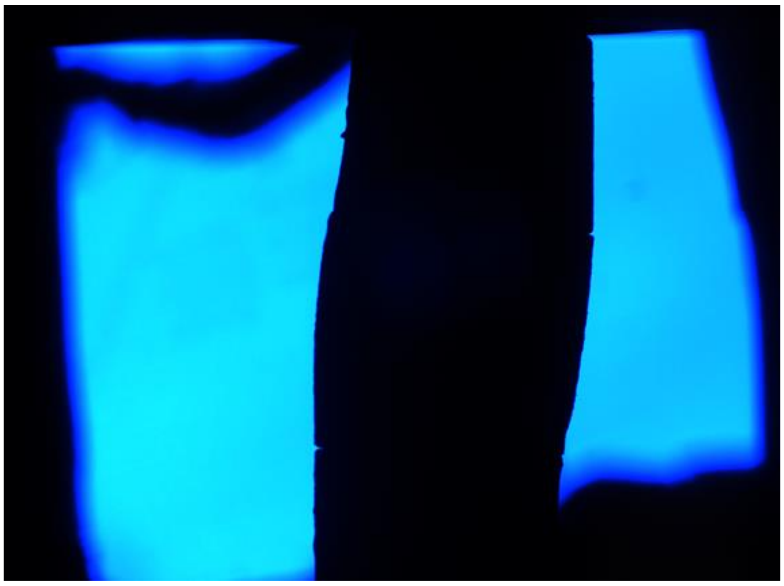

Figure 3.12: Maximum curvature in 161214b at the end of test

3.5 161214a

Sample 161214a had multiple stress profiles as seen in Figure 3.13. The strain rate (slope of the solid black line) can be seen to readily increase with each step up in stress (dashed line).

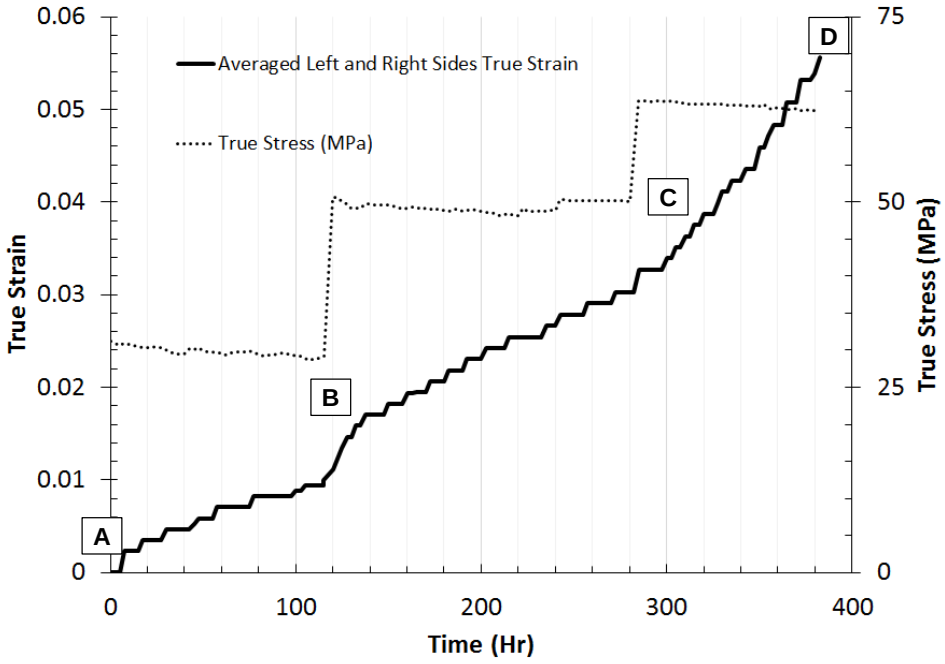

Figure 3.13: 161214a strain time history

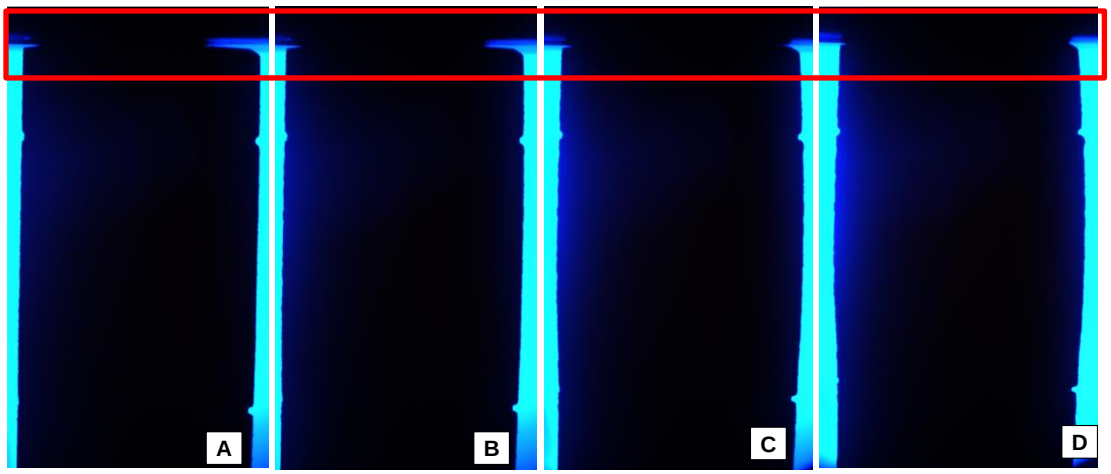

Figure 3.14: 161214a shadow images. The red box highlights the contact area between the sample and the platen. A:Start of test, 950°C, 30MPa B: 125 hours, 950°C, 50MPa C: 290 hours, 950°C, 70MPa D: 400 hours, 950°C, 70MPa

The sample was originally longer than tested. The top of the sample was cut off with a diamond saw to characterize the microstructure of the pellet before creep testing to provide a basis for optical and SEM comparison. As such, the top face of the sample (which is in contact with the compression platen) is not completely square; this can be seen in the red box in Figure 3.14. However, as the test progresses, the sample begins to creep and deform into the platen, essentially seating them with each other.

The sample was tested at one temperature, 950°C, as can be seen in the dashed line in Figure 3.15. The oxygen partial pressure line (solid black line) appears different than previous samples because an extended (three day), high temperature seating process (in where the sample was allowed to deform into the top platen at at least 850°C) was done on this pellet before applying the first stress state to account for the un-levelness of the cut face. It is expected that the high temperature environment provides a gettering effect which levels off with enough time.

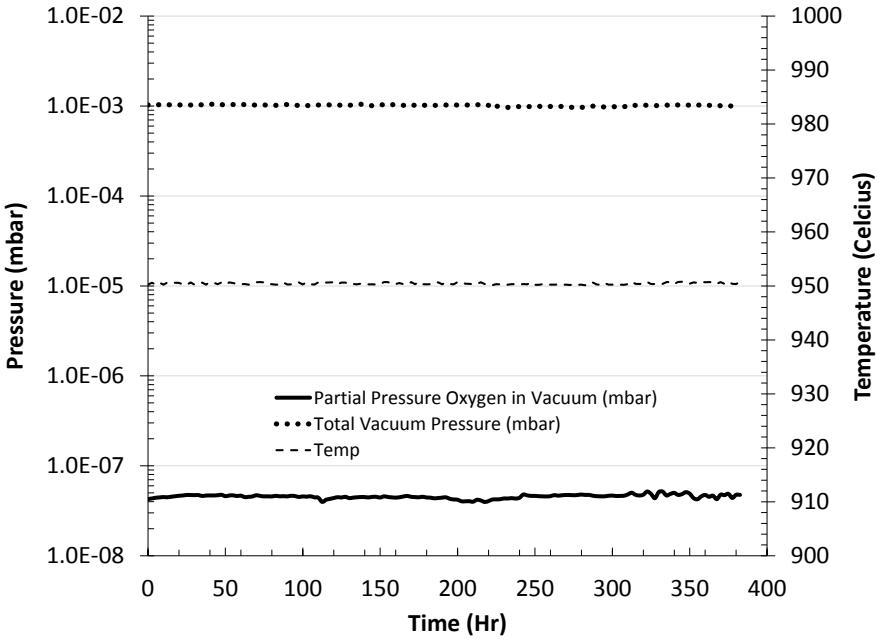

Figure 3.15: 161214a pressure history

The sample showed similar diametral strain behavior compared with the other samples tested as can be seen in Figure 3.16. It was shown to be slightly higher at some points such as at hours 80 and 300 but generally still follows the same response.

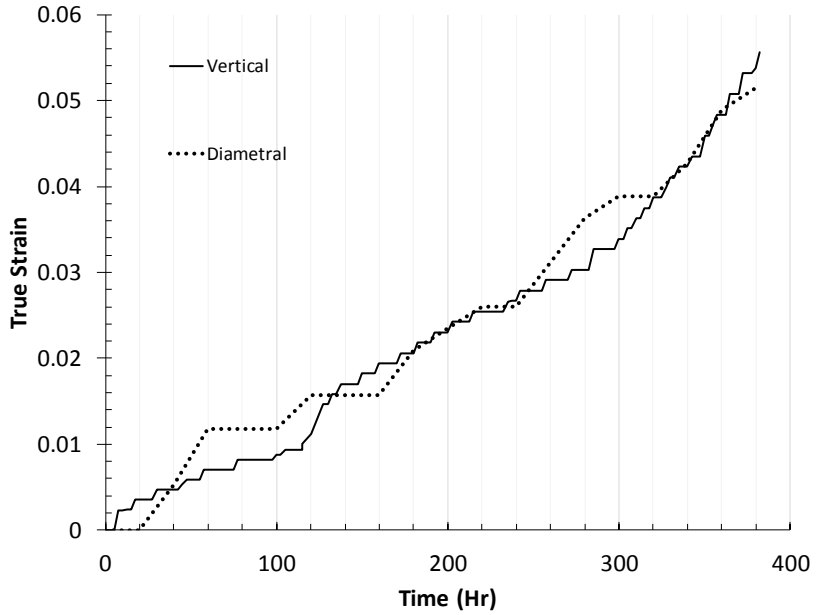

Figure 3.16: 161214a diametral and vertical strain history

A malfunction of the backup power supply installed earlier abruptly stopped the test. The sample cooled down at room temperature but was still under the 65MPa load when this was discovered. However, it was still intact upon unloading.

3.6 161214c

Sample 161214c was the final sample tested in this report. Two stress states were tested as can be seen in Figure 3.17: 28MPa and 48MPa. In addition to the two stress states, two temperature states were tested as can be seen in the dashed line in Figure 3.19, 950 and 1000°C.

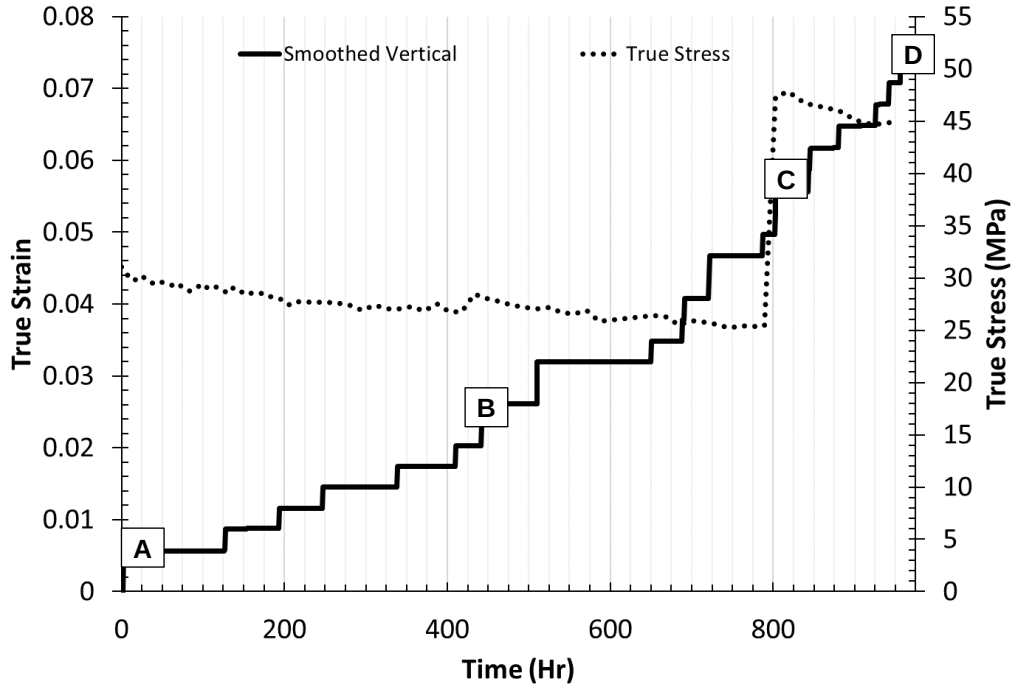

Figure 3.17: 161214c strain time history

Shadow images for 161214c are shown in Figure 3.18. The notches on this sample appeared deeper than other samples from the same batch.

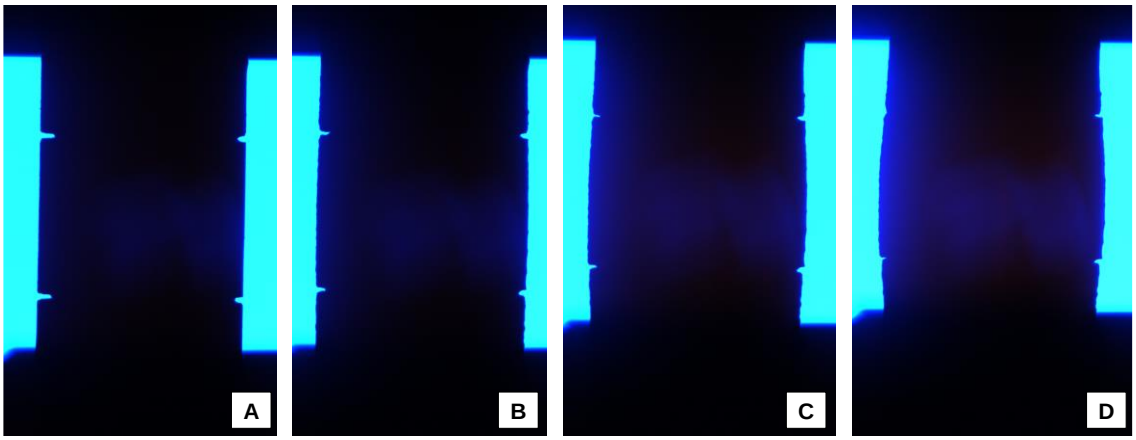

Figure 3.18: 161214c shadow images A; Reference, 950C 30MPa B 400 hours, 950°C 30MPa C: 800 hours, 1000°C, 45MPa D: 900 hours, 1000°C, 45MPa

The pressures and temperature for this sample are shown in Figure 3.19. There are two temperature conditions tested: 950 and 1000°C.

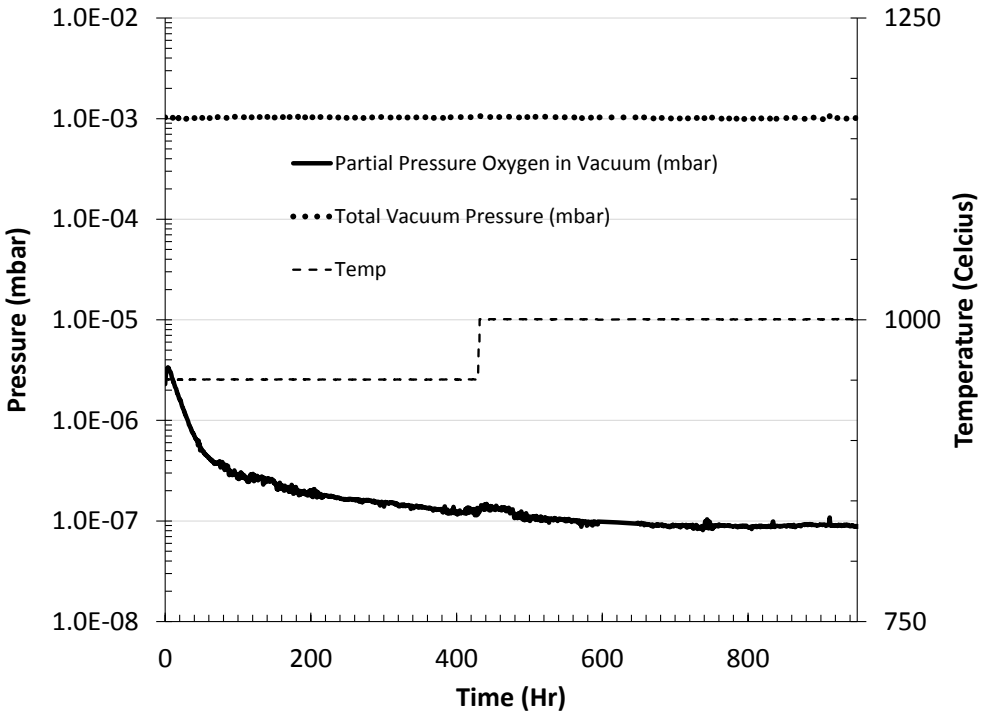

Figure 3.19: 161214c pressure history

The partial pressure of oxygen (thick black line) levels out at 200 hours and is likely due to the oxygen gettering effect of the hot testing environment (platens, internal copper

wires, etc.). At elevated temperatures and times, free oxygen in the testing chamber will be absorbed into these hot surfaces; this shows up as a lowered oxygen partial pressure as reported by the Zirox partial pressure monitor.

The diametral strain vs time is plotted against the vertical strain in Figure 3.20 and shows a similar strain rate history compared to the other samples.

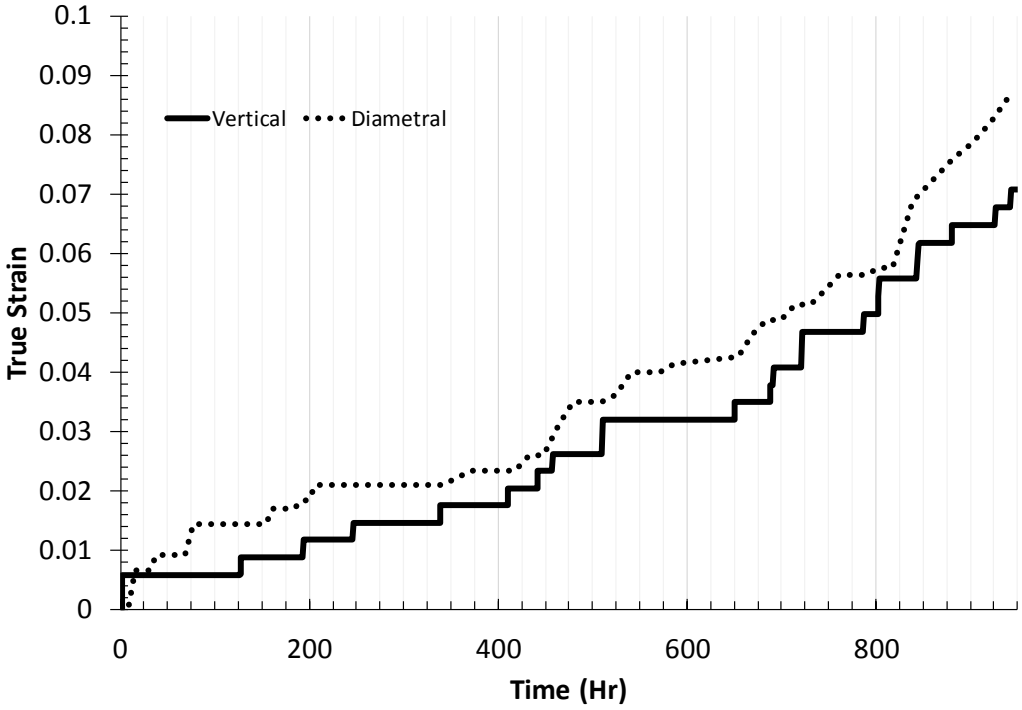

Figure 3.20: 161214c diametral vs vertical strain history

3.7 Closed Loop Temperature Control Effect

Closed loop temperature control was not yet implemented for pellets 150813a and 150813b. As such, for the strain-time history data, it appears that there are clear demarcations between primary creep and steady state creep. However, this is believed to be due to the steady drop in temperature after setting an initial temperature. Detailed views of the open loop temperature controlled pellets are shown below.

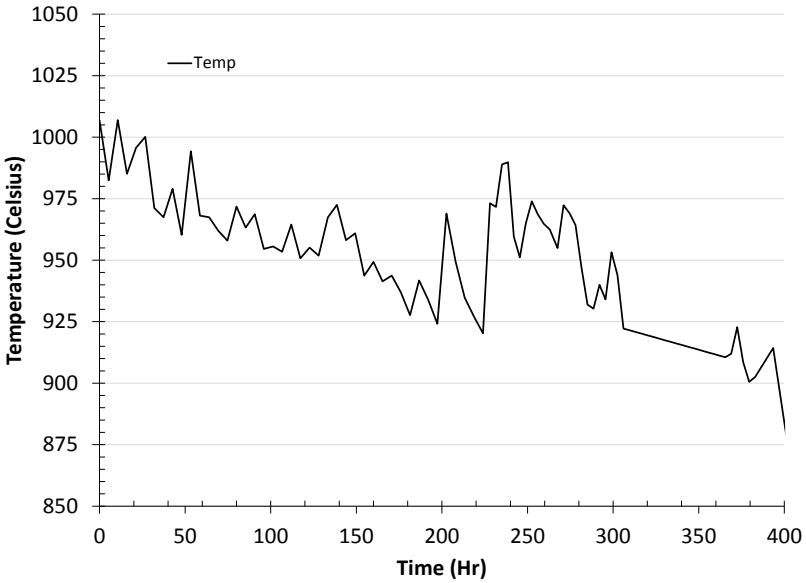

Figure 3.21: 150813a Temperature Detail

As stated before, the straight line in hours from 300 to 350 is interpolated data as the pyrometer was being calibrated during this period. Open loop temperature control data is also provided from sample 150813b.

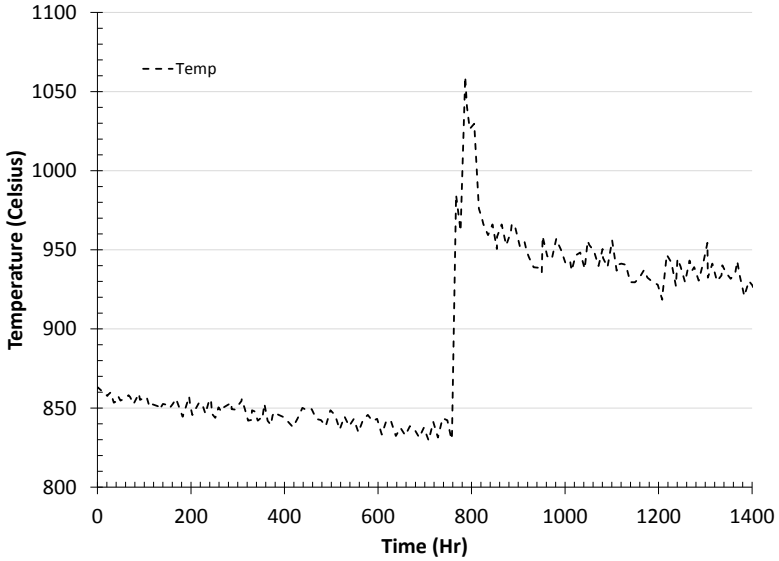

Figure 3.22: 150813b Temperature Detail

Before the implementation of the closed loop controller, temperature conditions were coarsely set via a VARIAC variable transformer. After setting the initial temperature condition, it was observed that the temperature would slowly decrease (~2°C per day) until it reached a steady state temperature. It would then oscillate around this temperature. This steady drop in temperature and oscillation was the impetus to build and implement the temperature controller.

To account for these effects, the temperature was set to a higher value than the target temperature so that the system would "settle" into the set temperature condition. This effect can be readily seen in Figure 3.22 at hour 800 where the target temperature was actually 950°C but the system was initially set to 1100°C knowing that it would settle down in the 950°C range.

These higher temperature conditions were seen correlate with a faster strain rate as can be seen in the strain-time history plots for pellets 150813a and 150813b in Figure 3.1 and Figure 3.4.

For samples 161214b, 161214a, 161214c, the closed loop temperature controller was implemented and provided a more stable temperature testing conditions as seen in Figure 3.23. All changes in temperature testing conditions with the closed loop temperature box occur at 3°C/minute and it wile it appears that the transition between temperature states was instantaneous, it is an effect of the time scale used. Detailed looks into the data have verified the 3°C/minute heating and cooling rates.

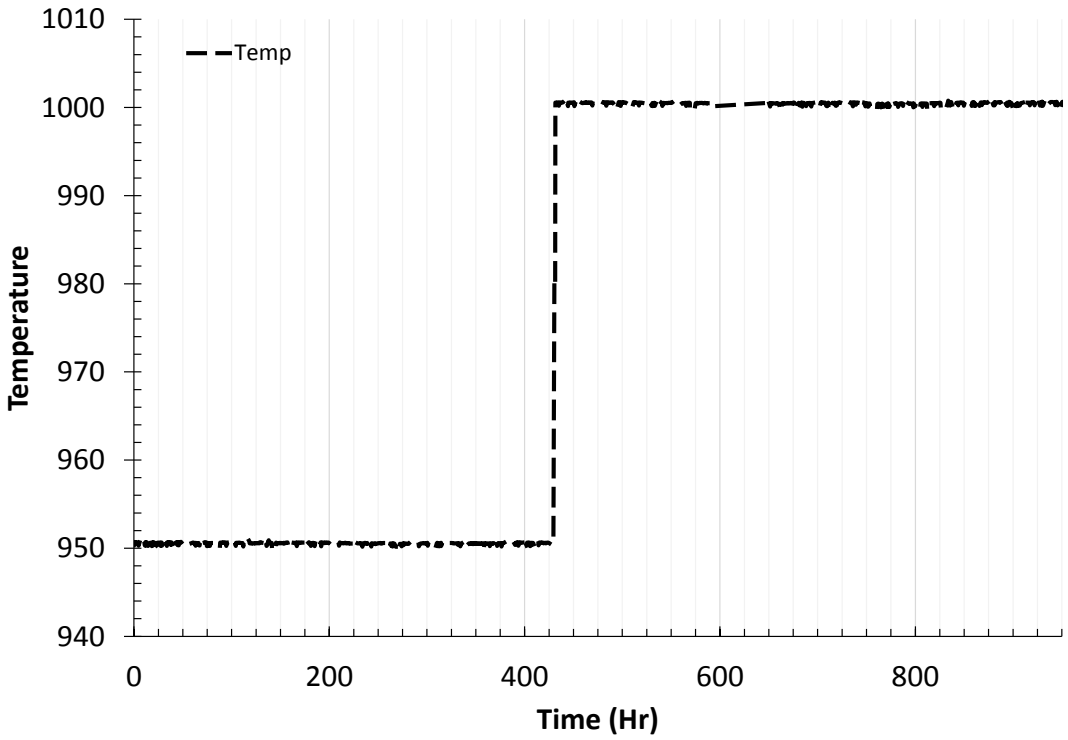

Figure 3.23: 161214c Closed Loop Temperature Detail

3.8 Discussion of Results

A summarized list of results of the steady state true strain rate (axial) and testing conditions are shown in Table 3.1.

Table 3.1: Creep Test Results

	Test Number	Start Time (Hr)	End Time (Hr)	Vertical Strain Rate (1/hr)	Diametral Strain Rate (1/hr)	Average Temp (C)	Average True Stress (MPa)
150813a	1	144	231	2.78E-04	2.83E-04	943	43
	2	345	420	1.60E-04	2.65E-04	904	64
150813b	3	254	760	3.68E-05	2.05E-05	843	72
	4	804	893	4.51E-04	4.29E-04	973	68
	5	1062	1400	1.49E-04	1.61E-04	937	50
161214b	6	183	548	9.64E-05	4.90E-05	900	53
	7	660	884	2.54E-04	1.29E-04	950	49
161214a	8	42	120	6.10E-05	1.51E-04	950	31
	9	175	284	9.25E-05	1.29E-04	950	51
	10	356	380	3.00E-04	2.53E-04	950	64
161214c	11	144	430	3.99E-05	3.04E-05	951	27
	12	551	792	7.81E-05	7.50E-05	997	26
	13	846	954	1.07E-04	2.13E-04	1,000	46

In Table 3.1, it is seen that U_3Si_2 readily creeps in the temperature ranges starting as low as 850°C. High compressive strains were reached (such as seen with 150813b with up to 20% axial strain) with the samples visibly showing the effects of barreling as seen in Figure 3.2 and Figure 3.5. To account for these changes in cross sectional area (and thus reduction in stress), true stress is calculated by calculating instantaneous area. Diametral strain rates are generally lower but similar to axial strain rates.

The data is plotted below and grouped by sample number in Figure 3.24 and grouped by temperature in Figure 3.25. As expected, increasing the stress on the pellets causes an increase in the true strain rate. When temperature is increased in the same sample, the same trend is observed as seen in Figure 3.24.

However, there is scatter in the data when comparing strain rates across samples as seen in Figure 3.25. For the 50 MPa data, the 1000°C strain rate (the highest temperature tested) is below some tests that are at 950°C. It is expected that inter-pellet variability is the major factor in the difference.

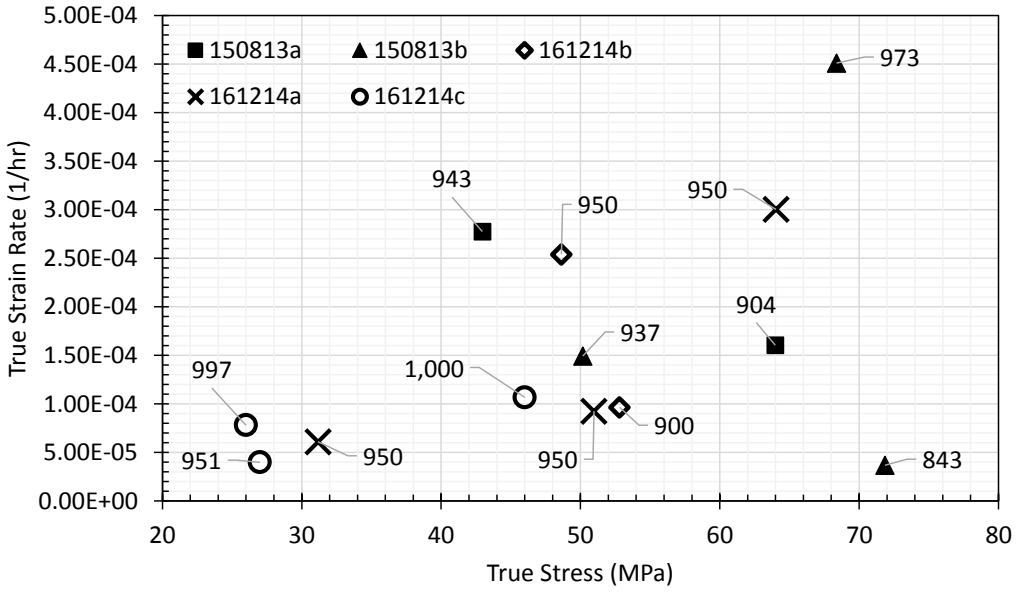

Figure 3.24: Plotted results of Table 3.1 grouped by sample

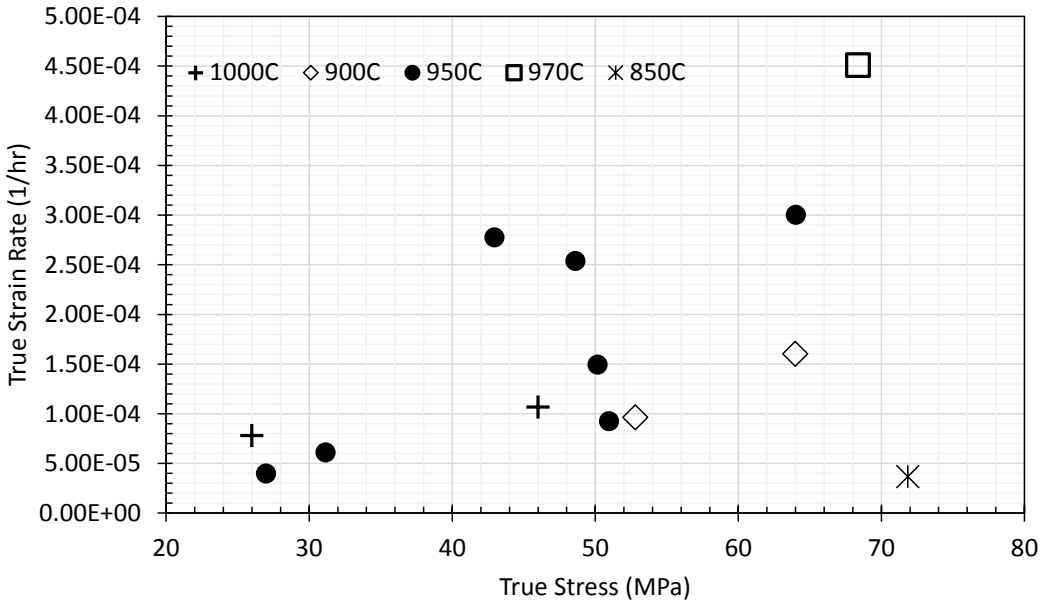

Figure 3.25: Plotted results of Table 3.1 grouped by temperature.

At oxygen partial pressures (1E-7 mbar) and elevated temperatures, the U_3Si_2 pellets did not react violently with the environment. However, after extended testing, a dull-colored, thin surface layer was observed to have formed. This layer began to spall off the bulk of the material upon cooling down from testing temperatures.

Upon unloading and removing the sample, it revealed a shiny material as seen in Figure 3.26. The surface is likely due to reactions of the imperfect environment with the pellet surface, coupled with extended testing times and high temperatures.

A typical picture of what the spalling effect looked like is provided in Figure 3.26. Note the dull colored skin at the top and bottom of the sample as well as a shiny inside layer that was typical of all pellets after testing.

Figure 3.26: Typical spalling effect after cooldown of samples (161214c)

From the steady state strain data from Table 3.1 and the least squares regression method discussed earlier, the values of A, n and Q for the Arrhenius equation for steady state creep rate were found and are provided in Table 3.2.

Table 3.2: Steady State Creep Rate Equation Coefficients

A	8.78E-16	
n	1.94	
Q	168.68	kJ/mol
	3.50E+00	eV
	5.60E-19	J

Values in Table 3.2 use all the data points taken from the tests to determine the values.

3.9 Determination of Creep Activation Energy and Stress Exponent

Values of Q and n can also be determined through plotting. As seen in Figure 3.27, for a test with similar stress testing conditions, the slope of the natural log of the strain rate vs the inverse temperature can give the activation energy.

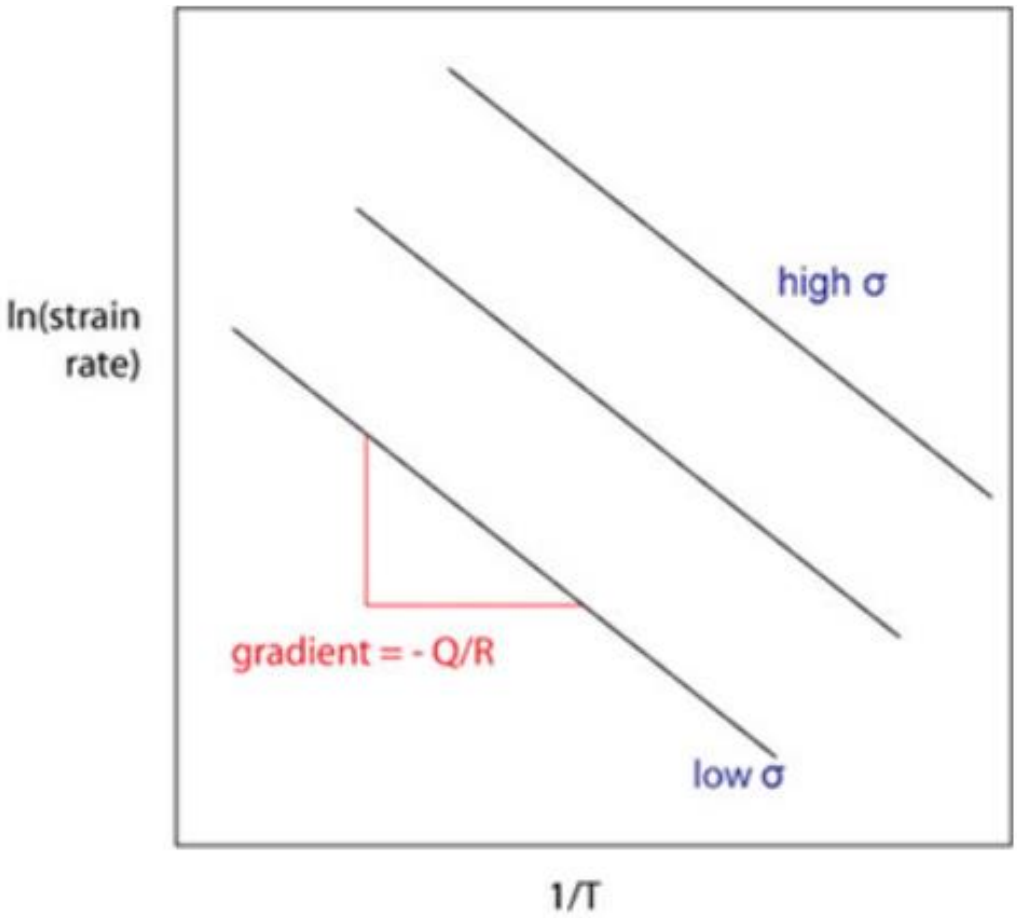

Figure 3.27: Finding Q with similar stresses [42]

In the same manner, for tests with similar temperature conditions, the stress exponent can be determined through the gradient of the natural log of the strain rate and the natural log of stress as seen in Figure 3.28.[42]

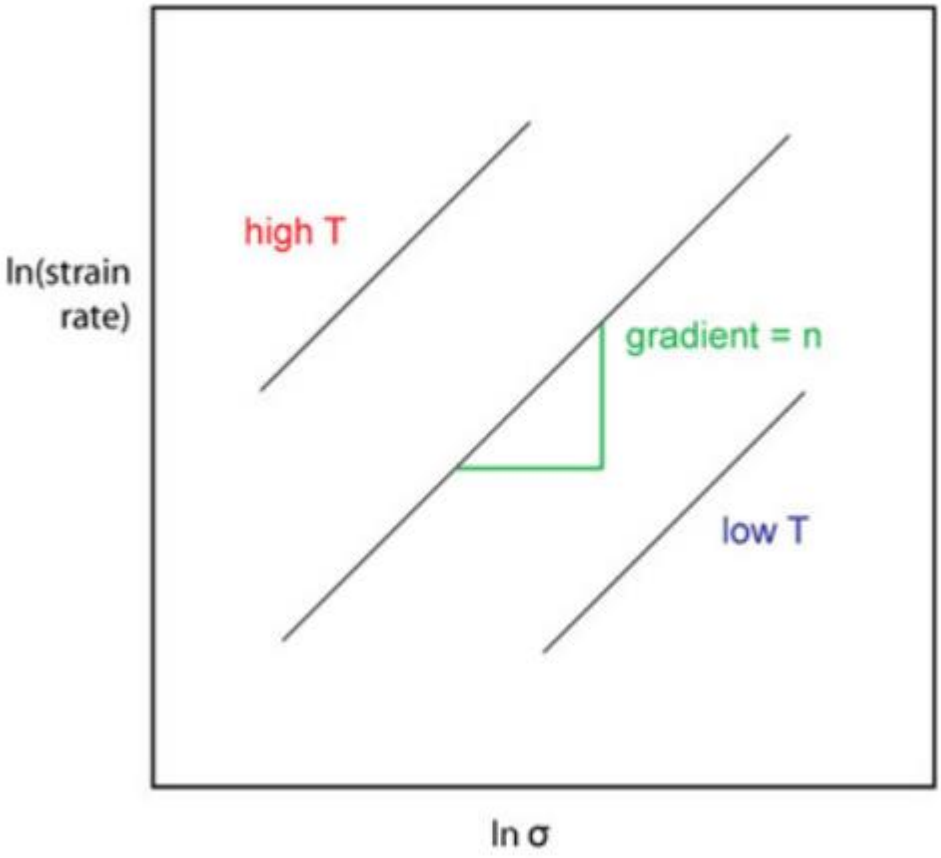

Figure 3.28: Determination of n with similar temperatures [42]

This method can be used to determine the values of the activation energy and the stress exponent from the same test and pellet and compare it with the value obtained with the least squares regression (LSR) method. Keeping an analysis within the same batch reduces the effects from a microstructure difference between pellets. For completeness, an analysis of n and Q between pellets is also provided.

The values of the activation energy can be determined with samples 150813b, 161214c, and 161214b due to similar stress values (within a 10 MPa difference). The results are below.

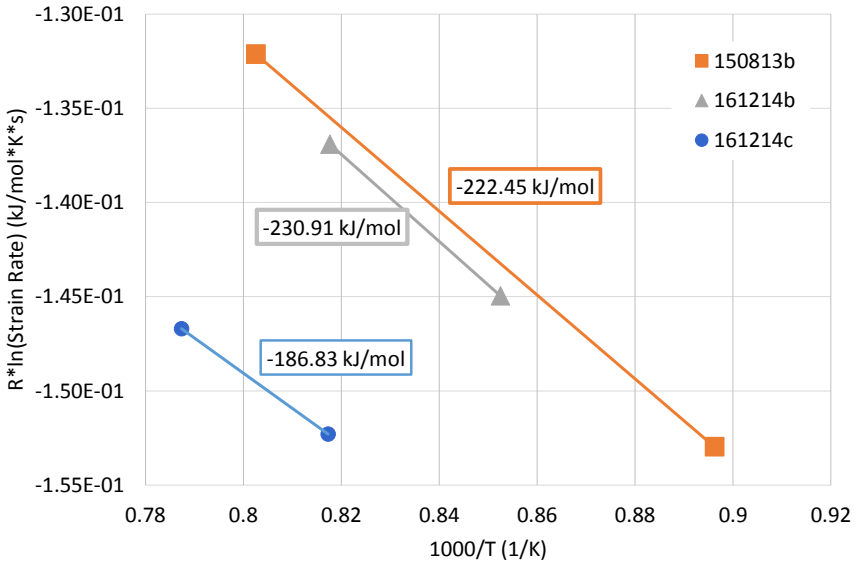

Figure 3.29: Same pellet Q determination

The value of the activation energy taken from the same sample are in reasonable agreement with each other, with a range from 186 kJ/mol to 230 kJ/mol, as seen in Figure 3.29.

When combining data from separate pellets, the Q value can also be determined for data with similar stress states. The results are below in Figure 3.30

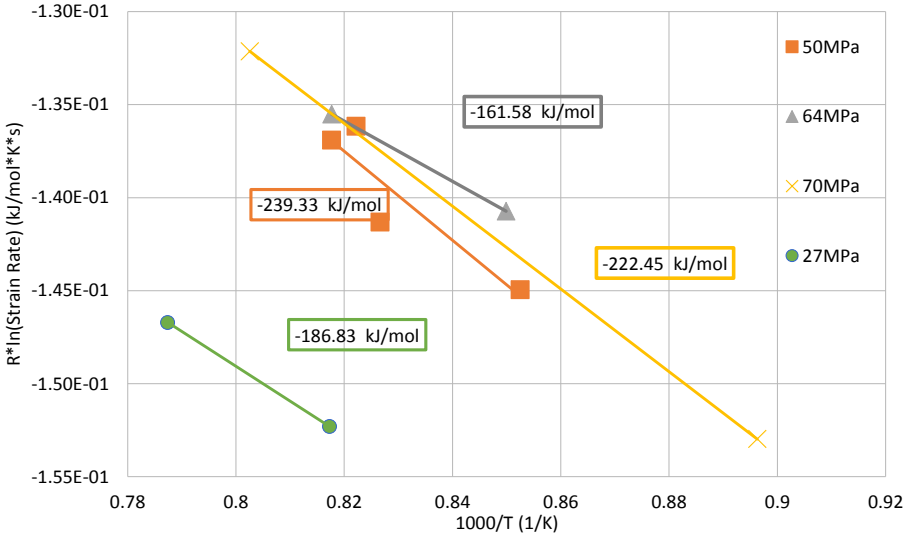

Figure 3.30: Between samples Q determination

The values of Q between samples are again within reasonable agreement with the LSR method with the smallest value being 161 kJ/mol and the largest being 239 kJ/mol. The general trend appears to be consistent with similar slopes between stress states.

In a similar matter, the value of the stress exponent, n, can be determined within the same samples when the temperature is similar and the stress difference is large enough. The results are below.

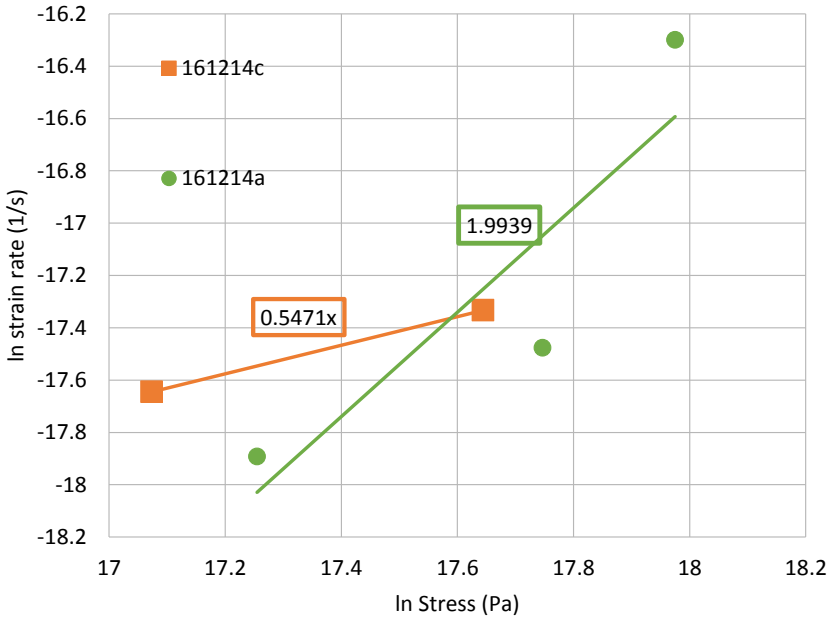

Figure 3.31: Determination of n within same samples

Within the same sample, the value of n appears to be reasonably close to the LSR method in the 161214a case but much lower for the 161214c case as seen in Figure 3.31. Both values still point to a relatively low stress sensitivity however, as it can range from up to 5 in some cases.

Between samples, the values of n are determined in the two sets of data (from the 950 °C tests and from the 900 °C tests) in Figure 3.32 below.

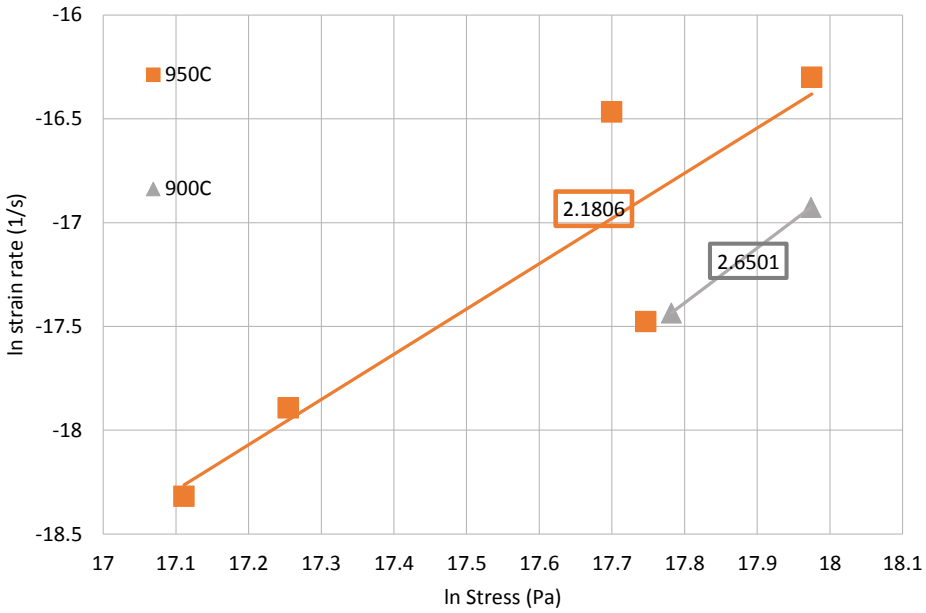

Figure 3.32: Determination of n between samples

The majority of tests were conducted at 950°C. Between these tests, the stress exponent of 2.18 was found. At 900°C, the stress exponent is slightly higher at 2.61 but still comparable. Altogether, the stress exponents between samples are relatively low (~2) and point to a low stress sensitivity.

3.10 Comparison to Previous Work

Previous work at USC [22] had modeled the creep rate of U_3Si_2 using data collected from the grain sizes of U_3Si_2 microstructure and sintering data. A modeling effort in BISON by Metzger modeled three regimes of creep that would be experienced by U_3Si_2 in reactor:

1) Athermal Creep Nabarro Herring Dominated Creep
2) Thermal Creep coble Creep
3) Thermal Creep Dislocation Induced creep

Each regime was separated by different temperature and stress conditions. The athermal creep was predicted to dominate up to 873°K while the Coble creep and dislocation creep (the thermal creep cases) were predicted to dominate above that temperature. The reasoning was that U_3Si_2 was expected to behave similar to Uranium Carbide (UC) in that it exhibits similar strong bonding characteristics. Furthermore, the transition temperature between athermal and thermal creep for UC was found to be .45 times its melting temperature. This was taken as the transition temperature for U_3Si_2 which corresponds to the 873K value from before.

For the Athermal creep regime, the following Nabarro Herring creep rate equation is used.

$$\frac{d\epsilon}{dt} = \left(\frac{12.5b^3\sigma}{kTd^2}\right) D_{ogb} \exp\left(\frac{-Q_{gb}}{RT}\right) \qquad \text{Equation 3.1}$$

When the normalized stresses (Von Mises stress divided by the shear modulus) was below 10^{-4}, the creep was predicted to be Coble and described by the following equation

$$\frac{d\epsilon}{dt} = \left(\frac{40b^4\sigma}{kTd^3}\right) D_{ogb} \exp\left(\frac{-Q_{gb}}{RT}\right) \qquad \text{Equation 3.2}$$

For normalized stresses above 10^{-4}, creep was predicted to be modeled by dislocation creep and modeled by the following equation

$$\frac{d\epsilon}{dt} = \left(\frac{6E7b\sigma^5}{kTG^4}\right) D_o \exp\left(\frac{-Q_L}{RT}\right) \qquad \text{Equation 3.3}$$

For the previous equations, the crystal structure was used to approximate the burgers vector, b. The structure is tetragonal and has two lattice parameters depending on

the axis; a=0.39nm and b = 0.73nm [37]. The burgers vector was taken as the average of these two and equaled 0.56nm. Boltzmann's constant, k, was taken as 1.38E-23 m^2kg/s^2K. Average grain size, d, was measured as 20um. Shear modulus, G, was taken as 67 GPa.

Two sets of data were used for the values for diffusion and activation energy– one obtained through an analysis of a U_3Si_2 tile (Sintering-based Model) and another from computational DFT data (Noordhoek DFT-based Model). They are provided in Table 3.3 below.

Table 3.3: Values Used in the Metzger Model [22]

	Sintering-based Model	Noordhoek DFT-based Model
Q_{gb}	9.97×10^{-19} J	2.28×10^{-19} J
Do_{gb}	2.365×10^{3} m^2/s	5.26×10^{-11} m^2/s
Q_L	2.00×10^{-18} J	4.57×10^{-19} J
Do_L	6.86×10^{24} m^2/s	4.63×10^{-6} m^2/s

The equations developed previously were used as input parameters in BISON. In the work, a 10 pellet stack was modeled under PWR reactor conditions with two cases: one where creep was neglected and one where creep was taken into account. This was done for values taken from the sintering-based model and values from the DFT-based model. The specific rod, assembly, temperature and dimensional specifications are provided for in Chapter 7 of the report.

A summary of the previous work and at what conditions the equations will operate in is provided with the figure below [22]

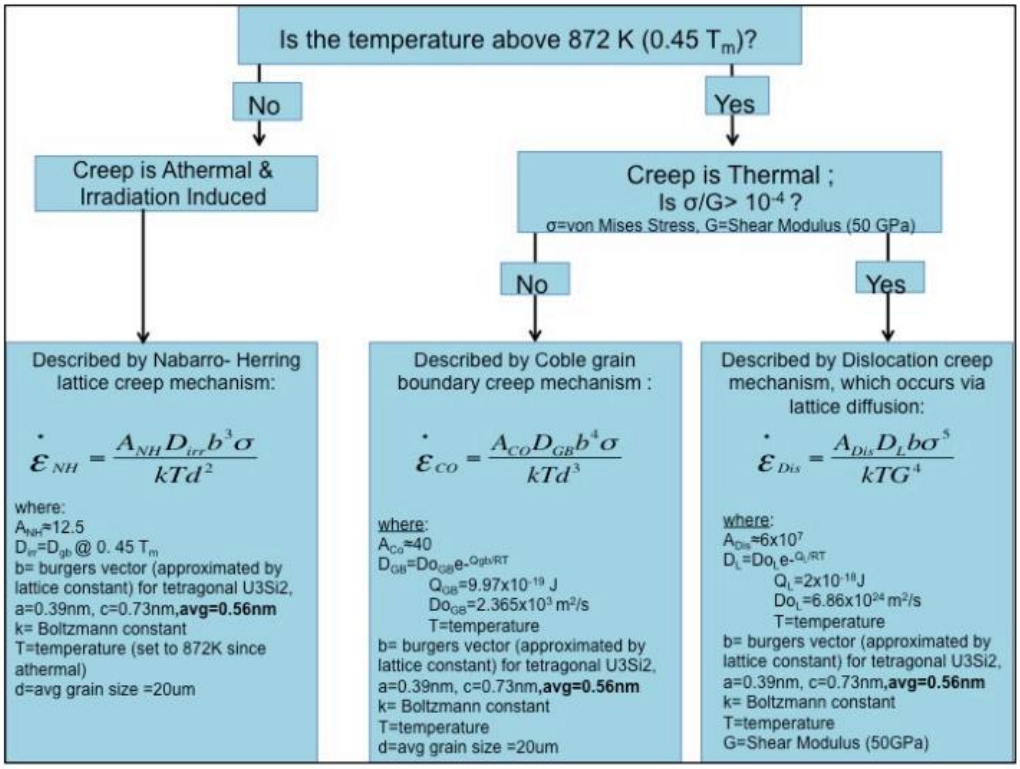

Figure 3.33: Summary of the Metzger creep model

As a comparison, stress and temperatures from Table 1.1 are used as inputs for the equations and values used in the Metzger model to predict strain rate. In addition, strain rates using the Arrhenius equation below (from values in Table 3 and Equation 1.1), are also calculated. These calculated strain rates will be compared with experimentally obtained strain rates from the same stress and temperature.

$$\frac{d\epsilon}{dt} = 8.78\text{E-}16\ \sigma^{1.94} \exp\left(-\frac{168.68}{(0.008314)T}\right) \qquad \text{Equation 3.4}$$

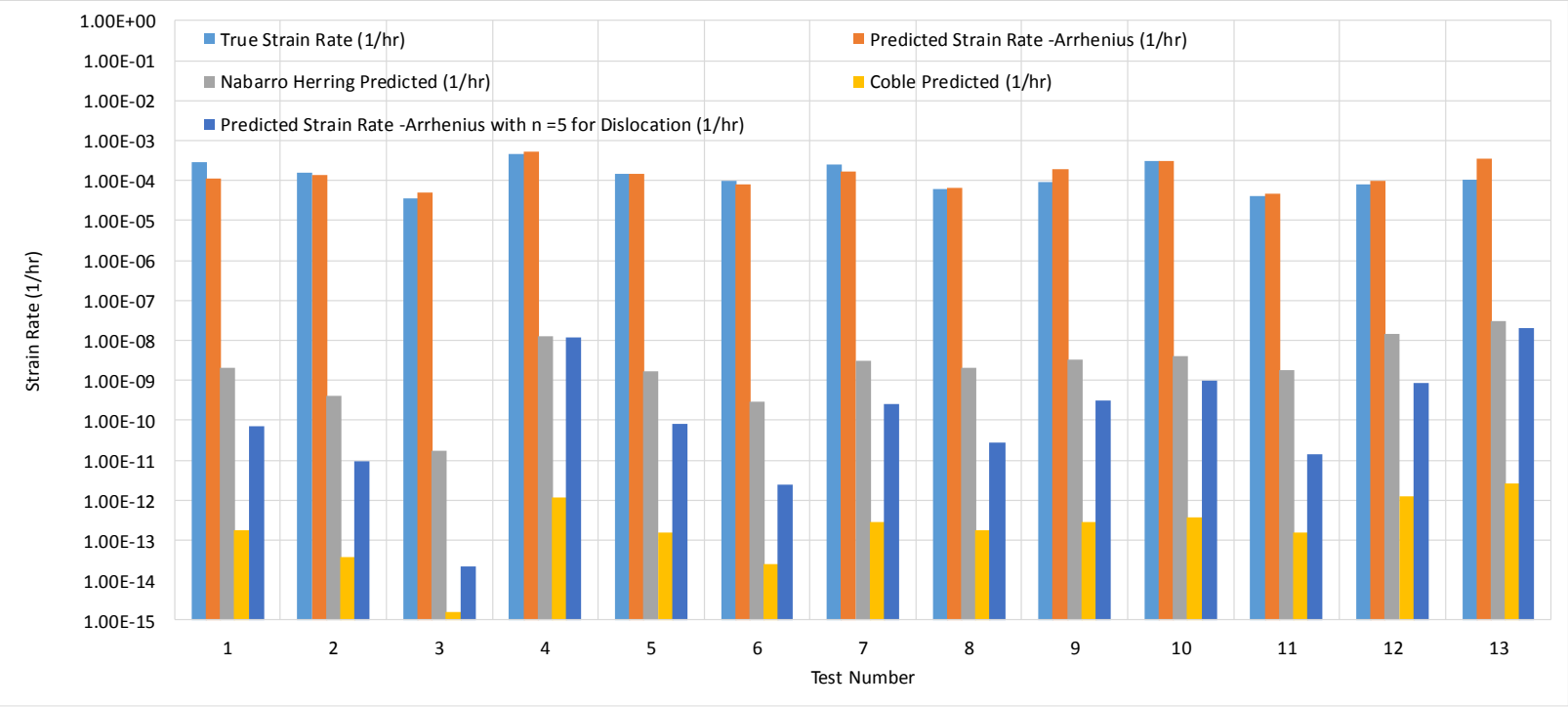

Figure 3.34: Predicted strain rates using sintering data values

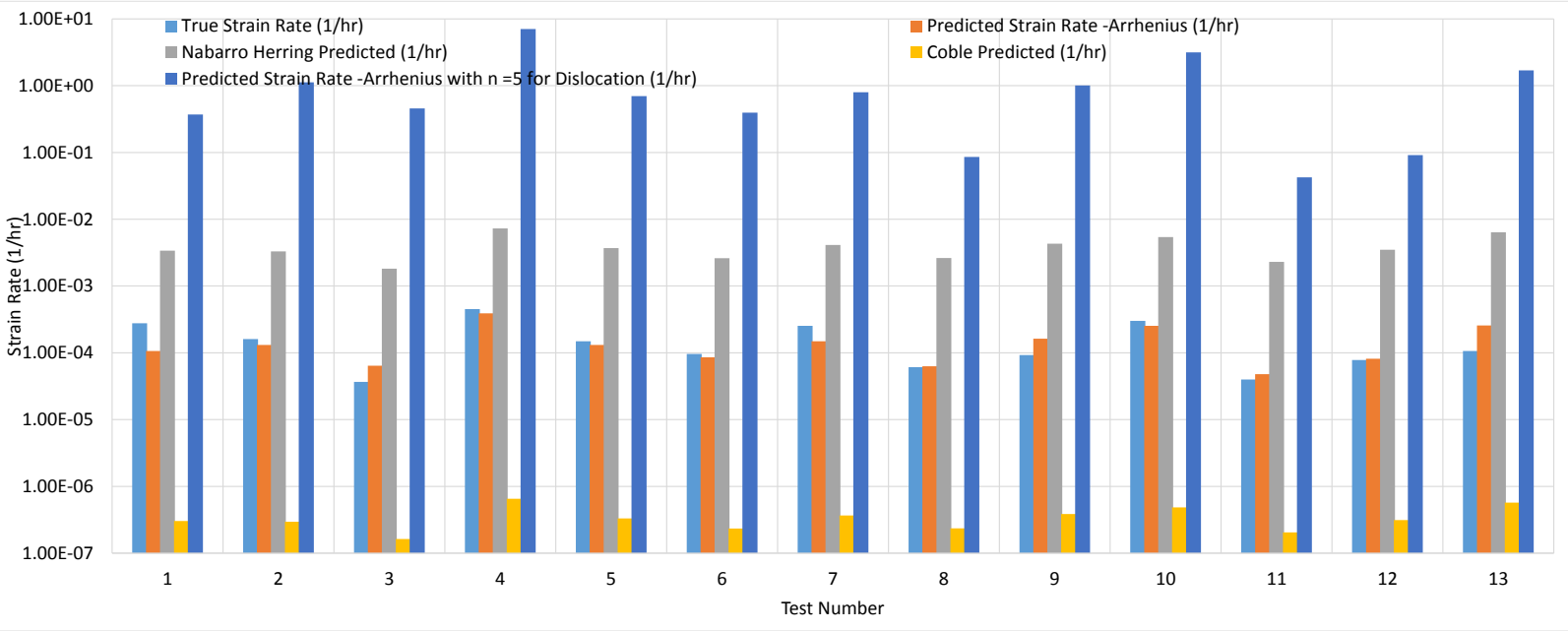

Figure 3.35: Predicted strain rates using DFT calculation values

Activation energy and diffusivities from sintering data are shown in Figure 3.34 above. They predict an extremely lower strain rates with about a four magnitude difference lower. This is identical to what Metzger reports, as there was virtually no difference between the model with creep considered vs a model with no creep considered in terms of PCMI. It was with those results that U_3Si_2 was not predicted to have a significant creep impact in reactor conditions.

However, using the activation energy from the DFT calculations lead to closer values obtained in this work as seen in Figure 3.35. The difference between the predicted Nabarro Herring creep rate are about an order of magnitude faster than the observed strain rate in this work. The values for Coble creep rate are about two orders of magnitude slower. The power law creep rate (dislocation creep) was found to be four magnitudes faster than the observed creep rate. As the predicted strain rates using the Nabarro-Herring creep rate formula are reasonably close to the experimentally obtained values, it may speak as to the dominant creep mechanism from the data in this research. Further optical and SEM imaging (currently ongoing at USC) of the post crept pellets microstructure can provide more insight into this.

As expected, the calculated creep rates found with Equation 3.4 (which uses values directly from this research) are in excellent agreement with the experimental creep rates, typically within an order of magnitude of the observed creep rates.

3.11 Modeling in BISON Using Current Data

Using the data from this research, Freeman updated the modeling case in BISON. [43] In a similar manner to the modeling work performed by Metzger, a case where creep was considered and a case where it was not considered was modeled in BISON.

A similar Arrhenius equation was developed using data from this research but a different method was used to calculate the values of A, n and Q and not all tests were used in the determination of the values. Specific details of how they were found can be seen in Chapter 3 of the report but the values used are shown in Table 3.4 below

Table 3.4: Freeman Creep Parameter Values [43]

A	Q (kJ/mol)	n
2.0386×10^{-4}	295.55	1.2063

A 10 pellet stack was modeled in BISON in reactor conditions. The specifics can be found in Chapter 4 of the report but some results of the model are highlighted in Figure 3.36 and Figure 3.37 which looks at hoop stress in the cladding.

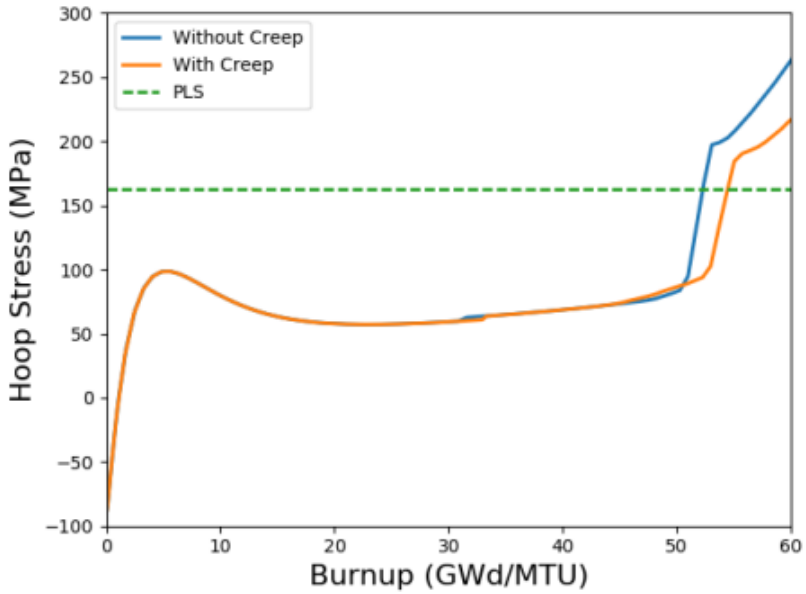

Figure 3.36: Hoop stress in composite portion of cladding – U_3Si_2 case with creep vs without creep [43]

The creep rate of U_3Si_2 has a significant impact as seen in Figure 3.36 above. Cladding contact begins at 50 GWd/MTU when the value of the hoop stress begins to

suddenly increase. In the figure, the stress in the cladding when no creep is considered (the blue line) begins to increase before the case where creep is considered (orange line) with about a 5 GWd/MTU difference. This is attributed to the gap width between the fuel and cladding remaining open longer because of the impact of the fuel creep deformation. This is in contrast to the sintering values used in the Metzger model which found little to no impact of creep.

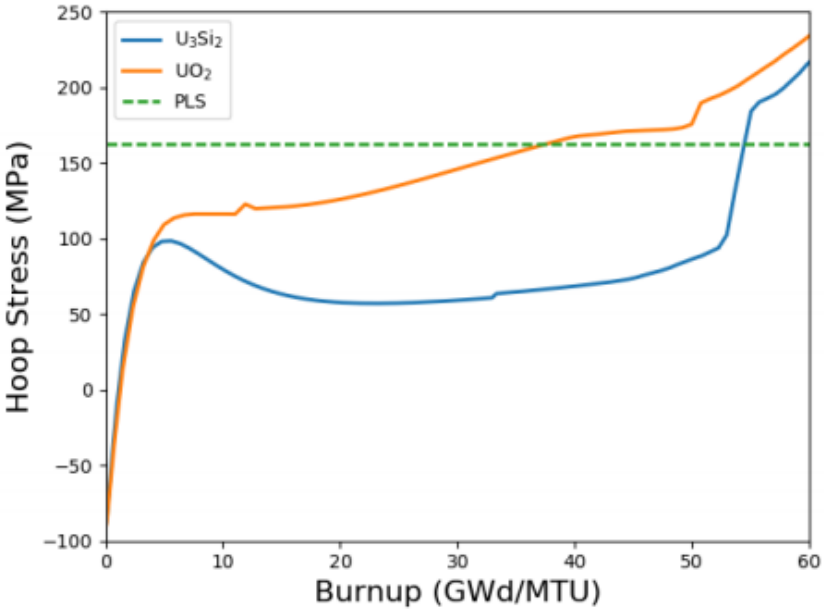

Figure 3.37: Hoop stress in cladding comparison between U_3Si_2 and UO_2 [43]

For a comparison U_3Si_2, is compared with a reference UO_2 case in reactor conditions. During the life of the fuel rod, hoop stress in the cladding is much lower in the U_3Si_2 model than in the UO_2 model with a difference of about 50 MPa. An additional burnup of approximately 18 GWd/MTU was observed before the cladding reached proportional limit stress.

3.12 Review of Activation Energy

Density functional theory calculations (DFT) of U_3Si_2 have been performed by Anderson et al [44] using the Hubbard U (PBE + U) correction method to calculate formation energies and diffusivities of point defects and atoms in the structure. The results are shown in the table below.

Table 3.5: DFT Calculations of Uranium and Silicon Self Diffusivities [44]

Diffusivity	ΔH_a (eV)	D_0 (m^2/s)
U vacancy (a-b plane)	1.48	1.86×10^{-6}
U vacancy (c-axis)	0.97	5.27×10^{-7}
U interstitial (a-b plane)	0.54	1.30×10^{-6}
U self-diffusion vacancy (a-b plane)	2.63	2.17×10^{-5}
U self-diffusion vacancy (c axis)	2.12	2.26×10^{-5}
U self-diffusion interstitial (a-b plane)	1.68	1.58×10^{-5}
Si vacancy (a-b plane)	2.24	1.19×10^{-6}
Si vacancy (c axis)	0.64	5.30×10^{-7}
Si interstitial (a-b plane)	3.05	1.86×10^{-6}
Si vacancy self-diffusion (a-b plane)	3.38	1.45×10^{-5}
Si vacancy self-diffusion (c axis)	1.78	6.46×10^{-6}
Si interstitial self-diffusion (a-b plane)	4.19	2.27×10^{-5}

The activation energy for creep obtained from the data in this research (3.5 eV) is very close to the value of Silicon vacancy self-diffusion (a-b plane) (3.38 eV). This may speak to the rate controlling process of the creep rates obtained earlier, namely being one related to diffusion. [44]

In addition, Metzger reports that for U_3Si_2, Noordhoek's DFT calculations for Silicon interstitial diffusion in U_3Si_2 is 4.56E-19J [22] which compares closely to the activation energy in this research (5.60E-19J). Again, this provides evidence for the major contribution for diffusion controlled creep.

3.13 Comparisons with Other Materials

A normalized Ashby creep map for UO_2 is provided below. [15] The position of the data obtained in this research is approximately located in the red and blue boxes in Figure 3.38 below

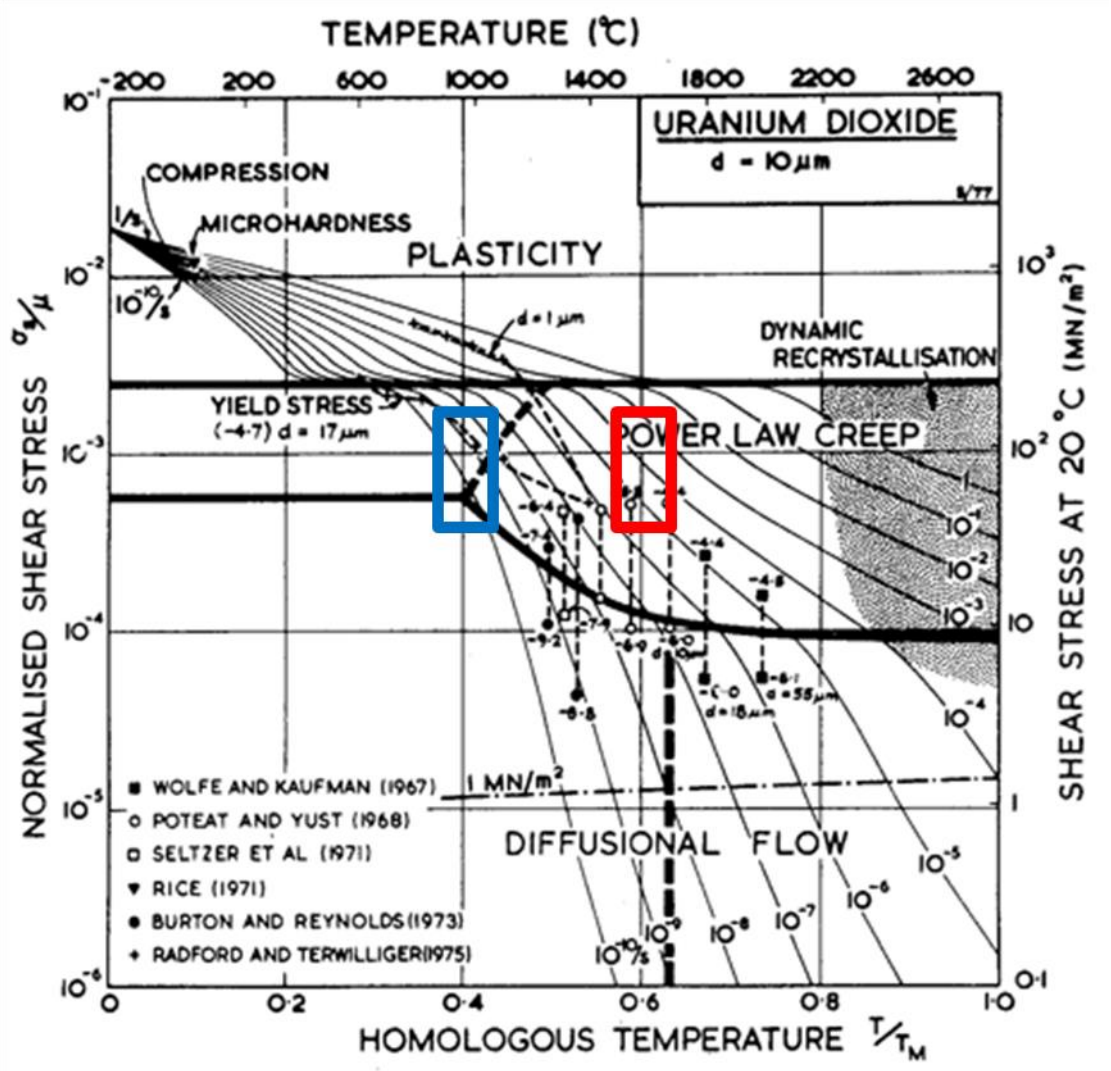

Figure 3.38: Ashby creep map with U_3Si_2 data plotted (in red) from this research.

U_3Si_2 creep values are on the order of 10^{-8} s^{-1}. When plotting the data using similar temperatures and stresses on a UO_2 Ashby Creep Map, it creeps slower than UO_2 on the order of three magnitudes. When using the actual temperature testing conditions (in the

blue box) and normalized shear stresses, U_3Si_2 readily creeps in conditions where UO_2 does not. As reported before, this speaks to the relative creep resistance of UO_2 as various dopants have been added to increase its creep rate.

Molybdenum Disilicide has a similar tetragonal crystal structure to U_3Si_2. [45]. The compressive creep response as studied by Sadananada et al over the range of 1100°C to 1300°C and from the stress ranges from 10 to 100 MPa is shown below. In addition, the data this research is plotted against their values.

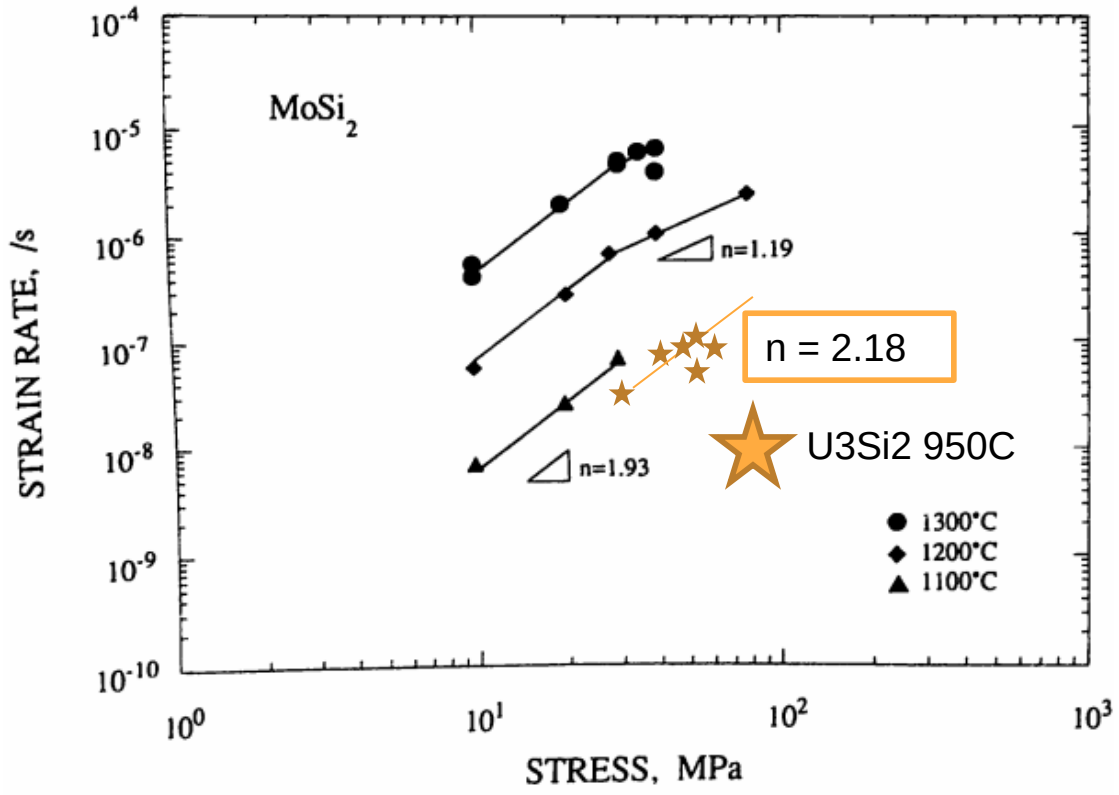

Figure 3.39: Creep response of $MoSi_2$ [45] with 950°C U_3Si_2 data

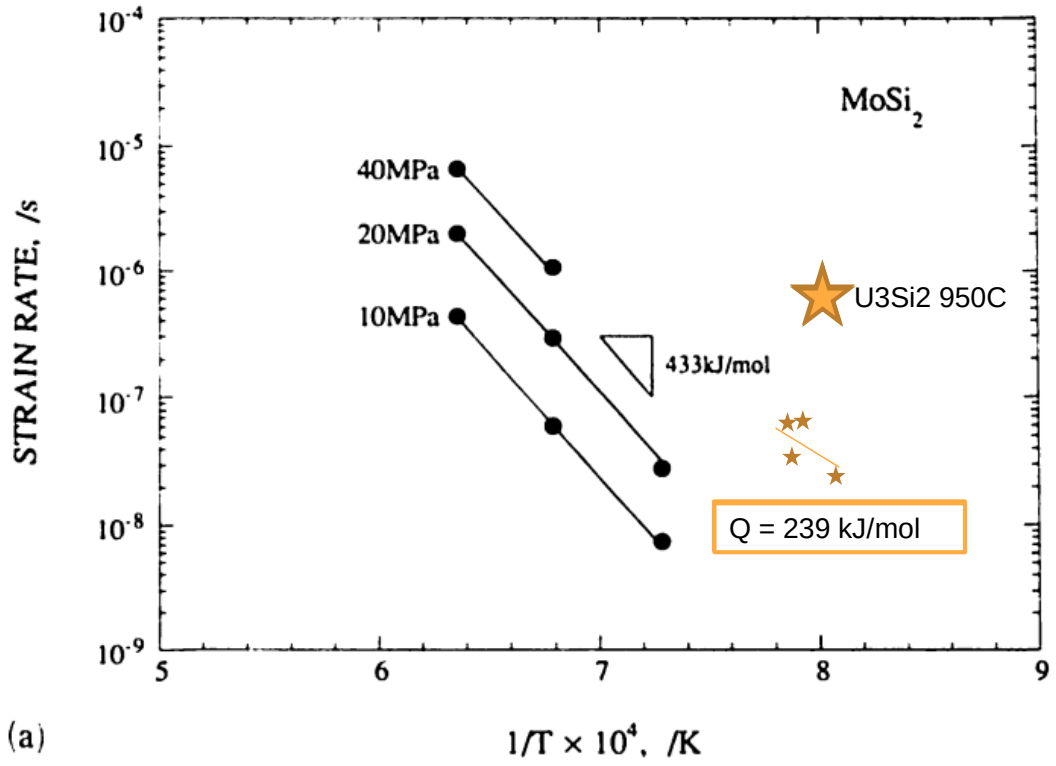

Figure 3.40: Activation energies of $MoSi_2$ [45] with 50MPa U_3Si_2 data

The activation energy is lower than the $MoSi_2$ data as seen in Figure 3.40 and has similar stress sensitivities as seen in Figure 3.39. The authors report that in the conditions tested that there is a diffusional controlled region that appears to transition to a power law area when the temperature was increased. Their estimation of the activation energy for diffusion of molybdenum in $MoSi_2$ using a semiempirical relationship (in the range of 250 to 540 kJ/mol) was in reasonable agreement with their experemintal activation energy (380 kJ/mol)[45]. Their logic is in line with the results found in this research: experimentally determined values of creep activation energy compares favorably with the DFT calculations for the activation energies of silicon and uranium in U_3Si_2 .

Chapter 4 Conclusions

4.1 Overview

A test rig has been designed and built at USC that has successfully completed a set of compression creep experiments under a controlled atmosphere. It was found that U_3Si_2 readily creeps as low as 850°C and 70 MPa.

An Arrhenius equation to predict steady state creep was made from the data gathered from this research. The activation energy for creep was found to be 168 kJ/mol or 3.5 eV. Based off of DFT calculations, it was noted that the activation energy is close to the self-diffusivities of the Silicon vacancies in the lattice, which are around 3.4 eV. In addition, the experimental stress exponent (1.94) is fairly low, as higher stress exponents can range from 3 to 5 for highly sensitive cases.

Using the Nabarro Herring creep rate equation to predict creep rates leads to values that are within an order of magnitude of the experimentally obtained creep rates. Dislocation motion equations predicted creep rates that were much higher than experimentally obtained creep rates.

From these points, it appears that the major creep mechanism in effect is diffusional controlled. It is possible that dislocation motions or grain boundary sliding can have an influence, however. Further optical analysis currently being done will lead to stronger insight into the dominant creep mechanism.

Updated modeling efforts in BISON using the data from this research indicate that creep deformation has a significant impact on time before cladding rupture in accident conditions than compared to a case where creep is not considered.

In the tested oxygen partial pressures, U_3Si_2 did not violently react but upon cooling down and unloading, a spalling effect was noted; a dull "skin" was observed on the outside of the creep pellet. It is expected that the impurities in the testing environment and extended testing times lead to this reaction.

4.2 U_3Si_2 as an ATF Candidate

The creep data in the research adds some knowledge about this fuel but there is much to be known. In an Idaho National Lab report, Gamble et al [46] report that the fuels high swelling behavior under irradiation is a subject of concern. In addition, fission gas release (tied to swelling) is an unknown factor. They note that [46]U_3Si_2 is reported to be more active than UO_2 when used in reactor conditions as, when tested with Zircaloy, interdiffusion was reported when tested at 800°C for 100 hours with Fe and Cr phases found at the interface.

Fabrication and shipping problems are present; as of now, U_3Si_2 is optimized for laboratory scale and research work. Large scale production for use in fuel rod assemblies has still not been met [46], [47] However, as an accident tolerant fuel candidate, U3Si2 still has attractive qualities. The creep performance seems promising in regards to delaying PCMI during an accident scenario. The lower operating temperatures of U3Si2 bring an additional safety factor when used in reactor. And lastly, a higher uranium density can be attractive to plant owner and operators. With more research (specifically into the area of fission gas release and swelling), it is possible that U3Si2 can find its place as an ATF in the future.

References

[1] M. McClure, “Stanford researchers calculate global health impacts of the Fukushima nuclear disaster.” [Online]. Available: https://engineering.stanford.edu/magazine/article/stanford-researchers-calculate-global-health-impacts-fukushima-nuclear-disaster.

[2] “Development of Light Water Reactor Fuels with Enhanced Accident Tolerance Report to Congress April 2015.”

[3] “FUKUSHIMA DAIICHI : ANS Committee Report,” LaGrange Park, 2012.

[4] J. A. V. and K. J. M. A.T. Nelson, J.T. White, D.D. Byler, J.T. Dunwoody, “Overview of Properties and Performance of Uranium-Silicide Compounds for Light Water Reactor Applications,” *Trans. Am. Nucl. Soc.*, vol. 110, pp. 987–989, 2014.

[5] L. H. Ortega, B. J. Blamer, J. A. Evans, and S. M. McDeavitt, “Development of an accident-tolerant fuel composite from uranium mononitride (UN) and uranium sesquisilicide (U3Si2) with increased uranium loading,” *J. Nucl. Mater.*, vol. 471, pp. 116–121, 2016.

[6] H. Shimizu, “The properties and irradiation behavior of U3Si2,” *At. Int.*, no. NAA-SR-10621, pp. 1–44, 1965.

[7] K. M. Taylor and C. H. McMurtry, “SYNTHESIS AND FABRICATION OF REFRACTORY URANIUM COMPOUNDS. Summary Report for May 1959 through December 1960,” 1961.

[8] J. Secker, F. Franceschini, S. Ray, W. E. Company, C. Township, and F. Efficiency, “Accident Tolerant Fuel and Resulting Fuel Efficiency Improvements,” *Adv. Nucl. Fuel Manag. V (ANFM 2015)*, no. Anfm, pp. 1–10, 2015.

[9] C. Industries, “creep in plastic materials.” [Online]. Available: http://www.craftechind.com/creep-plastic-materials/.

[10] J. S. Perrin, “Irradiation-induced creep of uranium dioxide,” *J. Nucl. Mater.*, vol. 39, no. 2, pp. 175–182, 1971.

[11] “ZwickUSA. Kappa DS.” [Online]. Available: http://www.zwickusa.com/en/products/static-materials-testing-machines/testing-machines-from-5-kn-to-250-kn/creep-testing-machines/electro-mechanical-creep-testing-machines/kappa-ds.html.

[12] J. Pelleg, “Creep in ceramics,” *Solid Mech. its Appl.*, vol. 241, pp. 41–61, 2017.

[13] S. Sharma, “LECTURE 12.” [Online]. Available: http://www.nptel.ac.in/courses/112107146/lects & picts/image/lect12/lecture12.htm.

[14] N. R. Center, “Linear Defects - Dislocations.” [Online]. Available: https://www.nde-ed.org/EducationResources/CommunityCollege/Materials/Structure/linear_defects.htm.

[15] H. J. Frost, “Deformation-Mechanism Maps, The Plasticity and Creep of Metals and Ceramics.” [Online]. Available: http://engineering.dartmouth.edu/defmech/chapter_2.htm.

[16] T. G. Langdon, “Identifiying creep mechanisms at low stresses,” *Mater. Sci. Eng. A*, vol. 283, no. 1–2, pp. 266–273, 2000.

[17] W. M. Armstrong, W. R. Irvine, and R. H. Martinson, “Creep deformation of stoichiometric uranium dioxide,” *J. Nucl. Mater.*, vol. 7, no. 2, pp. 133–141, 1962.

[18] P. E. Bohaboy, R. R. Asamoto, and A. E. Conti, “COMPRESSIVE CREEP CHARACTERISTICS OF STOICHIOMETRIC URANIUM DIOXIDE.”

[19] R. A. Wolfe and S. F. Kaufman, “Mechanical Properties of Oxide Fuels (Lsbr/Lwb Development Program).,” Pittsburgh, 1967.

[20] A. R. Massih and L. O. Jernkvist, “Effect of additives on self-diffusion and creep of UO<inf>2</inf>,” *Comput. Mater. Sci.*, vol. 110, pp. 152–162, 2015.

[21] C. Duguay, A. Mocellin, P. Dehaudt, and G. Fantozzi, “High temperature compression tests performed on doped fuels,” *Key Eng. Mater.*, vol. 132–136, 1997.

[22] K. Metzger, “Analysis Of Pellet Cladding Interaction And Creep Of U3Si2 Fuel For Use In Light Water Reactors,” Dissertation. University of South Carolina, 2016.

[23] “Edmund Optics. Telecentric Illumination: Why You need it in machine vision applications.” [Online]. Available: https://www.edmundoptics.com/resources/application-notes/imaging/telecentric-illumination-why-you-need-it-in-machine-vision-applications/.

[24] “cvmatch template plugin.” [Online]. Available: https://sites.google.com/site/qingzongtseng/template-matching-ij-plugin.

[25] “McMaster-Carr - Tooling Ball.” [Online]. Available: https://www.mcmaster.com/#8484a19/=1cfswyo.

[26] “True Stress/Strain.” [Online]. Available: http://web.adanabtu.edu.tr/Files/iyilmaz/Duyuru/dosya/ME 207 – Chapter 3_P3.pdf.

[27] T. Montaruli, “Electric Power and Joule Heating.” [Online]. Available: http://icecube.wisc.edu/~tmontaruli/Phys248/lectures/lecture29.pdf.

[28] “ISO Vacuum and High Vacuum Components.” [Online]. Available: http://schoonoverinc.com/iso-flanges-fittings/.

[29] “Inconel Rods on Mcmaster.” [Online]. Available: https://www.mcmaster.com/#=1c2yck7.

[30] “Thermal - Thermal Conductivity.” [Online]. Available: https://global.kyocera.com/fcworld/charact/heat/thermalcond.html.

[31] “ZIROX Vacuum Probe.” [Online]. Available: http://www.zirox.de/fileadmin/user_upload/datasheets/probes/PI_Vak_eng.pdf.

[32] “Oerlikon Total Vacuum Probe.” [Online]. Available: http://www.idealvac.com/files/manuals/Leybold-PTR90-Gauge-Specs-Data-Manual.pdf.

[33] “MODEL LCB200 In Line Rod End Load Cell Tension and Compression.” [Online]. Available: http://www.futek.com/files/pdf/Product Drawings/lcb200.pdf.

[34] “Lumasense pyrometer.” [Online]. Available: https://www.lumasenseinc.com/uploads/Products/Temperature_Measurement/Infrared_Thermometers/IMPAC_Pyrometers/Series_6/pdf/EN-ISR6-Advanced_Datasheet.pdf.

[35] “Grasshopper 5.0 MP Mono FireWire 1394b (Sony ICX625).” [Online]. Available: https://www.ptgrey.com/grasshopper-5-0-mp-mono-firewire-1394b-sony-icx625-camera.

[36] “TCLWD050 Long working distance telecentric lens.,” *Datasheet*. [Online]. Available: http://www.opto-engineering.com/products/TCLWD050.

[37] “Acme FS11000 Transformer.” [Online]. Available: http://www.temcoindustrialpower.com/products/Transformers_-_General/AT1370.html.

[38] “Hammond Collodial 1182v24 transformer.” [Online]. Available: http://www.newark.com/hammond/1182v24/transformer-toroid-48v-1kva/dp/54X7561.

[39] “Watlow EZ-ZONE PM EXPRESS.” [Online]. Available: http://www.watlow.com/products/controllers/integrated-multi-function-controllers/ez-zone-pm-express.

[40] T. Montaruli, “TestWorld.com. Agilent 34970A/34972A Data Acquisition/Switch Unit Users Guide.” [Online]. Available: https://testworld.com/wp-content/uploads/user-guide-keysight-agilent-34970a-34972a-daq.pdf.

[41] “Prescale pressure film.” [Online]. Available: http://www.fujifilm.com/products/prescale/prescalefilm/%5C.

[42] “Creep Deformation of Metals.” [Online]. Available: https://www.saylor.org/site/wp-content/uploads/2011/07/ME102-3.3.5.pdf%0A.

[43] R. Freeman, “ANALYSIS OF PELLET-CLADDING MECHANICAL INTERACTION ON U3Si2 FUEL WITH A MULTI-LAYER SiC CLADDING USING BISON,” Masters Thesis. University of South Carolina.

[44] A. D. Andersson, “Density functional theory calculations of defect and fission gas properties in U-Si fuels,” Los Alamos, 2016.

[45] K. Sadananda, C. R. Feng, H. Jones, and J. Petrovic, “Creep of molybdenum disilicide composites,” *Mater. Sci. Eng. A*, vol. 155, no. 1–2, pp. 227–239, 1992.

[46] K. A. L. Gamble, J. D. Hales, T. Barani, D. Pizzocri, and G. Pastore, “Behavior of U3Si2 Fuel and FeCrAl Cladding under Normal Operating and Accident Reactor Conditions,” Idaho Falls, 2016.

[47] J. M. Harp, P. A. Lessing, and R. E. Hoggan, “Uranium silicide pellet fabrication by powder metallurgy for accident tolerant fuel evaluation and irradiation,” *J. Nucl. Mater.*, vol. 466, pp. 1–11, 2015.